Preparation and characterisation of thio-kaolinite nanohybrid materials for heavy metal sorption from wastewater

Marijke Struijk

Thesis submitted to the Faculty of Graduate and Postdoctoral
Studies in partial fulfilment of the requirements for the
MSc degree in Chemistry

Department of Chemistry
Faculty of Science
University of Ottawa

Acknowledgements

I would like to express my gratitude to the following people who have made this research project and writing up of the thesis possible:

- Christian Detellier for giving me the opportunity to perform this research project, for his support and feedback throughout, and his flexibility with the direction of the project.
- Rola Mansa for her helpfulness and patience with many questions, her general support, as well as for training on TGA, XRD, and FT-IR.
- Nimal De Silva for performing and explaining ICP-MS analyses and his kind help, enjoyable talks and warm welcome in his lab and office.
- Fernando Rocha from the University of Aveiro, Portugal for teaching me about mineralogical interpretation of XRD patterns and supporting the preliminary stages of this project.
- Tim Lewis, Gary Roubidoux, and Michel Chevalier at the Robert O. Pickard Environmental Centre for large amounts of sample of Ottawa's raw sewage and effluent, as well as providing several monitoring data sheets.
- Christian Detellier's research group, in particular Gustave Kenne for his preliminary grafting assays and helping me get started with the laboratory procedures, and Jonathan Fafard for exchanging ideas to help me overcome some challenges.
- Glenn Facey and Eric Ye for help running NMR experiments and special credits to Glenn for figuring out a way to obtain a ^{13}C NMR spectrum of solid urea.
- David Schneider from the Earth and Environmental Sciences department for granting me access to the mechanical grinder.
- Last but certainly not least, my parents for supporting me throughout my studies, which has been particularly valuable these past two years.

Abstract

Heavy metals are non-degradable and their persistence constitutes ecotoxicological ramifications. Their presence in wastewater is inhibitory to microbial digestion processes and can lead to biomagnification in the environment. Clay minerals have been widely studied as inexpensive sorbent materials of aqueous-phase contaminants. Particularly in the case of kaolinite, a non-swelling clay with a low cation-exchange capacity, chemically enhanced derivatives exposing its OH-rich interlayer space to interactions with its external environment are of exceptional interest. The objective of this study was to prepare a novel functionalised kaolinite with the aim of significantly improving its heavy-metal sorption capacity.

Due to the robustness of sulfur-metal linkages, the compound 3,6-dithia-1,8-octanediol ($HO(CH_2)_2S(CH_2)_2S(CH_2)_2OH$) was grafted onto both urea- and DMSO precursors of two kaolinitic clays: the Source clay KGa-1b and a Portuguese clay sample collected from the Clays of Taveiro formation. All samples were characterised by X-ray diffraction and ^{13}C nuclear magnetic resonance spectroscopy (NMR). Initial materials and final samples were also characterised by thermal gravimetric analysis and infrared spectroscopy. The results describe nanohybrid materials that are resistant to hydrolysis and exhibit different grafting fashions.

Application as a heavy metal sorbent was tested in $ZnCl_2$ solutions as well as in zinc-spiked raw wastewater. Zinc concentrations were analysed concomitant with other metal species by inductively coupled plasma – mass spectrometry, demonstrating variable sorption capacities of the different clay samples tested and a consistently greater zinc removal in the wastewater system compared to simple zinc solutions. Measured concentrations of concomitantly analysed metals reveals a potentially alarming release of certain heavy metal species from some clay samples as a result of zinc sorption.

Résumé

Les métaux lourds ne sont pas dégradables et leur persistance peut avoir des répercussions écotoxicologiques. De plus, leur présence dans les eaux usées nuit aux processus de digestion microbienne et peut entraîner une bioamplification dans l'environnement. Les minéraux argileux ont fait l'objet de nombreuses études en tant que matériaux utiles pour la sorption des contaminants en phase aqueuse. La kaolinite est une argile non-gonflante ayant une faible capacité d'échange cationique. Ses dérivés chimiquement modifiés sont particulièrement intéressants, parce que leur espace interfoliaire, riche en groupements -OH, est prédisposé aux interactions avec l'environnement extérieur. L'objectif de l'étude était de préparer une kaolinite fonctionnalisée dont la capacité de sorption des métaux lourds serait considérablement améliorée.

Grâce à la forte liaison soufre-métal, le composé 3,6-dithia-1,8-octanediol ($HO(CH_2)_2S(CH_2)_2S(CH_2)_2OH$) a été greffé sur des précurseurs DMSO et urée de deux argiles kaolinitique: L'argile « source » KGa-1b et un échantillon d'argile provenant d'une formation argileuse de Taveiro au Portugal. Tous les échantillons ont été caractérisés par l'analyse par diffractions des rayons-X et par la spectroscopie de résonance magnétique nucléaire (RMN) du ^{13}C. Les matériaux initiaux et les échantillons finaux ont aussi été caractérisés par l'analyse thermogravimétrique et la spectroscopie infrarouge. Les résultats révèlent l'existence de matériaux nanohybrides résistants à l'hydrolyse et celle de différents modes de greffage.

L'utilisation d'argile en tant que sorbant de métaux lourds a été testée avec des solutions de $ZnCl_2$ et d'eaux usées ayant de fortes concentrations en zinc. Les concentrations en zinc ainsi que celles d'autres métaux ont été mesurées avec un spectromètre de masse par torche à plasma. Les résultats ont montré que la capacité de sorption variait suivant les différents échantillons d'argiles testés et que le taux de sorption du zinc était constamment plus grand dans les eaux usées en comparaison des simples solutions de zinc. Les concentrations de métaux mesurées révèlent le relargage potentiellement alarmant de certains métaux lourds de quelques échantillons d'argiles en raison de la sorption du zinc.

Table of Contents

List of Abbreviations

AIPEA	Association Internationale pour l'Étude des Argiles
ATR	Attenuated Total Reflection
B_0	Stationary magnetic field in NMR
BOD	Biological oxygen demand
cBOD	carbonaceous biological oxygen demand
CEC	Cation-exchange capacity
CMS	Clay Minerals Society
COD	chemical oxygen demand
CP	Cross polarization
CRC	Collision/reaction cell
d_{001}	Basal spacing
DDEM	Discrete dynode electron multiplier
DI	Deionised water
DMSO	Dimethyl sulfoxide
DTA	Differential thermal analysis
DTG	Derivative Thermogravimetric Analysis
DTOD	3,6-dithia-1,8-octanediol
EPA	Environmental Protection Agency
FT-IR	Fourier Transform Infrared
ICP-MS	Inductively coupled plasma – mass spectrometry
IR	infrared
K-bulk	<63-fraction of KGa-1b, as delivered by CMS
K-DMSO	DMSO-intercalated precursor sample with parent material Kga-1b
K-DMSO-DTOD	DTOD-grafted K-DMSO, where DMSO has been replaced by DTOD
KED	Kinetic energy discrimination
K-fine	Clay fraction (<2 µm) of Kga-1b, purified by sedimentation
KGa-1b	CMS-source-clay kaolinite from Georgia, United States
K-urea	Urea-intercalated precursor sample with parent material KGa-1b
K-urea-DTOD	DTOD-grafted K-urea, where urea has been replaced by DTOD
lb	Line broadening
MAS	Magic angle spinning
MS	Mass spectrometer
MW	Molecular weight
n.d.	"no date" or "not detected", depending on the

NMR	Nuclear magnetic resonance
ORS	Octopole Reaction System
QQQ	Triple Quad, system in MS
r.f.	Radiofrequency
SD	Standard deviation
SE	Standard error of the mean
SEM	Scanning electron microscopy
SP	São Pedro, kaolinitic sample from Taveiro, Portugal
SP-bulk	<63-µm fraction of SP, by sieving
SP-DMSO	DMSO-intercalated precursor sample with parent material SP
SP-DMSO-DTOD	DTOD-exchanged SP-DMSO, where DMSO was not successfully replaced by DTOD
SP-fine	clay fraction (<2 µm) of SP, purified by sedimentation
SP-urea	Urea-intercalated precursor sample with parent material SP
SP-urea-DTOD	DTOD-grafter SP-urea, where urea has been replaced by DTOD
TGA	Thermogravimetric analysis
TMS	Tetramethylsilane, internal standard in NMR spectroscopy
TOC	Total organic carbon
TSS	Total suspended solids
UV	ultraviolet
WW	Wastewater
WWTP	Wastewater treatment plant
XRD	X-ray diffraction
XRF	X-ray fluorescence

List of Figures, Tables and Appendices

Figures

Tables

Appendices

Introduction

Clay minerals have played important roles in human civilization. Since ancient times clay has been used for ceramics, adobe houses, body cleansers (both internal and external), tablets, statues, and bricks (Levey, 1959). Nowadays, clay is still used as such, and is also the topic of many interdisciplinary academic studies that range from geologic, chemical and environmental interests, to applications in the fields of pharmacology, pollutant remediation, soil carbon cycling, and industrial filler materials.

The understanding of what clay is and what constitutes a clay mineral has evolved over time and may differ per discipline. For instance, in geology and soil science particles <2 μm are considered as clays, and in colloid chemistry a particle size of <1 μm is used (Guggenheim and Martin, 1995). Clays often involve hydrated aluminium silicates, though this is not a fixed property. In the nineties two committees, the "Association Internationale pour l'Étude des Argiles" (AIPEA) and the Clay Minerals Society (CMS), joined forces to attempt to synthesize good definitions for the terms *clay* and *clay mineral* (Guggenheim and Martin, 1995). They decided that the term *clay* refers to: "a naturally occurring material composed primarily of fine-grained minerals, which is generally plastic at appropriate water contents and will harden [when] dried or fired. Although clay usually contains phyllosilicates, it may contain other materials that impart plasticity and harden when dried or fired. Associated phases in clay may include materials that do not impart plasticity and organic matter" (Guggenheim and Martin, 1995). Examples of associated phases include quartz, dolomite, and feldspars, and "other materials that impart plasticity" could be some oxy-hydroxide minerals (Guggenheim and Martin, 1995). *Clay minerals,* then, are "phyllosilicate minerals and … minerals which impart plasticity to clay and which harden upon drying or firing" (Guggenheim and Martin, 1995).

The building blocks of clay minerals are octahedral and tetrahedral sheets (with the model unit $[SiO_4]^{4-}$) that together form layers. The former can be dioctahedral, with a vacant site in the octahedral lattice structure – based on the composition of a gibbsite sheet ($Al(OH)_3$ units), or trioctahedral, based on the composition of a brucite sheet ($Mg(OH)_2$ units). A reason for the immense multitude of clay species is the large range of possible constituent elements within the geometric oxide- and hydroxide configurational layers. The chemical and structural composition of clay minerals varies widely, involving various combinations of sheets and different possibilities of constituent elements diverging from the aforementioned model compositions, so-called isomorphous substitutions. This can bring about small layer defects and/or layer charges that are compensated by electrostatically bonded cations that give rise to a property known as the cation-exchange capacity (CEC). Common isomorphous substitutions include the replacement of Si^{4+} by Al^{3+} in part of the tetrahedral sites, or Mg^{2+} replacing Al^{3+} in the octahedral layer. This enables reversible adsorption of cations (H^+, Na^+, K^+, Ca^{2+}, etc. and water molecules) on clay surfaces – in the case of non-swelling clay minerals including kaolinite and illite – and between layers – in the case of swelling clay minerals such as smectites and vermiculite. The CEC is a property to which most of a clay mineral's chemical activity in the environment can be attributed.

There is a vast array of possible clay mineral configurations that can evolve on *earth.* If no clear framework is set up from the start, this can become very complex, so a group of scientists at the International Soil Congress in Amsterdam in 1950 (Guggenheim *et al*., 2006) introduced order to the many classifications and nomenclatures that had been made over the previous years. The AIPEA established a nomenclature committee in 1966, and one of their more recent classifications has been included here (Table 0.1).

Table 0.1. Classification scheme for planar hydrous phyllosilicates related to clay minerals (adapted from Guggenheim *et al*., 2006; Bailey *et al*., 1980). Trioctahedral and dioctahedral minerals are indicated as T and D respectively. Some of the frequently encountered minerals have been underlined.

Layer type	Interlayer material (charge per unit formula)	Group	Sub-group	Species (non-exhaustive)
1:1	None or H_2O only (~0)	Serpentine-kaolin	T	Lizardite, berthierine, amesite, cronstedtite, nepouite, kellyite, fraipontite, brindleyite
			D	Kaolinite, dickite, nacrite, halloysite (planar)
			D,t	Odinite
2:1	None (~0)	Pyrophyllite-talc	T	Talc, willemseite, kerolite, pimelite
			D	Pyrophyllite, ferripyrophyllite
	Hydrated exchangeable cations (~0.2-0.6)	Smectite	T	Saponite, hectorite, sauconite, stevensite, swinefordite
			D	Montmorillonite, beidellite, nontronite, volkonskoite
	Hydrated exchangeable cations (~0.6-0.9)	Vermiculite	T	Trioctahedral vermiculite
			D	Dioctahedral vermiculite
	Non-hydrated monovalent cations (>50% monovalent, ~0.85-1)	True (flexible) mica	T	Annite, phlogopite, lepidolite, aspidolite
			D	Muscovite, paragonite, celadonite
	Non-hydrated mono- or divalent cations (`0.6-0.85)	Interlayer-deficient mica	T	Illite, glauconite, brammallite
			D	Wonesite
	Non-hydrated divalent cations (>50% divalent, ~1,8-2)	Brittle mica	T	Clintonite, kinoshitalite, bityite, anandite
			D	Margarite, chernyknite
	Hydroxide sheet (variable)	Chlorite	T	Clinochlore, chamosite, pennantite, nimite, baileychlore
			D	Donbassite
			D,t	Cookeite, sudoite
2:1	Regularly interstratified (variable)	Variable	T	Corrensite, aliettite, hydrobiotite, kulkeite
			D	Rectorite, tosudite, brinrobertsite
1:1, 2:1			T	Dozyite

With this brief introduction to clay minerals and an appreciation of some recent historical efforts in the relatively new field of clay science, the key mineral of this study can now be introduced: kaolinite. The word “kaolin” stems from the word Kauling, which is Chinese for “high ridge” (Murray, 1988). The mine Kauling was located on a high ridge in the Kiangsi Province in China and has long been a major mine of kaolinite, which has been used throughout the ages for the production of ceramics and is now widely used in the paper industry (Giese, 1988; Murray, 1988). Kaolinite is thought to have originated from China while the name Chinaware was adopted when kaolinite was discovered in Cornwall, England, where it was described as a similar material to the ceramic urns brought over by Marco Polo from China (Murray, 1988).

The more traditional uses of kaolinite have long benefitted from its rigid structure (e.g. bricks, pottery), while more recent uses in the synthesis of nanocomposites have been more focused on smectites and other high charge-per-formula-unit clay minerals that are relatively easier to delaminate and chemically modify. Nonetheless, its abundance and high relative hydroxyl content makes kaolinite a promising clay mineral that deserves further research. Some of its important properties are summarized in Table 0.2.

Table 0.2. Important properties of kaolin (mainly composed of kaolinite; adapted from Murray, 2007).

(Near-)white in colour
Chemically inert over a wide pH range (4-9)
Fine particle size
Soft and non-abrasive (Hardness of 1.5-2.0 on the Mohs' scale)
Platy with the plate surface dimensions relatively large compared to the thickness
Hydrophillic and disperses readily in water-wash
Plastic, refractory and dries to a white or near-white colour
Low conductivity of both heat and electricity
A very low layer charge
A low surface area compared with other clay minerals
Some kaolins have a low viscosity and flow readily at 70% solids
Relatively low in cost

The clay science community is well aware of the interesting physicochemical properties of clay minerals. Their versatility and relative low cost make them apt candidates for an large range of material and processing niches, with recent expansions in the domains of nanocomposites and other modified clay varieties – some studies of which have also involved applications as heavy metal sorbents in aqueous-phase systems.

The laboratory work that forms the foundation of this thesis has been performed in two stages. First, a recent and an age-old method were used to access the interlayer space within the kaolinite mineral to subsequently graft a sulfur-containing compound, creating a thio-kaolinite of which the characterisation results following the different stages of the clay modifications are presented in chapter 3. A study of their application as heavy metal sorbents for the purpose of wastewater remediation is reported in chapter 4. First, however, the relevant background information will be given to put this work into context in chapter 1, and the theory and instrumentation of the analytical techniques used are described in chapter 2.

CHAPTER 1
Context of the work

1.1. The composition and chemistry of kaolinite

A product of progressive weathering, kaolinite is one of the most abundant clay minerals (Müller, 1967; Miranda-Trevino and Coles, 2003). Belonging to the 1:1 type minerals, its structural layer is composed of one tetrahedral sheet ($[SiO_4]^{4-}$ units) that is connected by apical oxygens to one octahedral sheet (dioctahedral gibbsite $[Al(OH)_3]$) by hydrogen bonding (Fig. 1.1.1). By convention, this structure is considered to have its sheets lying parallel to the a- and b-axes, and its layers stacking on top of each other in the c-direction. In theory this structural layer is continuous along a and b, but in reality there are faults that usually occur such that hexagonal platelets are formed (Fig. 1.1.2).

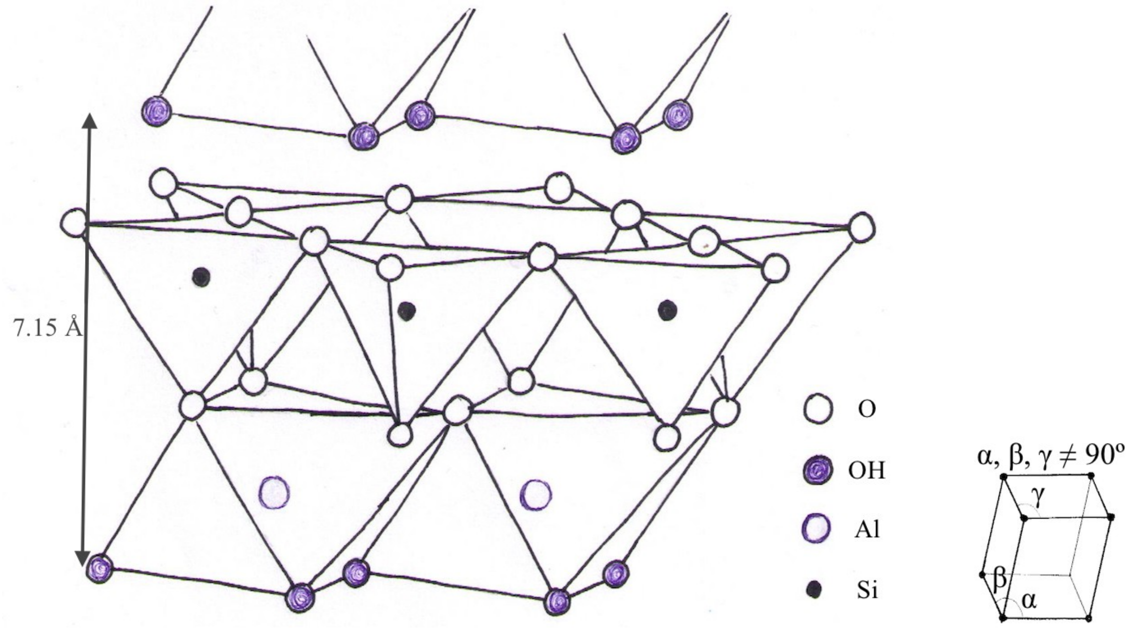

Figure 1.1.1. Diagram of the idealized mineral structure of kaolinite (adapted and redrawn from USGS, n.d.) with a d-spacing of 7.15 Å, and its triclinic lattice system.

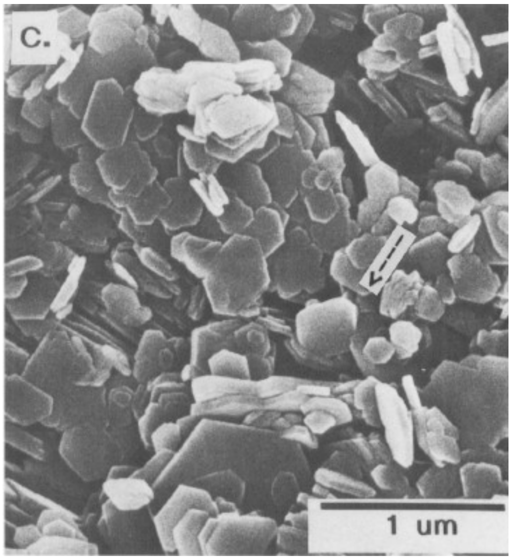

Figure 1.1.2. SEM image of KGa-1b kaolinite sample, illustrating its hexagonal shape and typical edge-to-face orientation (From Pruett and Webb, 1993, figure 6c. Reproduced with kind permission of The Clay Minerals Society, publisher of *Clays and Clay Minerals.*)

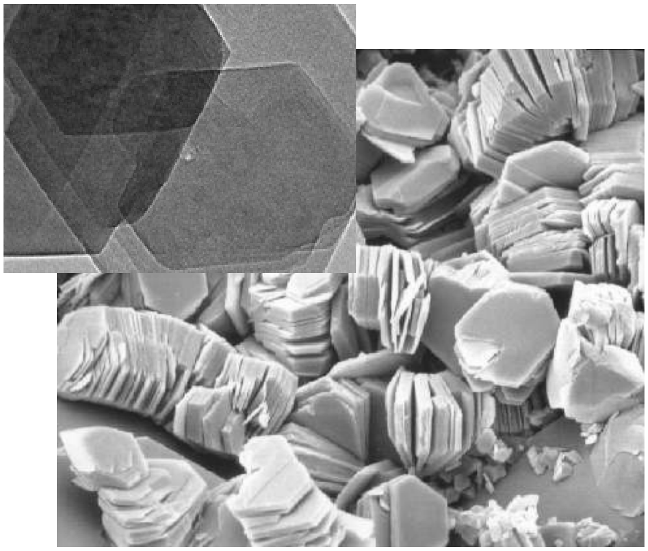

Figure 1.1.3. TEM image of kaolinite, illustrating its hexagonal shape (top; from the Detellier research group), and SEM image of kaolinite illustrating its stacking order (image frequently portrayed on the web).

The axes do not run along orthogonal lines, but rather along the axes defined by the relevant crystal lattice system. Although early X-ray diffraction studies on the structure of kaolinite were initially interpreted as part of the monoclinic crystal system (Ross and Kerr, 1930), a triclinic unit cell was later determined for kaolinite (Brindley and Robinson, 1946; Young and Hewat, 1988; see Fig. 1.1.1), because of slightly different orientations of inner-surface and inner hydroxyl groups (Ruiz Cruz, 2007). The distance between lattice planes – identified by Miller indices (*hkl*) – are called d-spacing, and when referring to the layer thickness in the c-direction it is called the basal spacing (see Fig. 1.1.1).

Kaolinite is unique among other clay minerals for its relatively uniform chemical composition that is typically (by weight) 46.54% SiO_2, 39.5% Al_2O_3, and 13.96% H_2O, corresponding to the ideal unit formula $Al_2Si_2O_5(OH)_4$ (Giese, 1988). Other elements that are frequently found with kaolinite include iron, titanium, potassium and magnesium (Ruiz Cruz, 2007).

The cation-exchange capacity (CEC) consists primarily of the charges caused by isomorphous substitutions provided that the charge-compensating cations are exchangeable, and on the pH-dependent edge-site cation coordination (Bolland *et al*., 1980; Bergaya *et al*., 2006). Isomorphous substitutions in kaolinite are limited, though Fe and Ti have been observed as part of the kaolinite mineral structure rather than in the form of an accessory mineral like anatase (Newman and Brown, 1987). As a result, kaolinite exhibits a low layer charge and small CEC, which is correlated to its relatively low chemical reactivity compared to swelling minerals like smectites. This, combined with the relative difficulty of accessing the interlayer space compared to expandable clay, may explain why modification of the interlayer space of kaolinite has received considerably less attention in the literature compared to montmorillonite, as has been noted by numerous authors (e.g. Tunney and Detellier, 1996; Yang *et al*., 2012).

Kaolinite is a non-swelling mineral whose layers are held together by hydrogen bonds between asymmetric interlayer surfaces, and this is strengthened by the cohesion brought about by the dipolar character of the layers (Giese, 1973; Cruz *et al*., 1973; Tunney and Detellier, 1993). Therefore, a comparatively high amount of energy is required to separate the layers (Giese, 1978) and only certain compounds are able to access the interlayer space (discussed in next section). Yet, once access to its interlayer has been made possible by intercalation of intermediate exchangeable compounds, its asymmetric interlayer, containing both Si-O- and Al-OH sites on the siloxane and oxy-hydroxy surfaces respectively, offers a greater range of sites for covalent bond formation as compared to the “sandwiched” 2:1 clay minerals. Hence, the potential of this abundant clay mineral merits greater scientific study.

1.2. Chemical modifications of kaolinite

1.2.1. Historical feats in kaolinite intercalation

When Wada (1961) first managed to insert salts of organic acids in the interlayer space of kaolinite, he paved the way to a new domain in clay science (Raussell-Colom and Serratosa, 1987). Initially denominated as *intersalation*, the process was soon renamed as *intercalation* when insertion of other compounds – among which urea, formamide and dimethylsulphoxide – was also reported (e.g. Weiss, 1961; Ledoux and White, 1966). In these reactions the molecules act as wedges that penetrate the interlayer space from the edge towards the centre (Raussell-Colom and Serratosa, 1987). From the reaction rate equation postulated by Weiss *et al*. (1969 cited in Raussell-Colom and Serratosa, 1987), it follows that intercalation occurs more effectively in larger than small particles, because of an enclosing "ring mechanism" from many edge-nucleation sites in the former, while intercalation in the latter will cause a contraction of its neighbouring interlayers.

Summarizing previous work on kaolinite intercalation, molecules that succeed at independently accessing the interlayer space of kaolinite can be classified as follows: (1) organic acid salts with low molecular weight, big monovalent cations and low hydration energy (e.g. acetates); (2) compounds with strong hydrogen-bond-formation tendencies (e.g. urea); (3) molecules with a high dipole moment or mesomeric structures (e.g. dimethylsulphoxide); (4) molecules with combinations of these properties (Raussell-Colom and Serratosa, 1987).

These intercalation processes are useful to detect different degrees of order in kaolinite as well as the presence of polymorphs whose interlayer is not accessible by the intercalant, such that its d-spacing remains undisturbed, allowing discrimination between mineral phases by XRD (Ruiz Cruz and Franco Duro, 1999; Wada, 1961; Churchman, 1990). Dimethyl sulfoxide can be used to discriminate between chlorite and kaolinite for example. The second application of intercalation, relevant to this study, is to prepare a kaolinite precursor in which its layers have already been separated for a follow-up intercalation of a compound that would not be able to react directly with the clay mineral.

1.2.2. Clay nanocomposite materials

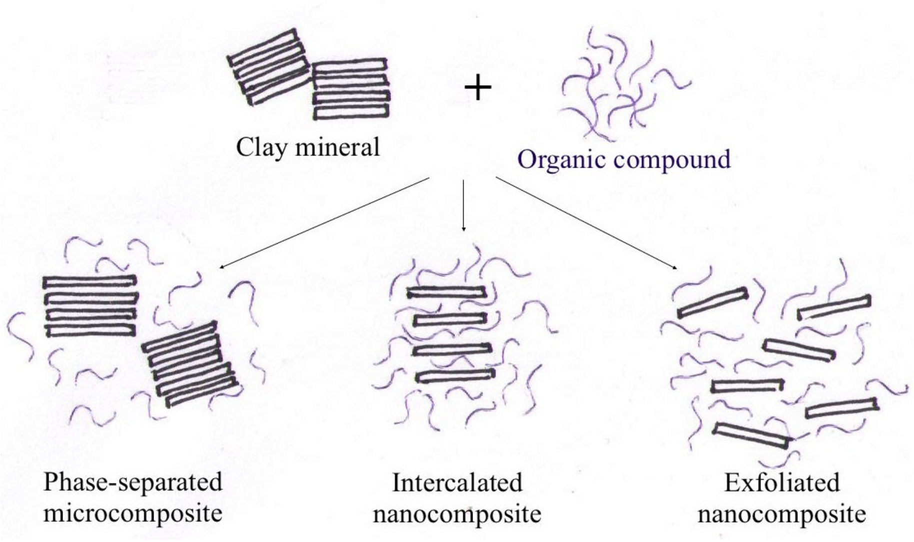

Figure 1.2.1. Diagrammatic representation of the nomenclature of different types of clay composite materials (adapted and redrawn from Alexandre and Dubois, 2000).

Nanocomposites are defined as those materials that have at least one dimension at the nano-scale range (i.e. smaller than 1 μm): sheets (e.g. clays), nanotubes and isodimensional nanoparticles (in order of increasing number of nanometer-range dimensions; Alexandre and Dubois, 2000). Methodologies to obtain intercalated or exfoliated nanocomposites include exfoliation-adsorption, in-situ intercalation/polymerization, melt intercalation, and from concentrated solution (Raussell-Colom and Serratosa, 1987; Alexandre and Dubois, 2000). Both in-situ intercalation and melt intercalation were employed in this study, as well as milling with a solid intercalant. Clay nanocomposites usually involved the association of clay minerals with an organic moiety, where intercalated and/or exfoliated composites can be obtained (Fig. 1.2.1). Alexandre and Dubois (2000) defined two main orientations of alkyl chains inside clay layers, each of which may exist as a monolayer or a bilayer, depending on the packing density and chain length: (1) as a lateral layer of the chain lying parallel to the clay layers, or (2) as a paraffin-type layer of molecules radiating away from the clay surface.

In addition to Figure 1.2.1, it may be worthwhile to note that exfoliation only occurs when the individual clay mineral layers are far enough apart to experience no more interaction (Ruiz-Hitzky and van Meerbeek, 2006). In reality, clay mineral nanocomposites cover a spectrum of purely intercalated, to partially delaminated (or exfoliated), to purely exfoliated, where there are very few examples of the latter (Ruiz-Hitzky and van Meerbeek, 2006). Intercalation, delamination and/or exfoliation of kaolinite can greatly enhance the range of applications for which the otherwise robust kaolinite mineral can be used.

1.2.3. Grafting of kaolinite

Chemical modification of kaolinite may improve its adsorbent properties by enabling access to its otherwise inaccessible interlayer space hosting reactive hydroxyl groups of the octahedral sheet, and by adding the functionality of an intercalated compound. If grafting of the intercalant can be obtained by covalently bonding to the clay mineral surface, a product of greater stability can be obtained than by means of ion-exchange or physisorption (Mercier and Detellier, 1995). Grafting of kaolinite is often performed on previously prepared dimethylsulfoxide- (DMSO) or urea-kaolinite (Letaief and Detellier, 2006), as was done in this study.

The first internally grafted kaolinites were reported by Tunney and Detellier (1993), who successfully grafted different alcohols onto the inner octahedral surface in DMSO- and *N*-methylformamide precursors. The functionality that was affixed to the kaolinite samples in the present study was a sulfur-containing chelating compound with the aim of improving its metal sorption ability in wastewater. The remainder of this chapter will therefore revolve around heavy metals in the context of wastewater, followed by a discussion about the ability of kaolinite for heavy metal sorption.

1.3. Heavy metals in wastewater

There is some debate about the definition of a heavy metal. Following Appenroth (2010), the term *heavy metal* refers to the transition elements, rare earth elements (lanthanide and actinide series), and the lead-group elements. In this work the heavy metal analytes are copper, zinc, nickel, arsenic, lead, cadmium and mercury, as well as chromium, manganese and iron, and zinc will have a central role.

1.3.1. Environmental concerns of heavy metals

Heavy metals are non-degradable and their persistence constitutes many ecotoxicological ramifications as their concentrations can build up in water or soil systems and animal tissues (bioconcentration and biomagnification). In trace quantities some heavy metal species, such as copper and zinc, perform critical biological roles in humans, animals and vascular plants, including as components of enzymes, anti-inflammatory agents, and cell-mediated immune functions (Prasad, 2009; Dimirkou *et al*., 2002). However, their persistence causes them to be generally hazardous. Their life-threatening impacts range from impacts on nervous functions, metabolism, blood composition, functioning of vital organs, and with chronic exposure symptoms that can be similar to those of Parkinson's disease, Alzheimer's and multiple sclerosis (Kurniawan *et al*., 2015). Zinc overdose can cause stomach cramps, vomiting, nausea, anaemia, and skin irritations (Gautam *et al*., 2015). On a more ecological scale, a recent study suggests greenhouse gas emissions increase in heavy-metal-polluted agricultural soils, coupled to decreased soil organic carbon content and microbial biomass, resulting in a lower crop productivity (Bian *et al*., 2015).

Depending on the country, drinking water limits for zinc range from 0.1 to 5 mg/L and surface water standards for zinc and copper have been set to 5 and 1.3 mg/L respectively by the United States Environmental Protection Agency (Gautam *et al*., 2015; Kurniawan *et al*., 2015). Such limits may not always be sufficient for smaller organisms. For instance, a copper concentration of 0.01 µg/mL can be lethal to green algae (Bowen, 1966 cited in Jackson, 1998), while drinking water limits of copper have been set at 3 mg/L by the European community and 1.0 mg/L by the US EPA (Gautam *et al*., 2015). The United States Environmental Protection Agency (EPA), among others, bases its industrial effluent standards on the performance of existing treatment methods. Logically, if one wishes to improve standards for the sake of environmental protection, the treatment methodologies need to be improved and be widely available and affordable.

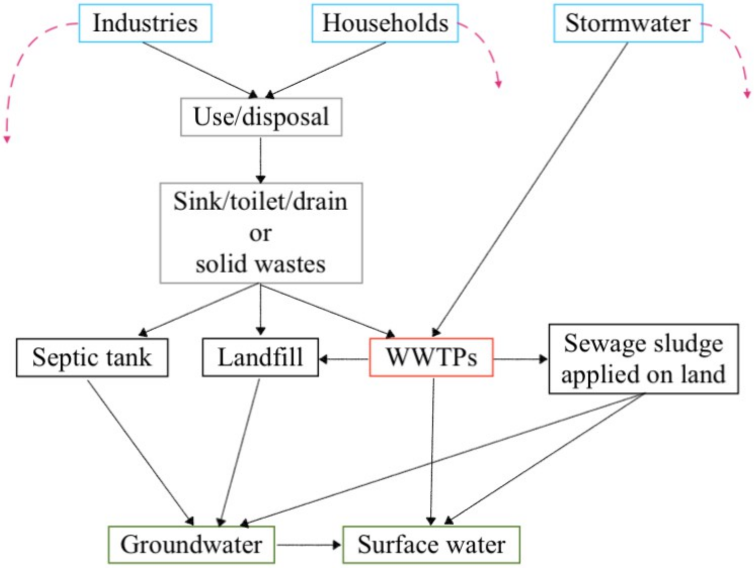

Figure 1.3.1. Possible entry pathways of heavy metals to the aquatic environment and the position of wastewater treatment plants (WWTPs) in the public water infrastructure. Dashed red arrows indicate potential direct leaks into environment (Inspired by Health Canada, 2012).

Figure 1.3.1. shows a selection of the anthropogenic cycle of heavy metals in water, their entry pathways into the environment, and the central role of wastewater treatment plants. Human exposure may then occur by direct or indirect use of contaminated ground- and surface waters, such as plant uptake from sludge-fertilized or treated wastewater-irrigated (Stietiya *et al*., 2014) agricultural soils and subsequent ingestion, eating animals from higher trophic levels whose food intake has led to biomagnification in their tissues, or any other pathway via inhalation, ingestion and skin absorption (Kurniawan *et al*., 2015). Also the air may be contaminated with dust particles containing heavy-metals, e.g. from mining and

processing of zinc ores (Gautam *et al*., 2015) or waste incineration. Apart from landfilling and incineration, recycling of heavy metals also occurs, though the latter is often not practical due to insufficient concentrations and inadequate conditions for convenient separation and recycling (European Commission, 2002).

In short, heavy metal contamination in the environment is a concern, and further study of effective yet inexpensive clay-mineral-based sorbents may prove to be very useful towards a more considerate relationship with the geochemical cycling that has been interrupted and diverted by our industrial developments.

1.3.2. Existing wastewater treatment processes

Wastewater treatment plants play an important role in remediating contaminants in water before re-entering the environment. For clay minerals to be used in the remediation of heavy metals from wastewater, it is useful to be aware of the current practices to be able to envision how such a technique could eventually be implemented. The description below will focus on the process of typical municipal wastewater treatment plant, such as the one at the Robert O. Pickard Environmental Centre in Ottawa, and go over some treatment possibilities of heavy metals in wastewater.

Typically, wastewater treatment plants perform so-called primary and secondary treatment stages, removing contaminants in settling tanks where oil and grease are skimmed off, by microbial degradation, and by sorption to solid substances, all of which will end up in the sludge (Monteiro and Boxall, 2010; Carballa *et al*., 2004; Figure 1.3.2). Occasionally a tertiary treatment stage may be applied, such as filtration by sand and/or activated carbon, nutrient removal, and disinfection with chlorine, UV, or ozone (Monteiro and Boxall, 2010). At the end of the treatment, the effluent is usually released to surface waters and the solid waste (sludge) incinerated, landfilled, or turned into a fertilizer (excepting some activated sludge, which is recycled within the wastewater treatment plant to maintain the bacterial culture; Monteiro and Boxall, 2010). However, conventional treatment methods are not always sufficient for the removal of all heavy metal species.

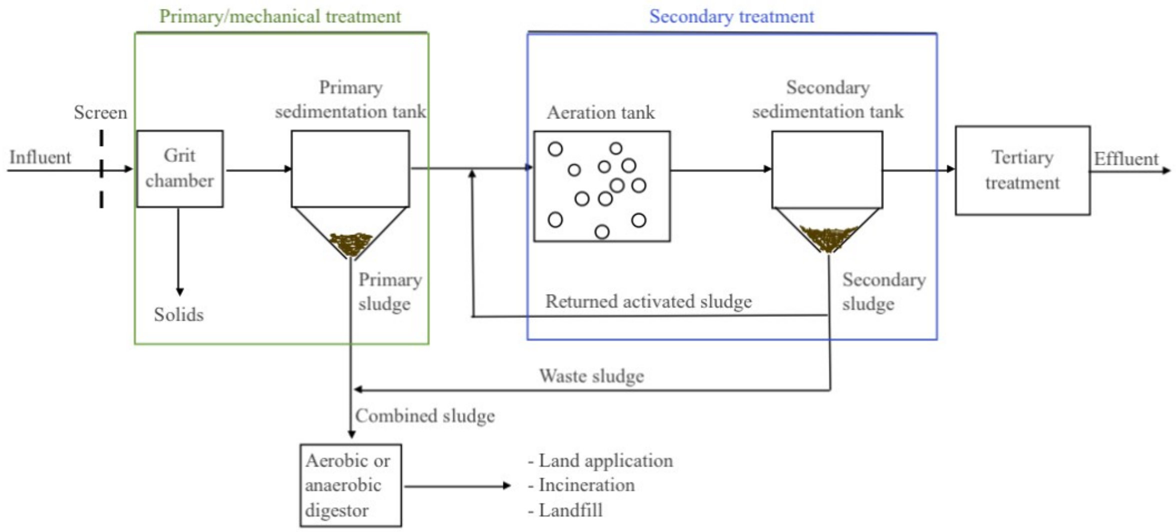

Figure 1.3.2. Schematic representation of a typical wastewater treatment process (adapted and redrawn from Monteiro and Boxall, 2010).

Incoming raw sewage water and effluent are frequently monitored at a treatment plant. Measured properties include the carbonaceous biological oxygen demand (cBOD), which is a proxy for the amount of organic pollution in the water. It is tested by the conventional $CBOD_5$ test, which measured the amount of O_2 consumed during a certain amount of incubation time as organics are being degraded. Total suspended solids (TSS) are also assessed by weighing the amount of solids filtered out by a pre-weighted glass-fibre filter from a certain amount of wastewater, reported in g/L. The parameters of most interest to authorities, as part of the wastewater systems effluent regulations, are suspended solids, BOD, and un-ionized ammonia (Fisheries Act, 2010).

Existing methodologies to remove heavy metals from wastewater when the standard process is not sufficient include: (1) precipitation and coagulation, but this usually involves dangerous chemicals, is not appropriate for low concentrations, and increases sludge volumes produced; (2) ion exchange, which effectively reduces concentrations to very low levels but is expensive and easily perturbed by organics and suspended solids; (3) membrane filtration typically by polymer film reverse osmosis, which can reach a removal efficiency of over 99% but is also very expensive and sensitive; (4) bioremediation, which involves clean-up by plants and microorganisms, e.g. in constructed wetlands or by growing plants that tolerate and hyperaccumulate certain metal species in aboveground tissues (including Ni, Cu, Zn, As, Cd and Pb; Qureshi *et al.*, 1985); (5) heterogeneous photocatalysts; and (6) adsorption onto clay minerals, layered double hydroxides, biomass, magnetic nanoparticles, activated carbon, and zeolites (Gautam *et al.*, 2015; Bhattacharyya and Gupta, 2008). There are advantages and disadvantages related with each method, but adsorption has recently received a lot of attention due to its relatively low costs and high performance (Gautam *et al.*, 2015; Kurniawan *et al.*, 2015). Moreover it is a simple and versatile method – lending itself to remediation of trace amounts as well as in batch or continuous systems, for both organic and inorganic contaminants – and it yields relatively small amounts of sludge that has the potential to be regenerated to reuse the adsorbent material (Mohanty *et al.*, 2006). Clay minerals have especially gained popularity due to their capacity to sorb as well as exchange ions, and they are stable both chemically and mechanically, exhibit a large specific surface area, exhibit interesting structure and surface chemistry for functionalisation possibilities, and are abundant and inexpensive (Kurniawan *et al.*, 2015). Hence, they could become economically viable replacements for commercial activated carbons and ion exchangers currently in use (Kurniawan *et al.*, 2015).

1.3.3. Recent trends in municipal wastewater heavy metal content

Regulations for industrial point sources have become stricter in England and other developed nations like Canada, reducing the load of many toxic metals, while diffuse input persists, where particularly zinc and copper present a problem today (Comber and Gunn, 1996). While lead is still a major heavy metal contaminant of concern, the replacement of lead piping and the phasing out of leaded gasoline and paint have been quite effective at reducing concentrations, at least in Europe and North America, while zinc and copper seem to be on the rise (Comber and Gunn, 1996; Erickson *et al.*, 2013). Zinc and copper mainly originate from household use of personal care products (e.g. creams, ointments, make-up, deodorant, talcum powder, shampoo, aftershave), plumbing materials, and detergents (Comber and Gunn, 1996). On top of that, a survey of heavy metals entering agricultural soil in European countries found that atmospheric deposition was dominated by zinc, followed by copper and lead (the latter mostly in Poland and Hungary; Nicholson *et al*., 2003).

Even though sludge application as a soil fertilizer may seem to be a good use of resources, it does carry risks. Because metals are persistent, their removal before reaching discharge as an effluent inevitably means they must have concentrated (due to reduced volume) in the sludge. Indeed, with regards to sewage sludge applied to agricultural soil, zinc is seen as a primary concern because of its adverse effects on the soil microbial community (hence its use as an antimicrobial agent; Pasquet *et al*., 2014) as well as its relatively high crop bioavailability (Smith, 2009).

1.4. The use of kaolinite for the sorption of heavy metals

Clay minerals and their metal sorption abilities have been widely studied, both in terms of its roles in contaminated soils and as inexpensive sorbent materials of aqueous-phase contaminants. The high surface area and charged layers of clay minerals are two favourable adsorbent properties. They can be used as a means to remove heavy metal species from wastewaters and could even be used for metal recovery, where environmental pollution is not only remediated, but valuable metals such as copper, zinc, silver, and molybdenum in discharge waters are recovered for future (re)use (Saniedanesh *et al*., 2013).

1.4.1. Heavy metal sorption onto natural (unmodified) kaolinite

Studies on natural and modified kaolinite and smectite clay minerals typically demonstrate a higher sorption of heavy metals onto smectite (Bhattacharyya and Gupta, 2008), which can be attributed to its greater layer charge combined with easy access to the swellable interlayer and cleavage of the bonds between the layers, so that heavy metals can adsorb both onto edge sites as well as between the layers. Possible sorption sites on kaolinite include: (1) external oxygen surface of exposed tetrahedral sheets; (2) external hydroxyl surface of exposed octahedral sheets; (3) edge sites where the sheets are broken; (4) the interlayer space if accessible (Yariv, 2002; Bhattacharyya and Gupta, 2008). Typically the interlayer space is inaccessible in natural kaolinite minerals and the surfaces each constitute roughly 40% of the available sites, and the edges about 10-20% (Yariv, 2002). Some of the functional groups found on the edges are those associated with the aluminol sheet – exposed aluminium ions ($Al^{\partial+}$), aluminol-sheet hydroxyls (Al-O-H) and hydroxyl ions ($Al\text{-}OH_2^{\partial+}$), exposed aluminol oxygen ions ($Al\text{-}O^{\partial-}$) – and those associated with the siloxane sheet – exposed silicon ions ($Si^{\partial+}$), siloxane sheet hydroxyls (Si-O-H) and hydroxyl ions ($Si\text{-}OH_2^{\partial+}$), and exposed siloxane oxygen ions ($Si\text{-}O^{\partial-}$) (Yariv, 2002).

Charged surface sites on kaolinite, where sorption may occur, are usually classified as being pH-dependent – those originating from protonation/deprotonation reactions of terminal oxide sites – or pH-independent – those originating from cation substitution on the external surface compensating for layer charge (Bolland *et al.*, 1980). The pH-dependent sites are rather weakly bound because of the distance between the source of the charge – an isomorphic substitution in the clay layer – and the compensating cation (Bolland *et al.*, 1980). Since kaolinite is rather

Sorption mechanisms pertain to both physical and chemical processes. Physical adsorption processes include van der Waals forces (e.g. partitioning) and electrostatic outer-sphere complexation (e.g. ion exchange; Scheidegger and Sparks, 1996; Figure 1.4.1). Chemical adsorption processes include inner-sphere complexation (monodentate or bidentate), covalent bonding, hydrophobic bonding, hydrogen bonding, hydrogen bridges, and steric orientation effects (Scheidegger and Sparks, 1996; Stumm and Morgan, 1981 cited in ibidem; Figure 1.4.1). In the case of inner-sphere complexation on the siloxane surface, water molecules can no longer access the ditrigonal cavity, while in outer-surface complexation a water molecule is always positioned between the cation and the siloxane surface (Kurniawan *et al*., 2015). Due to dissociation of the hydroxyls on the octahedral surface, sorption on oxy-hydroxy sites most probably involves complexation as well (Kurniawan *et al*., 2015). A third category of uptake processes includes surface precipitation, coprecipitation and diffusion into the mineral crystal structure, though it should be noted that these are strictly speaking not considered as adsorption phenomena (Scheidegger and Sparks, 1996).

To be clear the term “sorption” is used to cover all three categories of processes described above, while “adsorption” refers to only the physical and chemical complexation processes mentioned in the first two categories. Though this terminology is not always consistent in the literature (Scheidegger and Sparks, 1996), many authors prefer to use the term sorption to include the whole range of relevant processes that are difficult to differentiate experimentally (Petrović *et al*., 1999).

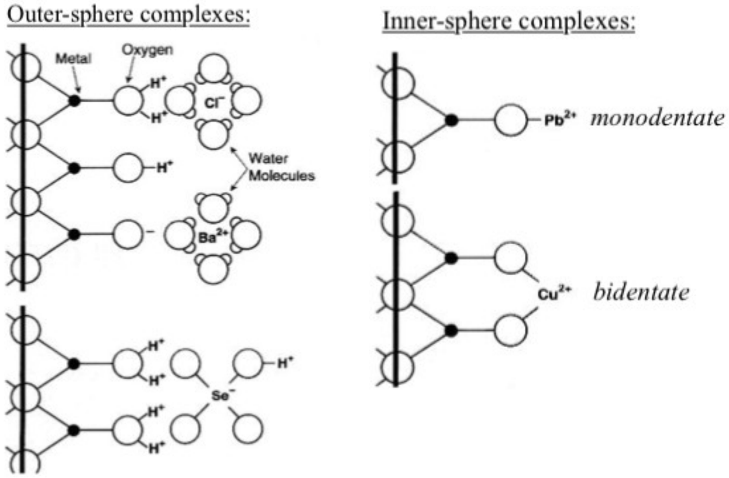

Figure 1.4.1. Surface sorption processes (adapted from Scheidegger and Sparks, 1996).

The inclusion of surface precipitation by using the term “sorption” is important for the purpose of this work because many heavy metals are, based on their ionic potential, likely to form surface precipitates (Johnston, 2005). The ionic potential is an expression of the ion-charge-to-radius ratio (i.e. surface-charge density) that affects resultant bonds. Elements with an ionic potential exceeding 95 (e.g. B, Cr, and Si) are more likely to form oxyanions, while elements with ionic potentials below 30 (e.g. Cd, Co, Cu, Mn(II), Ni, and Zn) tend to form soluble cations that can form precipitates in conjugation with elements that exhibit an intermediate ionic potential between 30 and 95 (e.g. Cr, Fe, Mn(III), and Mn (IV); Johnston, 2005). Once precipitation commences it can act like a nucleation agent, where Ni and Co are often attracted to precipitated Mn oxides, and Cu and Zn to Mn and/or Fe oxides (Johnston, 2005).

Sorption onto kaolinite includes the exchange of surface-hydrogen ions for heavy metals, which is both a pH dependent and pH-controlling uptake process as the exchange releases H^+ ions, increasing the pH of the surrounding solution (Bolland *et al*., 1980; Zhang *et al*., 2015). Replacement of H^+ ions for lead, zinc and cadmium cations may even cause swelling of the mineral, as well as flocculation, higher compressibility, hydraulic conductivity, and decreased shear strength (Zhang *et al*., 2015; Mitchell, 1993 in Miranda-Trevino and Coles, 2003), because metal adsorption onto kaolinite may cause reduced van der Waals forces between the kaolinite layers and create some internal spaces (Bhattacharyya and Gupta, 2008). Though such effects have been linked to the adsorption of lead, zinc, and cadmium, this process is poorly understood (Miranda-Trevino and Coles, 2003).

It is difficult to know what processes contribute to different metal uptake events and to what extent, and studies are still ongoing on this topic (Kurniawan *et al*., 2015). Considering precipitation of metal ion hydroxides formed in solution, this is believed to be a prominent process at heavy metal ion concentrations exceeding typical levels in natural water bodies and when the pH is neutral to alkaline (Jackson, 1998). Scheidegger and Sparks (1996) suggest that as the density of initially surface-complexed metals increases, nucleation drives the formation of aggregates that precipitate on the mineral surface. This continuum between adsorption and precipitation was also observed and described in a modelling study by Farley *et al*. (1985), which in turn was tested and found to match empirical observations of cadmium, manganese, zinc, and cobalt sorption onto calcite by Comans and Middelburg (1987).

Due to the interplay of the aforementioned factors, contact time is an important factor and may not always be a simple logarithmic relationship between time and metal sorption, as illustrated by the results obtained in a study by Miranda-Trevino and Coles (2003), who measured heavy metal uptake over a time span of 24 hours concomitantly with pH fluctuations. They demonstrate that Zn sorption by kaolinite brings about a marked initial decrease in pH followed by fluctuations, while sorption stabilizes within a 24-hour period (Fig. 1.4.2; Miranda-Trevino and Coles, 2003). Cadmium uptake, on the other hand, decreases over time while the pH increases (Fig. 1.4.3; Miranda-Trevino and Coles, 2003).

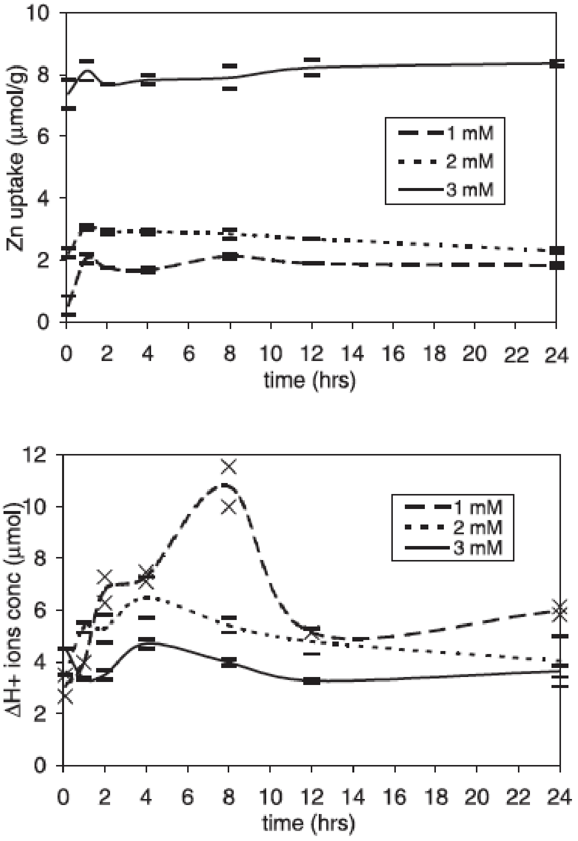

Figure 1.4.2. Zinc uptake by kaolinite over time (top) and the accompanying pH change (bottom) measured at three different initial metal concentrations (From Miranda-Trevino and Coles, 2003)[*].

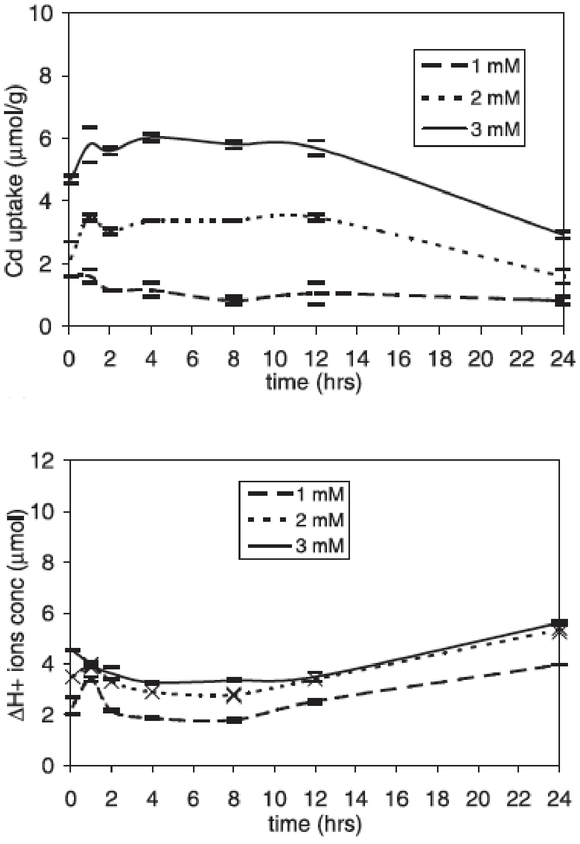

Figure 1.4.3. Cadmium uptake by kaolinite over time (top) and the accompanying pH change (bottom) measured at three different initial metal concentrations (From Miranda-Trevino and Coles, 2003)*.

---

[*] Reprinted from Applied Clay Science, 23, Miranda-Trevino, J. C. and Coles, C. A., Kaolinite properties, structure and influence of metal retention on pH, p. 136, 2003, with permission from Elsevier.

The sorption mechanism, its location on the clay mineral, and primary variables concerned depend on the surface area of the clay mineral, its layer charge, and reactive surface groups, as well as on the (heavy) metal species involved (Churchman, 2006).

According to Tiller (1996 cited in Churchman *et al.*, 2006), clay minerals have a higher affinity for heavy metal cations than for alkali and alkaline earth cations that are typically found as layer-charge-compensating species in the interlayer space of clay minerals, a favourable property for the purpose of this study though it also implies their presence in natural samples before their application in wastewater remediation. This is particularly true at high pH levels, which is thought to be due to a higher likelihood for heavy metals to hydrolyse (McBride, 1994). However, for metal substitution to take place, the ionic radii of the ions concerned can differ by maximum ~15%, such as Mg(II) (66 pm) replacement by Cr(VI) (63 pm), Ni(II) (69 pm), or Zn(II) (74 pm; Johnston, 2005).

1.4.2. Metal chelation by sulfur-containing compounds

Chelation, a word derived from the Greek *chelos* meaning claw, aptly describes the bonding of a metal ion by at least two separate binding sites of a polydentate (usually organic) chelating agent that typically contains sulfur, nitrogen, and/or oxygen as electron-donor atoms (Sears, 2013; IUPAC, 1997). They are used for detoxification in living beings where they may mobilize and chelate heavy metals from tissues to be excreted (Sears, 2013). Extreme pH levels are not favourable for the functioning of chelating agents as they are usually not stable at low pH, and at high pH metals often form insoluble hydroxides that can no longer be chelated (Flora and Pachauri, 2010).

The chelating ability of the -SH group is well known (e.g. Tandon *et al*., 1988). According to Johnston (2005), trace elements in the soil are more preferentially bound to sulfur than oxygen atoms, such that sulphide ore minerals found in nature release metals as they are weathered, particularly copper, lead and zinc.

The compound 3,6-dithia-1,8-octanediol has been studied in the past as a component of a chelating agent and its affinity for toxic metals. Mitchell and Jones (1978) prepared and studied several chelating agents, one of which contained 3,6-dithia-1,8-octanediol, and measured their affinity for mercury compared to calcium by mercury electrode titrations, finding a higher affinity for the former. Following were *in vivo* studies by Tandon *et al.* (1988), who demonstrated successful chelation and tissue removal of lead in intoxicated mice, by measurement of these metals in their urine and faeces during the experimental period and afterwards in their blood and tissues (Tandon *et al.*, 1988). It was concluded that the vicinal thioether groups, which have a low lipophillicity, are promising antidotes (Tandon *et al.*, 1988).

In June, while this study on thio-kaolinite was ongoing, da Silva *et al.* (2015) published a study on the synthesis of 3,6-dithia-1,8-octanediol-functionalised silica for the determination of lead concentrations in milk. Due to matrix effects of ICP-MS and other atomic spectrometry techniques used to measure lead concentrations, their objective was to develop a new and reusable pre-concentration technique for cheaper and more accurate determination of lead (da Silva *et al.*, 2015).

1.5.3. Heavy metal sorption onto organo-kaolinite minerals

There is a growing interest in the development of nanohybrid materials, including those made using clay minerals. Previous studies on modified clay minerals, albeit by organic complexation, hydroxyl interlayering, or pillaring, provide a solid indication that adsorption onto clay minerals can be significantly increased (Churchman *et al.*, 2006).

Compared to other clay minerals, kaolinite exhibits few adsorption sites, which can be attributed to its tightly packed structure and limited isomorphic substitutions. However, if the kaolinite layers could be stripped apart, via the processes mentioned in section 1.2.1, the octahedral OH-groups would be liberated. This may open up many possibilities, as these groups are very reactive, and also an advantage over 2:1 minerals as their octahedral sheets are covered in their sandwiched TOT structure.

Previously published modifications of intercalated precursor-kaolinites (see section 1.2.1) include the grafting of methoxy (e.g. Tunney and Detellier, 1996; Tan *et al*., 2015), long-chain alkyl amines (Gardolinski and Lagaly, 2005), quaternary ammonium (Letaief *et al*., 2008) and silane-bearing amine groups (Tonlé *et al*., 2007; Mbaye *et al*., 2014). The latter method has been taken a step further by exchanging chloro goups for NaSH to produce a thio-kaolinite material (Tonlé *et al*., 2011).

In this study a new thio-kaolinite is reported based on the grafting of 3,6-dithia-1,8-octanediol onto both urea- and DMSO precursors of two different kaolinite samples. Subsequently each sample was tested for its ability to sorb heavy metals from simple aqueous solutions as well as in a complex wastewater matrix. While on natural kaolinites metal sorption is expected to occur solely on its external surface, by ion-exchange and complexation mechanisms, it is hypothesised that modified samples will exhibit higher metal removal capacities due to additional sorption in accessible interlayer spaces and by chelation.

CHAPTER 2

Theory of main characterization techniques

In this chapter the characterization techniques relevant to this study are presented and the specifications of machines and settings used are detailed.

2.1. Powder X-ray diffraction

X-ray diffraction (XRD) is used to determine the crystallinity and crystal structure of a sample. It utilizes waves of very short wavelengths between 0.1 and 10Å, corresponding to the interlayer spacing of clays and associated earth minerals and the binding energies of inner-shell electrons. Consequently, interactions of X-rays with matter enables the production of characteristic X-rays that make up monochromatic beams, as well as constructively interfere on a crystal lattice to produce identifiable peaks characteristic of the mineral phases present in a sample.

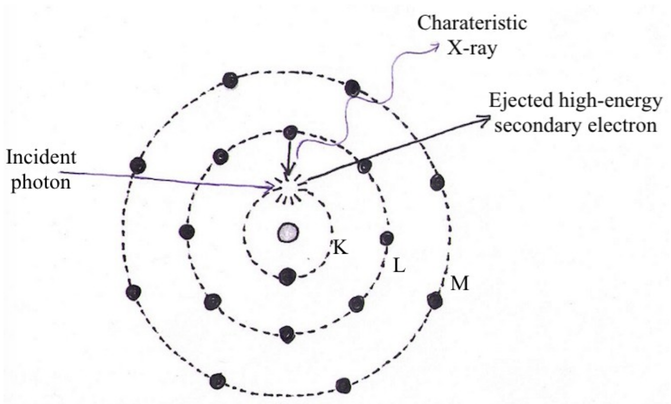

Figure 2.1.1. Schematic representation of the production of characteristic X-rays (adapted and redrawn from Fultz and Howe, 2013).

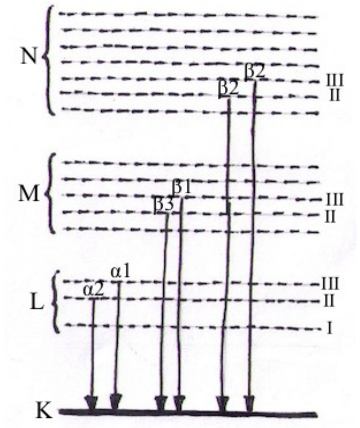

Figure 2.1.2. Characteristic X-rays produced by transitions following ejection of an inner shell electron (adapted and redrawn from Janssens, 2004).

A diffractometer's X-rays are produced by an X-ray tube in which high-energy electrons are produced and emitted onto a copper target (other metals may be used to produce characteristic X-rays of different wavelengths). By ejection of the copper's K-shell electrons, X-rays characteristic of its inner shell binding energy are produced (Fig. 2.1.1 and 2.1.2) with wavelengths that are appropriate for performing X-ray diffraction on a clay powder sample. Another process that also occurs when high-energy electrons are fired onto the target is inelastic scattering (Compton), which produces so-called brehmstralung, consisting of Kα, Kβ, etc. (Fig. 2.1.3). To perform XRD, the wavelength of $K\alpha_1$ and $K\alpha_2$ radiation are used. In order to refine the beam resulting from the summation of the ejection and inelastic scattering phenomena (Fig. 2.1.3), a nickel filter is inserted (for metal targets other than Cu a filter of the element z-1 is necessary) to absorbs Kβ radiation (Fig. 2.1.4).

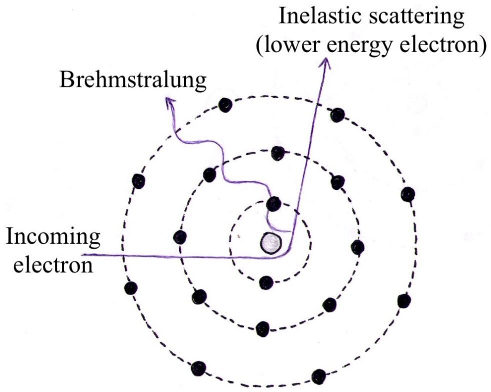

Fig. 2.1.3. Inelastic scattering that produces brehmstralung (adapted and redrawn from Fultz and Howe, 2013)

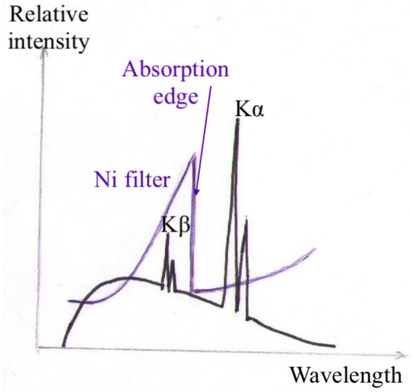

Figure 2.1.4. Graphical representation of the effect of the Ni filter (adapted and redrawn from Janssens, 2004).

The filtered X-ray beam is directed onto the sample where, upon interaction with the sample's atoms, elastic scattering (Rayleigh) occurs and produces a diffracted beam with the same energy as the incoming beam (Fig. 2.1.5). In order for the XRD phenomenon to occur and a peak to show up in the pattern, the radiation produced by the elastic scattering phenomena throughout the sample must be constructive rather than destructive.

Bragg's law is a central principle to understanding the theory of the XRD phenomenon. It relates the angle of incidence (θ) of an incoming monochromatic X-ray beam to its distance travelled from one lattice layer to the next, where the distance is a positive integer (n) multiple of the wavelength (λ). Hence, the distance (d) between the two lattice layers of the same Miller index (*hkl*) can be calculated from Bragg's Law:

$$n\lambda = 2d_{hkl} \sin\theta$$

When reflected X-rays are out of phase, they interact destructively, cancelling each other out, and the detected energy is low. On the other hand, when reflections are in phase, this translates into higher energy and greater intensity detected. Such constructive interference occurs when the incoming beam makes the same angle as the diffracted beam and such that it interacts with the electron clouds around regularly spaced atoms (Fig. 2.1.6). The interlayer spacing can then be calculated and is generally referred to as d-spacing.

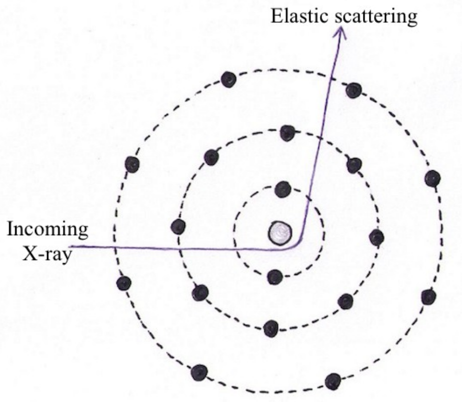

Fig. 2.1.5. Elastic scattering (adapted and redrawn from Fultz and Howe, 2013).

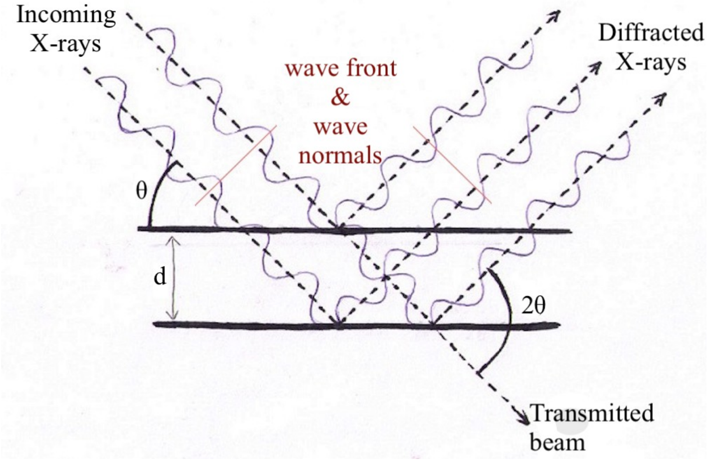

Fig. 2.1.6. Simplified diagram illustrating constructive interference for parallel planes according to Bragg's Law (adapted and redrawn from Brady and Weil, 2002; Reynolds, 1989).

A rather useful overview of different types of scattering produced by the XRD process (Fig. 2.1.7) has been provided by Jenkins (1989). He identifies the desired peaks' origin as well as the elements composing the background of a pattern.

	Source	Produces
a	Diffraction of required wavelength	Wanted peaks
b	Diffraction of other wavelengths	Unwanted peaks
c	Coherent scatter from sample	General background
d	Incoherent scatter from sample	General background
e	Scatter from sample support	Extra background at low angles
f	Fluorescence from sample	General background

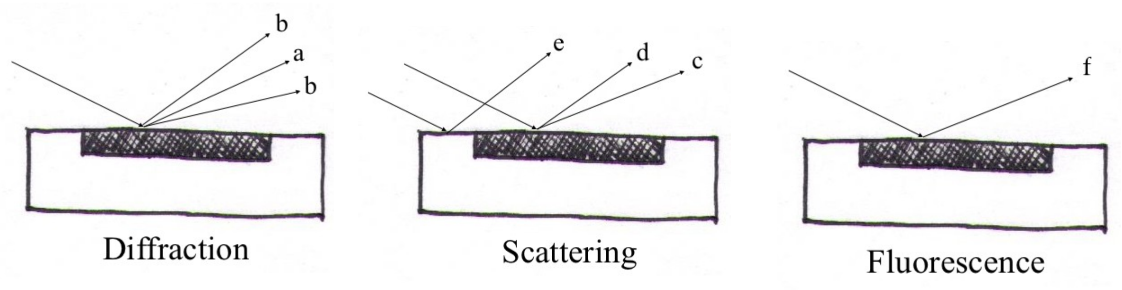

Figure 2.1.7. Composition of a typical XRD pattern (Redrawn from Jenkins, 1989)

Another issue may be that the beam angle is improperly detected due to a slight change in the position of the sample stage, or when there is an irregularity in the sample holder or sample itself, the baseline and beam angle detection may be shifted somewhat. Though careful sample preparation and use of the same sample holder throughout should mostly prevent this from happening, it is quite easily resolved by using several known peak positions in a reference pattern (e.g. kaolinite's d_{001} reflection) as a point of reference and to shift the pattern by the appropriate $^{o}2\theta$ if necessary. This is particularly useful when comparing oriented slides, where the thickness of the layer depends on the size and amount of clay in the air-dried drop pipetted onto a glass slide.

It should be noted that in powders, composed of many very small crystals oriented randomly, constructive interference occurs on periodicities along all directions, including all *hkl* planes in the sample. Therefore oriented slides can also be prepared where the *hkl* planes of all samples are parallel to one another. Clay minerals can then be more easily identified and semi-quantified. By treating the slide with ethylene-glycol smectite will swell, so it can be distinguished by observing an increase in d-spacing. Kaolinite and chlorite have the same d-spacing and can be distinguished from each other by heating an oriented slide to 500 ºC, when a kaolinite peak will disappear whereas chlorite will persist.

The intensity ($I_{(hkl)}$) of of the detected signal is determined by numerous factors, which can roughly be described by the following equation:

$$I_{(hkl)} = [F_{(hkl)}]^2 \times interference \times L_p \quad .$$

$F_{(hkl)}$ is the structure factor and depends on the number, nature and position of each atom in the unit cell. The interference function describes layer stacking according to Bragg's law. L_p is the Lorentz-polarization factor accounting for the fact that diffraction does not only occur at the angle predicted by Bragg's law but in a small range of 2θ angles (Lorentz). Moreover, it recognizes that X-rays are partially polarized resulting in reduced intensity (polarization).

Table 2.1.1. Peak areas and correction powers used (adapted from Martins *et al.*, 2007, cited in Costa *et al.*, 2011; Galhano *et al.*, 1999 and Oliveira *et al.*, 2002) for the range of d-spacings at which the corresponding mineral reflections were found in a samples; semi-quantification from the <63-µm powder fractions, unless stated otherwise.

Mineral	D-spacing	Correction factor
Phyllosilicates	4.41 - 4.46	0.1 or 0.2 depending on Sm content
Anatase	3.58	1
Quartz	3.34 - 3.35	2
Feldspars (K, Ca, and Na)	2.99	1
Dolomite	2.86	1
Siderite	2.79	1
Magnetite-Maghemite	2.52 - 2.60	1.3
Smectite (glycolated or air-dried oriented slide, <2µm)	14.75	4
Illite (air-dried oriented slide, <2 µm)	10.22	0.5
Kaolinite (air-dried oriented slide, <2µm)	7.07 - 7.26	1

Many sophisticated methods have been developed to perform quantitative phase analysis. However, in this work a simple semi-quantification was performed using the appropriate relative peak areas, which were subsequently divided by empirically estimated correction factors as outlined in Table 2.1.1. The peak occurring at about 4.46 Å is often used to estimate the phyllosilicate content of a sample because it represents the coinciding *110*- and *020* reflections of different dioctahedral clays (Środoń *et al.*, 2001). Following Galhano *et al.* (1999), a factor of 0.1 was used for phyllosilicates when no smectite was detected. The presence of kaolinite was confirmed by the disappearance of the relevant peak in the pattern of the heated oriented slide. Clay mineral fractions contained in the phyllosilicates were calculated from the <2-µm fraction.

Most analyses in this study were performed using powders, composed of many very small crystals oriented randomly so that there will be a certain number of crystals whose lattice planes will satisfy Bragg's law. In some cases oriented slides were also prepared.

XRD analyses were performed on a Philips PW3020 diffractometer operating at a voltage of 45 kV and a current of 40 mA. It uses a PW1830 X-ray generator with CuKα radiation consisting of a 1:1 ratio of $K\alpha_1$ and $K\alpha_2$ ($\lambda = 0.1542$ nm), a PW3719 beam angle tracker, and a Kevex detector (model 2005 212). Data collection was performed using X'Pert Data Collector 2.0e and X'Pert Data Viewer 1.0c (PANalytical B.V., Almelo, Netherlands). Scans were performed from 2 to 90° 2θ continuous, at a 0.02 step size, and a dwell time of 0.75 sec/step.

The following references were consulted for writing this section: Baron *et al*. (1971), Bish and Post (1989), Brady and Weil (2002), and Janssens (2004).

2.2. Nuclear magnetic resonance spectroscopy

NMR spectroscopy is based on the absorbance of electromagnetic radiation in the radio frequency range by atomic nuclei while the sample is subject to a stationary magnetic field (B_0).

Table 2.2.1. Spin number determination based on atomic mass and atomic number (adapted from Silversein and Webster, 1998)

Spin number (I)	Atomic mass	Atomic number	Example (I)
Half-integer	Odd	Odd or even	^{1}H(½), ^{13}C(½), ^{29}Si(½), ^{27}Al($^{5}/_{2}$)
Integer	Even	Odd	^{2}H(1)
Zero	Even	Even	^{12}C(0)

When the spin number (*I*) of the nuclei is not equal to zero (see Table 2.2.1), its charge “spins” and a magnetic dipole is generated along a nuclear axis, the magnitude of which is expressed as its magnetic moment μ (Fig. 2.2.1). The spin number *I* indicates how many nuclear orientations and associated energy levels will be effected by an external uniform magnetic field (B_0), according to the formula $2I + 1$. A proton (^1H) for instance, whose spin number is ½, exhibits 2(½)+1 = 2 energy levels, namely +½ and –½ (Fig. 2.2.2).

As described by the Boltzmann distribution, a slightly greater proportion of nuclei subject to B_0 exhibit the orientation that has a lower energy state (e.g. for H^+ this is +½). This brings about a measurable net magnetization (M_0) precessing at the Larmor frequency (ω_0) about B_0 situated along the z-axis (Fig. 2.2.1). At higher magnetic field strength of B_0, the energy difference between the two energy states increases (Fig. 2.2.2) as per the equation:

$\Delta E = \frac{h\gamma}{2\pi} B_0$, where h is Planck's constant, and γ is the gyromagnetic ratio (a proportionality constant between a nucleus' magnetic dipole μ moment and its spin I).

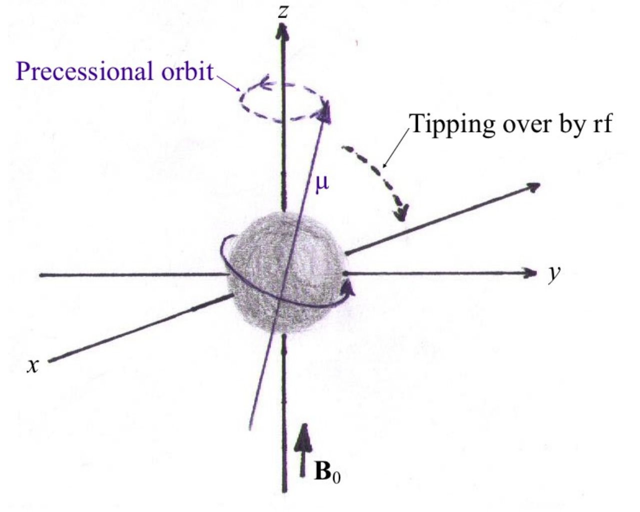

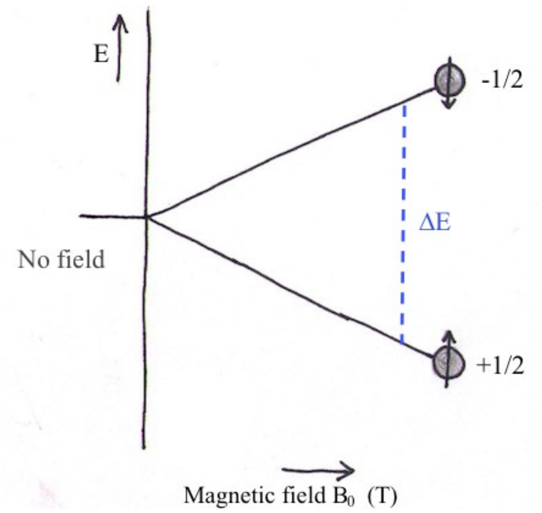

Figure 2.2.1. Diagram positioned in *xyz*-plane of reference of a spinning and precessing proton with a magnetic moment μ in the direction of a uniform magnetic field B_0, such that the net magnetization M_0 is in the same direction. Application of a r.f. pulse elicits a tipping of M_0 to the *xy*-plane. (Adapted and redrawn from Silverstein and Webster, 1998)

Figure 2.2.2. Nuclear spin energy level diagram for a spin I=1/2 nuclei: Zeeman splitting upon applied uniform magnetic field B_0. The energy difference between the two spin states increases as the external magnetic field is strengthened (adapted and redrawn from Silverstein and Webster, 1998).

In order to elicit a transition of a nucleus to a higher energy state, a rotating magnetic field at radiofrequency (r.f.) needs to be applied. Absorption is obtained by applying a r.f. (measured in MHz) with electromagnetic energy at the same frequency as ω_0. The net magnetization is then tipped towards the *xy*-plane that is at 90º from B_0. At this frequency the system is said to be in *resonance*. The further from the *z*-axis the resultant magnetization is tipped, the higher the peak intensity observed in the NMR spectrum (Goodman and Chudek, 1994; i.e. highest absorption is obtained at a pulse of exactly 90º).

Electrons closely around the nucleus provide a small amount of shielding from B_0, so that differing magnetic fields in different environments influence the nucleus' ω_0 and the exact frequency at which resonance occurs. Hence, it is possible to distinguish the number of environments present for the nucleus examined by measuring different chemical shifts (δ). In order to obtain accurate values of NMR frequencies and in order to compare results obtained with different machines operating at different frequencies, δ is measured in ppm relative to a standard. Smaller chemical shift values equate to larger shielding and v.v. (Kirkpatrick, 1988). Following the applied r.f. is the acquisition of the free induction decay (FID), detected by radio receivers, which is decomposed by Fourier transformation to obtain an NMR spectrum.

Due to zero spin on ^{12}C (see Table 2.2.1), NMR of the carbon nucleus can only be performed on ^{13}C. Due to its low natural abundance (1.1% of ^{12}C) and lower sensitivity than the ^{1}H nucleus, its overall sensitivity is about a 5700th that of ^{1}H (Silverstein and Webster, 1998). ^{29}Si, the second nucleus analysed in this work, has a natural abundance of only 4.7%. Both nuclei require special techniques to shorten the experimental time required. Moreover, while anisotropy is averaged out by tumbling of the nuclei in solution in liquid state NMR, such freedom of movement is impossible in solid samples, meaning the resulting peaks will be broad. To improve the resolution, specialist techniques are widely applied in solid state NMR, including magic-angle spinning (MAS), and cross-polarization (CP).

One of the issues with NMR analyses of clay minerals, is that the nuclei in its lattice structure exhibit a slow T_1 relaxation time. T_1 refers to the longitudinal- or spin-lattice relaxation time, which accounts for the resultant magnetism to return to the z-axis after the r.f. pulse. CP can be employed to overcome this in solid samples with an ordered structure if a magnetically dilute species with a long T_1 (such as ^{13}C and ^{29}Si) is bonded to an abundant species with a short T_1 (such as ^1H). In practice, a CP experiment is performed by applying an initial short 90° proton pulse, followed by a longer pulse to sustain their excited state. Meanwhile, an equally long pulse is applied at the resonating frequency of the dilute species (Fig. 2.2.3). Essentially the proton is sharing its energy with the dilute nucleus, which is "dragged along" with the proton's relaxation, reducing its T_1.

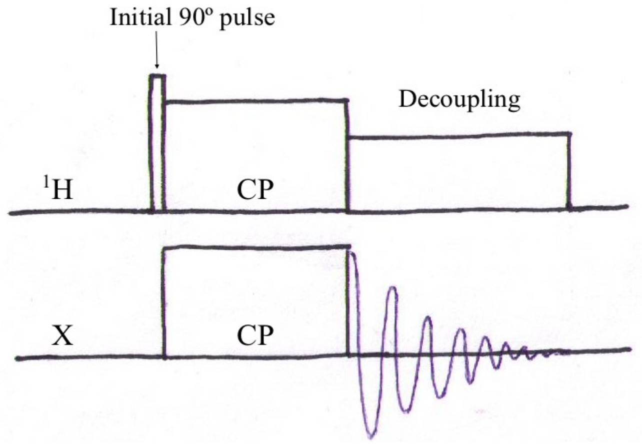

Figure 2.2.3. Pulse sequence diagram of a cross-polarization NMRexperiment (Adapted and redrawn from Goodman and Chudek, 1994; Conte *et al.*, 2004).

Figure 2.2.4. Bruker AVANCE III 200 NMR spectrometer instrument used in this study.

MAS is used to overcome the rigidity of solid-state samples in which anisotropy cannot be averaged out by simple moving about and toppling over of analyte species in a solution. There is an equation that describes anisotropy in solids which contains the factor $3\cos^2\theta - 1$, where θ is the angle between B_0 and the main nuclear axis (Goodman and Chudek, 1994). It has been worked out that this factor can be caused to vanish by rotation of the sample around the angle $\cos^{-1}(1/(3)^{½}) = 54.7°$ with respect to B_0 (Goodman and Chudek, 1994). That is the magic angle. Much sharper peaks can be obtained using this technique.

NMR spectroscopy was performed using a Bruker AVANCE III 200 solids spectrometer (Fig. 2.2.4) equipped with an Oxford Instruments 4.7-Tesla magnet (Oxford, England). All samples were prepared in a 7-mm zirconium rotor with a Kel-F cap (polychlorotrifluoroethene, whose C nuclei are not detected in ^{13}C NMR), inserted in a 7-mm Bruker CP-MAS probe and analysed at a spinning speed of 5000 Hz. All experiments were performed using magic-angle spinning (MAS) and ^{1}H-^{13}C or ^{1}H-^{29}Si cross polarization (CP) with a ramped ^{1}H contact pulse. Calibration to a reference was performed before each experiment. All ^{13}C CP-MAS spectra were referenced to glycine at a chemical shift of 176.5 ppm, and ^{29}Si CP-MAS spectra were referenced to tetrakis(trimethylsilyl)silane at -10.02 ppm, each relative to TMS. The experiment was halted when the signal to noise ratio was sufficiently high and/or little more improvement was possible within a reasonable amount of time, resulting in a varying number of scans for each sample that is specified in the relevant figure captions. Experiment settings are summarized in Table 2.2.2.

Table 2.2.2. Experimental settings used in all ^{13}C and ^{29}Si CP-MAS experiments. Settings for urea analysis are mentioned separately as they had to be adjusted for ineffective transferral of the cross-polarization pulse.

	^{13}C	^{13}C urea	^{29}Si
^{1}H 90° pulse	3.10 μs	4.20 μs	3.45 μs
Contact time	2000 μs	1000 μs	10000 μs
Acquisition time	0.0499972 s	0.0254452 s	0.0233972 s
Recycle delay	3.00 s	600.00 s	2.00 s
Spectral width	20161.291 Hz	20161.29	21929.824 Hz
Number of points	2014	1024	1024
Number of scans	See relevant figure caption	112	See relevant figure caption

Data processing was performed with the programme Bruker Top-Spin, applying Fourier transformation and exponential multiply while maintaining any applied phase correction (efp), followed by an automatic phase correction (apk), and a baseline correction (abs). Line broadening (lb) of 0 Hz was used, unless otherwise noted in the appropriate figure caption.

The following references were consulted to write this section: Silverstein *et al*. (1991), Goodman and Chudek (1994), Kirkpatrick (1988), Silverstein and Webster (1998), and Duer (2004).

2.3. Infrared spectroscopy

If one were only given a choice of one characterization technique to analyse a clay sample, infrared (IR) spectroscopy is claimed to be the most multifaceted, because it provides information about the chemical composition, isomorphous substitutions, as well as layer stacking order (Petit, 2006). IR spectroscopy employs electromagnetic radiation in the range between 10,000 cm^{-1} and 100 cm^{-1}. Upon interaction with matter, IR radiation may be transmitted, reflected, scattered, and absorbed. The latter is measured by detecting the difference of incoming radiation I_0 and transmitted radiation I as a function of wavelength. Absorption by molecular bonds occurs when the energy of the incoming radiation is in tune with the energy of their intrinsic vibrational modes, depending on the relative masses of the atoms concerned, the force constants of the bonds, and the geometry (Silverstein and Webster, 1998). Spectra typically show absorption or transmittance as a function of wavenumber v (cm^{-1}), which is the number of wavelengths per cm, i.e. $v = 1/\lambda$. The IR spectra presented in this work are in the range of 4000 – 400 cm^{-1}, but IR spectroscopy may also be performed in the near-IR range (14,290-4000 cm^{-1}) and the far-IR range (700-200 cm^{-1}).

Vibrational modes may be classified as follows: (1) stretching (v), a changing in bond lengths, and (2) bending (δ), a changing in bond angles, including more specifically (a) wagging (ω), a changing in the angle between the plane of a group of atoms; (b) twisting (τ), a changing in the angle between the planes of two groups of atoms; and (c) rocking (ρ), a changing in angle between a group of atoms (Figure 2.3.1). For non-linear molecules there are 3n-6 observable vibrations modes, as well as 3 rotational modes.

Because the wavelengths at which absorption occurs depends on many factors of the environment of molecular bonds, IR spectra are very intricate, particularly in the case of complex molecules such as clay minerals. Though IR spectroscopy triggers most relevant vibrations for clay minerals, some of the constituent minerals cannot be identified because their absorption bands are hidden by other components (Russell and Fraser, 1994). In this work the main interest of using IR spectroscopy is to perform a general identification of main absorption bands characteristic of kaolinite minerals and the other compounds used, and to be able to follow the modification of the clay minerals in detail.

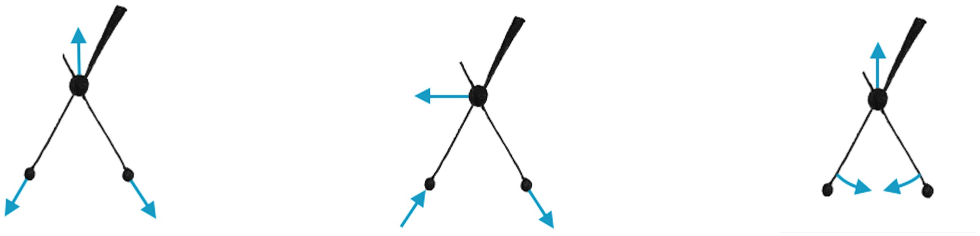

a) Symmetrical stretching (v_1) **b)** Asymmetrical stretching (v_3) **c)** In-plane bending/scissoring

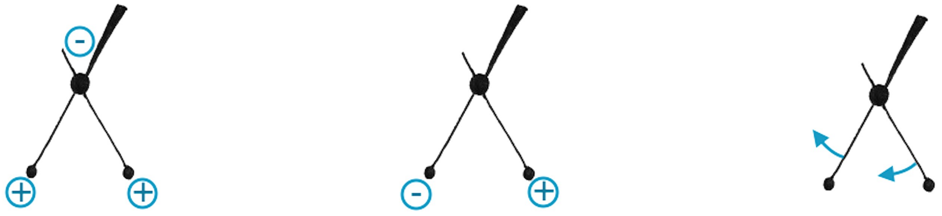

d) Out-of-plane bending/wagging **e)** Out-of-plane bending/twisting **f)** In-plane bending/rocking

Figure 2.3.1. Vibrational and rotational modes occurring when IR radiation is absorbed. + and – indicate movement into and out of the page. (Adapted and redrawn from Silverstein and Webster, 1998)

A Fourier Transform IR (FT-IR) spectrometer was used in this work. Its many advantages over the original dispersive type IR instruments include most notably the Felgett's advantage, describing the enhanced scanning speed as all wavelengths are simultaneously measured and a monochromator is no longer necessary, the Jacquinot advantage, pertaining to the improved sensitivity and reduced noise, and the Connes advantage, concerning the internal wavelength calibration made possible by a neon standard (Madejová *et al*., 2011).

FT-IR was performed using a Thermo Scientific Nicolet 6700 FT-IR machine with a Smart iTR diamond ATR fitting (Attenuated Total Reflection). In ATR spectroscopy IR radiation enters a prism of high refractive index material that transmits all IR radiation until it reaches the clay sample that is tightly pressed onto the diamond, which has a low refractive index such that some energy penetrates the sample, known as an evanescent wave (Petit, 2013). IR radiation must arrive on the sample at an angle (θ) that is greater than the critical angle (θ_c) (Fig. 2.3.2), otherwise it will be both transmitted and reflected. Distortion of the evanescent wave at the reflecting surface produces a spectrum that is converted by Fourier Transform. It is important to be aware of this piece of equipment, because the spectrum obtained with an ATR diamond is not identical to typical transmission experiments (Petit, 2013). Because the depth of penetration into the sample (typically a few micrometers) depends on the incoming wavelength, the relative peak intensities decrease at higher wavenumbers (King *et al.*, 2004), the region where OH stretching of kaolinite is observed. Moreover, the range of wavenumbers at which the sample can be tested is constrained.

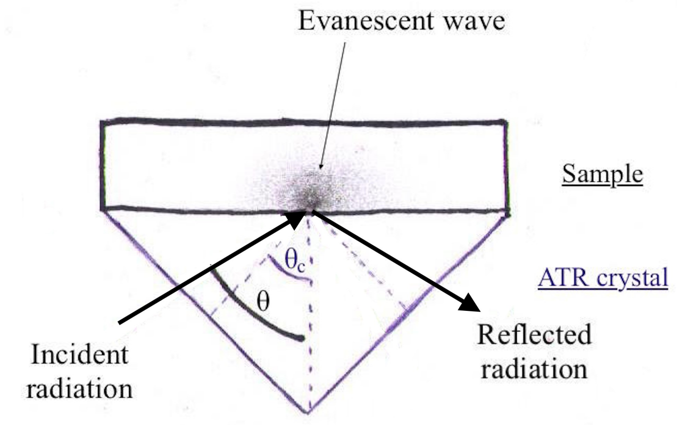

Figure 2.3.2. Diagrammatic representation of ATR spectroscopy (Adapted and redrawn from Petit, 2013).

Fortunately there are also several advantages to using an ATR device. Sample preparation can be somewhat tedious in transmission spectroscopy – thoroughly grinding to minimize scattering and mixing with KBr to make a pellet – while an ATR sample can simply be pressed onto the diamond, provided it does not react with it or scratch it. Furthermore atmospheric absorption is minimized, while in transmission spectroscopy the IR beam constantly passes through the atmosphere where CO_2 has absorption bands at 667, 1337, and 2349 cm^{-1} (Hirschmugl, 2004) and could be more affected by exhaled air.

Background measurements were performed before each run. Each run and background measurement consisted of 100 scans, at a resolution of 4, and a 0.483-cm^{-1} data spacing.

The following references were consulted to write this section: McMillan and Hofmeister (1988), Russell and Fraser (1994), Silverstein and Webster (1998), and King *et al*. (2004).

2.4. Thermogravimetric analysis

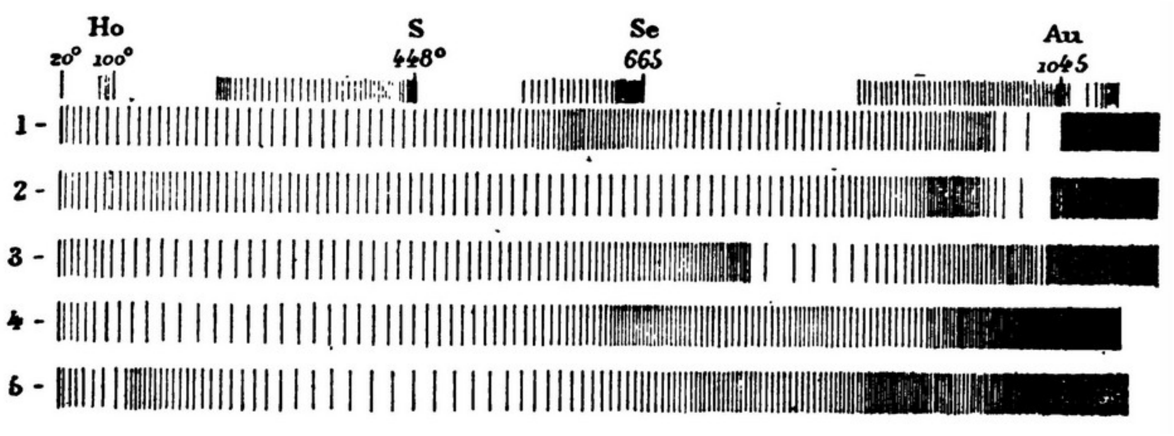

Figure 2.4.1. The heating-rate patterns of (1) halloysite; (2) allophane; (3) kaolinite; (4) pyrophyllite and (5) montmorillonite obtained by Le Chatelier (1887). The closer the spacing between the lines, the slower the heating rate. The boiling/melting points of water (Ho), S, Se, and Au are also shown along the top for reference.

Interestingly, most of the major advancements in the history of thermal analysis involved the study of clay minerals (Mackenzie, 1991), such as the application of the thermocouple by the first thermal analysis studies performed in the late 19th century by Le Chatelier (1887). As clay minerals had been identified mostly by their plastic properties and other observations by the human senses (Mckenzie, 1991), Le Chatelier (1887) wanted to determine their dehydroxylation temperatures and managed to distinguish 5 types of clay based on his observations upon gradually heating them. He observed certain stages where the temperature increase slowed down or suddenly increased (Fig. 2.4.1). The pattern at number 3 (Fig. 2.4.1) is kaolinite, exhibiting a marked slowing down of the heating rate until 770ºC (Le Chatelier, 1887). Le Chatelier's observations seems very similar to present-day DTA (differential thermal analysis), however his measurements were of heating-rate fluctuations (Mackenzie, 1991). During the 1930s thermal analysis became more wide-spread as it was often used as a cheaper alternative for (though it was actually a complement to) XRD for characterization of minerals (Plante *et al*., 2009; Mckenzie, 1991).

In thermal gravimetric analysis (TGA), today the most widely used thermal analysis technique, the change in mass of a sample is constantly measured as a function of increasing temperature under known environmental conditions (gaseous environment, pressure). Though it is a rather simple technique in principle, today's instruments exhibit extremely fine-tuned temperature and mass sensors, allowing very specific thermochemical decomposition patterns to be obtained.

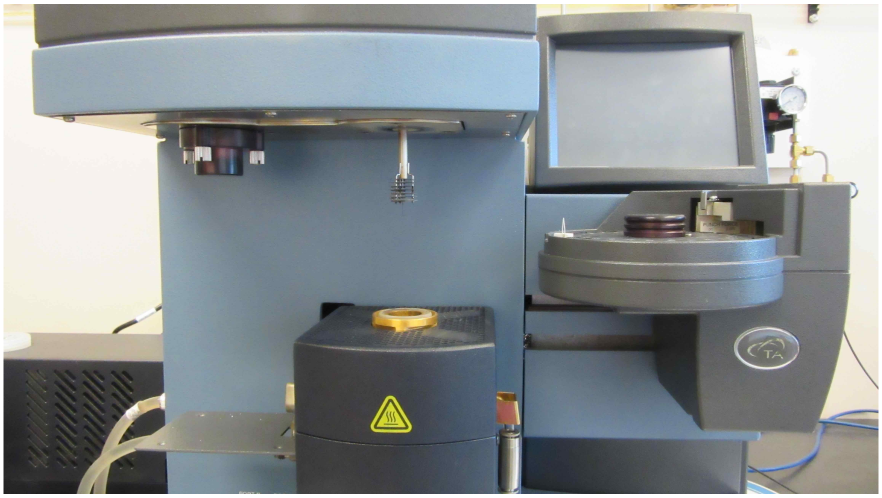

Figure 2.4.2. TA Instruments TGA Q5000 at the University of Ottawa.

Figure 2.4.2 shows the TGA instrumentation used in this study, consisting of one small vertically mobile furnace containing a chamber in which a sample pan, suspended from the hang-down wire, was positioned. After taring the scale of the instrument for the weight of an empty and cleaned sample pan, about 12 mg of clay powder sample was added. The pan was placed on the sample pan auto-sampler stage, from where the metal thread grabbed it and positioned it just above the furnace opening, which subsequently moved up and around the sample pan (Fig. 2.4.2). At this point, N_2 gas was turned on (balance purge flow rate of 10 mL/min and a sample purge flow rate of 25 mL/min) and the furnace heated up to a final temperature of 1000.0 ºC at a ramp of 10.00 ºC/min. Essentially, this process pyrolyses the sample. Though the gas, ramp and final temperature can be adjusted in the program settings, the experiments in this study were all performed as described here.

A TGA curve consists of the weight % of the initial sample mass remaining in the pan as a function of increasing temperature. The main components and information that can be extracted from a TGA curve are illustrated in figure 2.4.3. The percentage mass loss attributable to a certain mass loss event (e.g. dehydroxylation) is calculated from the y-value difference between the relevant stationary points (Fig. 2.4.3). The derivative of the resulting curve (DTG) is often included, as % mass loss/temperature unit, to clarify at what temperature the inflection point occurs.

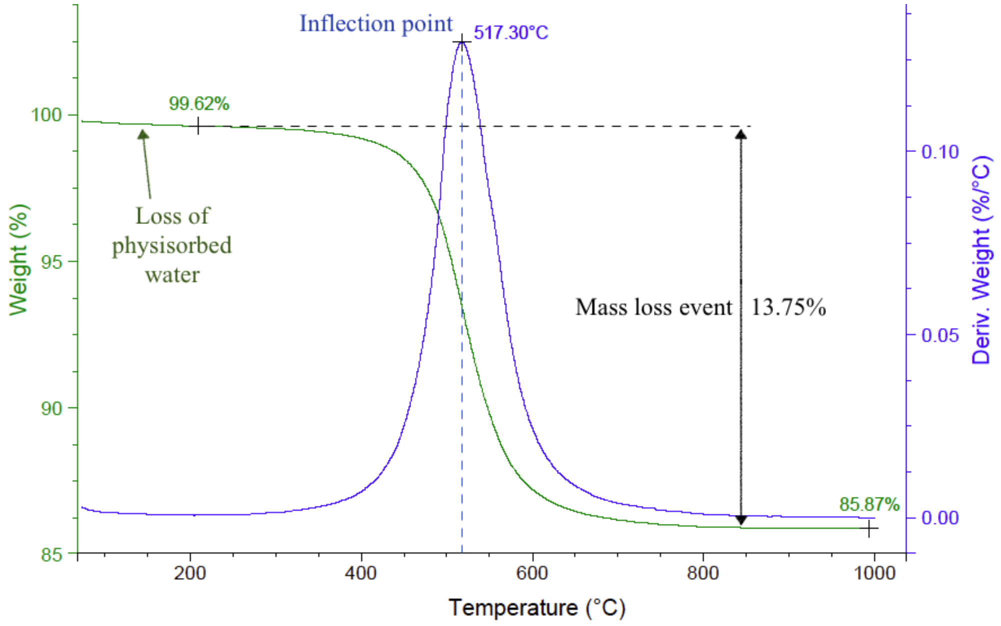

Figure 2.4.3. Example of a TGA curve of natural kaolinite and its essential information components.

TGA is very useful for determining the organic loading in the synthesis of organoclays, and to establish how the thermal stability of clay minerals changes when they are chemically modified. By comparing the TGA and DTG curve of an organoclay to the curves of its constituent products (the clay and the organic compound), it can provide information about the interaction between the clay and the organic matter (Yariv, 1991).

Thermogravimetric analysis (TGA) was performed using a TA Instruments TGA Q5000 with a high temperature platinum or alumina (Al_2O_3) 100 µL pan. Data collection was performed with Q Advantage, Thermal Advantage Release 5.4.0 (TA Instruments-Waters LLC, 2001-2011). Curves were then analysed and exported via TA Instruments Universal Analysis 2000, version 4.5A (TA Instruments, 1998-2007).

2.5. Inductively coupled plasma – mass spectrometry

Inductively coupled plasma – mass spectrometry (ICP-MS) is a widely used technique for measuring trace metal concentrations. It has very low detection limits, up to the ppt-level for most elements, and is appreciated for its ability to inherently perform multi-element analyses. The discussion that follows below essentially describes how the ICP-MS machinery controls how and what kind of particles travel to the eventual MS detector. The description below has been adapted to the ICP-MS machine used in this study, located in the geochemistry laboratory of the department of Earth and Environmental Sciences at the Advanced Research Centre at the University of Ottawa.

A plasma is a state of matter that is created by irradiating a gas, such as argon, separating positive ions and free electrons and forming an electrically neutral gas with a very high energy and temperature (about 6000 ºC). To produce an inductively coupled plasma, application of an oscillating radio frequency power passed through a coil wrapped around the torch (Fig. 2.5.1) couples with the argon gas. Formation of the inductively coupled plasma (ICP) is then initiated with some “seed” electrons sparked from a Tesla coil or a piezoelectric starter, which are accelerated by the oscillating r.f. field (Taylor, 2001).

The ICP is created in a torch composed of quartz. The torch has a central channel for sample introduction, surrounded by an argon-filled chamber where the plasma is formed that is encapsulated by a flow of cooling argon gas (Fig. 2.5.1). A constant low flow of auxiliary argon gas is pumped into the plasma chamber to push the ICP away and prevent melting (Taylor, 2001). Coolant argon gas is also introduced to prevent melting of the quartz and it stimulates formation of a doughnut (annular) shaped plasma around the central channel (Fig. 2.5.1. Taylor, 2001).

Liquid sample is introduced in the central channel of the torch as droplets that are dispersed into an aerosol by a nebulizer, as large droplets would cause disturbance. The nebulizer inserted in the ICP-MS used in this study was a Peltier-cooled spray chamber. As the aerosol droplets travel through the plasma "doughnut", thermal radiation on its constituent elements atomizes them and eventually ionizes the atoms. The latter occurs just past the high energy "doughnut" region of the ICP (Fig. 2.5.1).

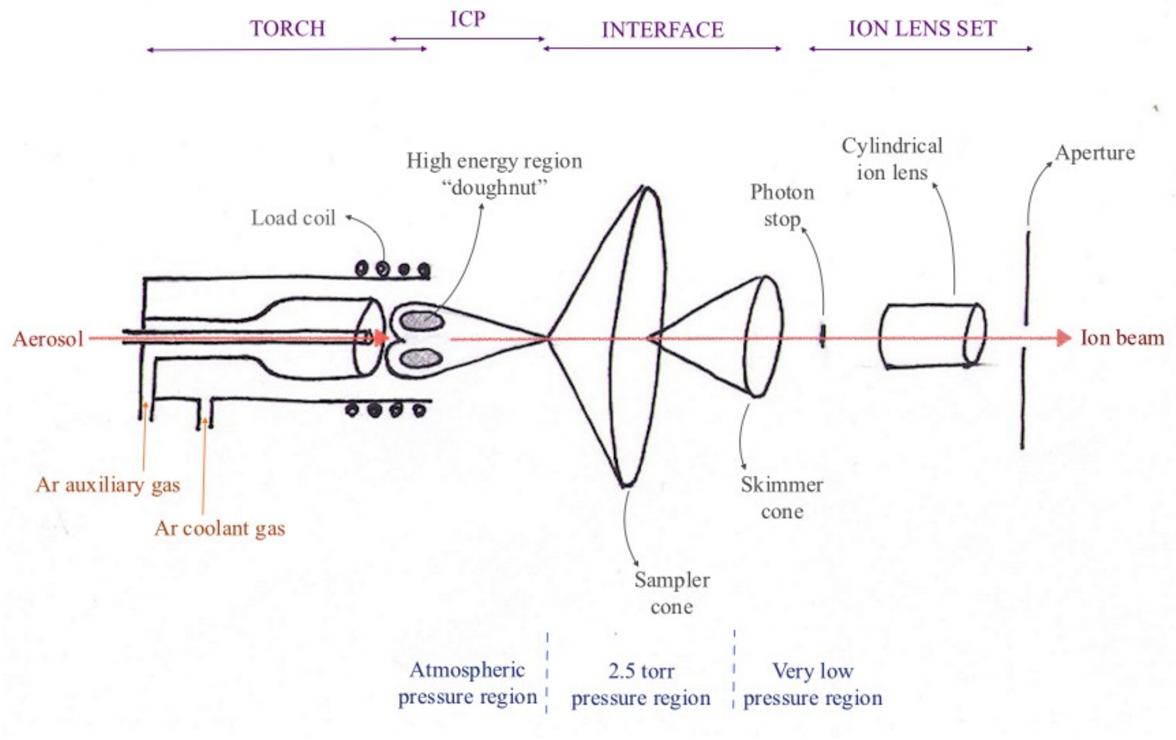

Figure 2.5.1. Diagram of a typical ICP torch, interface and ion lens set (adapted and redrawn from Taylor, 2001).

The ions then need to be transported safely to the mass spectrometer (MS). The interface ensures that the ions can pass from the 6000-ºC plasma to the MS operating at room temperature, as well as from a high pressure system to a (almost) vacuum. The interface is composed of at least two water-cooled Ni cones: an outside sampler cone with its 1-mm opening at the apex in the plasma, followed by the skimmer cone that has a <0.5-mm opening at its apex (Fig. 2.5.1.; Taylor, 2001). These cones extract an ion beam that is representative of the ion population passing through the plasma. Meanwhile, the pressure associated with the plasma is decreased by a vacuum pumping system (twin turbo vacuum system) to 10^{-5} torr or less, to ensure the MS can function properly and that ions can travel without resistance.

Subsequently, a photon stopper (Fig. 2.5.1) forms an obstruction for photons and neutral species produced by the ICP that would disturb the mass analyser and increase background noise. A negatively charged extraction electrode filters out positive ions that travel around the photon stopper, guided by positively charged lenses. They then pass through the electrostatic lens and finally through the entrance aperture of the MS (Fig. 2.5.1). The voltage of the ion lens is automatically fine-tuned during the experiment to approach optimum ion transport efficiency for the analytes.

Table 2.5.1. Some examples of analyte overlap by molecular ions causing interference and the CRC mode that can be used to overcome it (Agilent Technologies, Inc., 2009; Kogel and Lewis, 2001).

Analyte	Interfering ion	CRC mode
^{40}Ca	Ar	H_2 reaction mode
^{56}Fe	ArO	H_2 reaction mode
$^{39}K^+$	ArH^+	NH_3 reaction mode
^{56}Fe	$^{40}Ar^{16}O$, $^{40}Ca^{16}O$	
^{63}Cu	$^{40}Ar^{23}Na$, $^{12}C^{16}O^{35}Cl$, $^{12}C^{14}N^{37}Cl$, $^{31}P^{32}S$, $^{31}P^{16}O_2$	
^{75}As	$^{40}Ar^{34}SH$, $^{40}Ar^{35}Cl$, $^{40}Ca^{35}Cl$, $^{37}Cl_2H$	He collision mode
^{114}Cd	Sn	
^{66}Zn	TiO, TiOH	He collision mode

In some cases elements present in the plasma, solvent and sample matrix may combine to form molecular ions that cannot be discriminated from analytes because their masses are the same (Agilent Technologies, Inc., 2009; see Table 2.5.1.). Collision/reaction cells have been developed to overcome this problem by reducing the throughput of interfering ions. The ICP-MS used in this study was fitted with a 3rd generation Octopole Reaction System (ORS^3) collision/reaction cell (CRC), which operates in one of three main modes: no gas mode, reaction mode, and collision mode (Agilent Technologies, Inc., 2009). When the analytes tested for are known to have overlapping molecular ions, introduction of a gas into the cell through which the ion beam passes will either react (by using H_2 or NH_4 gas) or collide (by using He gas) with molecular ions to break them up and/or neutralize their charge. For example, ammonia can be used to neutralize and therefore remove $^{38}ArH^+$ from the ion beam, which interferes with the analyte $^{39}K^+$, as follows: $NH_3 + {}^{38}ArH^+ \rightarrow NH_4^+ + {}^{38}Ar^0$ (Taylor, 2001).

In the case of complex-matrix samples (such as wastewater), three major limitations for reaction mode may pose problems: (1) only those interfering ions that are reactive with the cell gas will be removed, such that other interfering ions will persist; (2) reaction products may include secondary interferences; and (3) reaction with and removal of analyte species (which may or may not be contained in molecular ions) by the cell gas will remove them from the ion beam, causing signal loss (Agilent Technologies, Inc., 2009; Taylor, 2001). In a technical overview by Agilent Technologies, Inc. (2009), comparing the different cell modes for complex matrices, it was concluded that collision mode using He produces more reliable results. Collision mode exploits the kinetic energy discrimination (KED) process, based on the occurrence that molecular ions are more likely to collide with the cell gas than their overlapped analytes of the same mass because they are larger (Agilent Technologies Inc., 2010). However, both collision and reaction mode decrease the signal of some of the analytes, reducing the limit of detection.

The mass spectrometer (MS) orders ions by their mass-to-charge ratio (m/z) which are counted by the detector. The so-called Triple Quad (QQQ) system includes two quadrupoles before and after the ORS: a Q1 that manages which ions are passed onto the ORS, and a Q2 that lets only the target analytes enter the detector (Agilent Technologies, Inc., 2014; Fig. 2.5.2). Quadrupoles consist of four parallel rods made of polished metal or metal-plated ceramic in a symmetrical configuration. Positive and negative combinations of direct currents and radio-frequency waves are applied to the rods such that two rods next to each other have opposing electrical charges and oscillate 180º out of phase (Fig. 2.5.2). The atoms in the ion beam passing through the space between the rods, which is adjusted to let only the target analyte (of a certain m/z) pass to the end of the Q1 unit, will start to spiral. The magnitude of the atoms' spiralling paths depends on their m/z, such that only the target analyte will reach the end of the quadrupole, while all other species will be deflected, collide with the rods, and are filtered out. Incidentally, these quadrupole units positioned before the reaction cell can overcome many of the interference mechanisms occurring in reaction mode of the ORS by acting as a mass filter, greatly enhancing results even compared to collision mode.

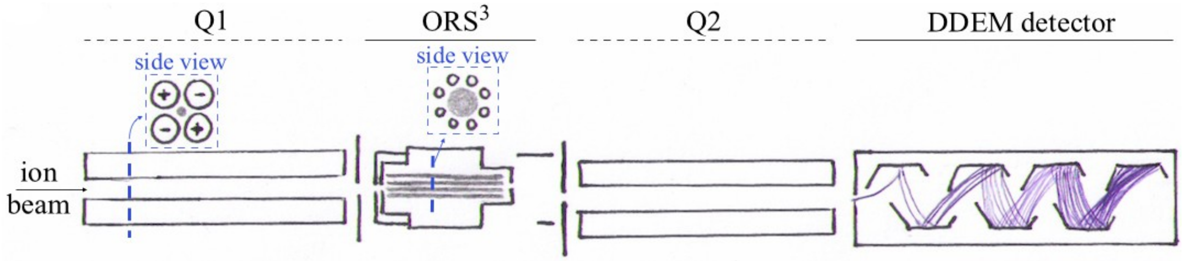

Figure 2.5.2. Schematic diagram of the route of the ion beam after passing through the cylindrical ion lens (Fig. 2.5.1.) in an Agilent Technologies 8800 ICP-MS Triple Quad. The beam passes through the first quadrupole (Q1), the 3rd generation octopole reaction system (ORS^3), the second quadrupole (Q2), and finally the discrete dynode electron multiplier (DDEM) detector (adapted and redrawn from Taylor, 2001; Agilent Technologies Inc., 2010b).

A second quadrupole (Q2) is located after the ORS (Fig. 2.5.2). The dual action of the two quadrupole units of the MS is referred to as MS/MS mode. All in all this QQQ configuration ideally filters out only those species that have a certain m/z, any molecular ions that may exist in this population are then broken up in the OCR system, and finally a second selection is performed to filter out the separated ions to be left with a single analyte beam of ions that are counted by the detector.

The detector is a discrete dynode electron multiplier (DDEM; Fig. 2.5.2), collection of dynode plates composed of a metal oxide so that two secondary electrons are ejected upon collision of the analyte ion with its surface. The plates are subject to a dc potential that augments at each successive plate so that the two ejected electrons are accelerated to the next plate, where 4 secondary electrons are ejected and accelerated, etc. to reach an amplification of the signal of 9 orders of magnitude. Finally the electron beam reaches a collector that produces a proportional electrical current.

In order to perform quantitative analysis, each run was preceded by the analysis of metal mixtures of a series of know concentrations (12.5, 25, 50, and 100 ppm of both mix A and mix B; 12.5 and 25.0 ppb of a separate Hg solution; Table 2.5.2) in relation to the measured ion current, from which calibration curves are produced. The accuracy of these calibration curves was assessed before proceeding to the analysis of the unknown samples.

Table 2.5.2. Calibration mixtures used, diluted from 100 ppm stock solutions prepared in 1% HNO_3.

Mix A	Al, As, B, Ba, Ca, Cd, Co, Cs, Cu, Fe, Mg, Mn, Mo, Ni, Pb, Si, Sc, Sr, Ti, V, Zn
Mix B	Na, K, P, S

When concentrations of certain metals are relatively high in the sample matrix, interference with other analytes can occur. For instance, high concentrations of Na (on the scale of 0.02 to 0.06 M) causes a 20 to 50% reduction in signal for Pb, Cu, and Li (Taylor, 2001). Likewise, high concentrations of heavier metals cause 20 to 70% reduction in the signal of those same metals. Therefore samples are often diluted with a weak solution of nitric acid (1%).

The machine used in this study was an Agilent Technologies 8800 ICP-MS (Triple Quad), coupled to an Agilent Technologies ICP-MS Autosampler (ASX-500 series). The sample uptake and stabilizing time were each 30 seconds, probe rinse of the sample and standard were each 10 seconds. The pump speed was 0.5 rpm, dwell time 0.1 sec (n=4), r.f. power 1550 W, sample depth 10 mm, and the sample gas flow 1.07 L/min. A series of 8 blanks (1% HNO_3) was inserted after calibration to calculate the limit of detection of each metal analyte. Every 12 samples a blank and a calibration standard of 12.5 ppm were inserted to check for drift.

The following references were consulted to write this section: Taylor (2001) and Agilent Technologies, Inc. (2014), and general explanations from Nimal De Silva (pers. Comm., 2015).

2.6. X-ray fluorescence

X-ray fluorescence (XRF) was used only once in this study, at the University of Aveiro, Portugal, to determine the oxide- and trace element composition of one sample. It had a very modest contribution to the data set, so only a short and basic explanation follows.

XRF is based on the production of characteristic radiation (see fig. 2.1.1). Fluorescence refers to the absorption of photons, followed by the emission of photons at a longer wavelength (lower energy). X-rays are directed onto a sample to eject high-energy inner-shell electrons. The electron vacancy is then filled up by an electron from a higher orbital, producing an X-ray of an energy equal to the energy difference between the orbitals involved. Therefore, the X-ray is characteristic of the atom from which it originates. From the spectrum subsequently obtained, elemental composition can be quantified.

CHAPTER 3
Material characterisation and modification

3.1. Chemical reagents

Dimethylsulfoxide (DMSO; Fisher Scientific, 99.9%), urea (Sigma-Aldrich, ACS reagent, 99.0-100.5%), 3,6-dithia-1,8-octanediol (DTOD; Sigma-Aldrich, 97%), and isopropanol (solvent grade) were used without further purification. Solutions of 0.1 M hydrochloric acid and 0.1 M sodium hydroxide were prepared by dissolution of the appropriate quantities of HCl (12.405-M HCl; Fisher Scientific Canada) or NaOH with deionized water.

3.1. Sample collection and preparation

In this work two clay samples were used: KGa-1b, a reference kaolinite which was obtained from the Source Clay Repository of the Clay Minerals Society, located at Purdue University, West Lafayette, IN, United States; and SP (São Pedro), which was chosen for its high kaolinite content amongst a set of four clay samples that were characterized at the University of Aveiro, Portugal (Appendix A). KGa-1b has been characterised as part of an extensive series of Baseline Studies of the Clay Minerals Society Source Clays, from which relevant information has been extracted and included in Appendix B.

KGa-1b is obtained from a deposit located in the Buffalo Creek Formation in Georgia, United States, dating back to the Cretaceous time period, that contains a kaolin strata of 11 m thick (Moll, 2001). KGa-1b is a so-called *soft* kaolinite with few defects, a low Fe content (0.10-0.45% in weight Fe_2O_3), 1-2% in weight of Ti-rich minerals, and 0.1-0.04% in weight of organic matter (Moll, 2001). Data on the elemental composition and trace-element chemistry of KGa-1b are included in Appendix B.

Sample SP was sourced from Gresco & Grés, Lda, a ceramic factory in the area of Taveiro, Portugal, principally involved in the manufacture of tiles. It was taken directly from the filter press on the company's site (Fig. 3.2.1b), which is typically employed in this industry when clay pretreatment involves wet milling and/or when it is soaked in water to improve its plasticity (Zamek, 2006; Millberg, n.d.). The clay is sourced from the direct surroundings belonging to the Taveiro Formation, a deposit dating back to the Upper Cretaceous (Fig. 3.2.1c). The Taveiro Formation is known for its simple mineral assortments of illite, smectite as well as some kaolinite towards the southern end of the formation where SP is located – a distinct deposit compared to others belonging to the same formation (Galhano *et al*., 1999; Rocha and Gomes, 2003). The accessory mineral portion is also quite simple, containing mostly quartz, K-feldspar and sporadic presence of dolomite, anhydrite and anatase (Galhano *et al*., 1999). Apart from a higher kaolinite content, the southern region exhibits higher Al_2O_3 and Fe_2O_3 contents, and lower MgO and CaO levels, which corresponds with the increased kaolinite and decreased smectite contents (Rocha and Gomes, 2003). Trace element analysis was performed by XRF to determine heavy metal species already present.

The <63-µm fraction of SP was collected by wet sieving. First about 500 g of the bulk sample was suspended in deionized water, and mixed using a mechanical mixer (Heidolph). The dispersion was then passed through a <65-µm sieve, aided with additional deionized water. The collected clay fractions were oven-dried at 50 ºC and subsequently ground by an agate mortar and pestle to obtain a fine powder.

Both clays were further purified to remove impurities by sedimentation techniques. Clay fractions under 2 µm of sample SP were collected by sedimentation conform to Stoke's Law at the University of Aveiro, Portugal. In a beaker, 10g of ground <63-µm sample was dispersed in water (about 800 mL). Flocculation of the particles was avoided by addition of 4 drops of 1% sodium hexametaphosphate solution (also used for kaolinite sample preparation in the Baseline Studies; Costanzo, 2001), and dispersion was aided by ultrasonication during the sedimentation set-up (Sonicator, Ultrasonic processor XL2020, Misonix incorp.; at 8 kHz (setting 4)) for a duration of 1 minute. The solutions were poured into tall 1-L cylinders, filled with water up to the 1000-mL mark, and stirred using a long stirring rod. The height of the dispersion subsequently siphoned off using a thin flexible plastic tube was in accordance to Stoke's Law, i.e. removal of 10 cm of the suspension after 8 hours, and 20 cm of the suspension after 16 hours (Fig. 3.2.1a).

Figure 3.2.1. **(a)** Sedimentation apparatus and set-up, showing removal of 10 cm of columns' suspensions into beakers to be oven-dried. **(b)** Sample SP taken directly from the filter press at Gresco & Grés, Lda. (Taveiro, Portugal; photograph by Daniela Baitan) **(c)** Map indicating the location of sample SP near Coimbra, Portugal, in the Taveiro Formation (slightly adapted from Rocha and Gomes, 2003, with permission from the author).

After each removal, water was added again until the 1000-mL mark, and the solutions were thoroughly stirred to start a new cycle. Throughout this process, care was taken not to agitate the cylinders after stirring as this would disturb the conformity of the suspensions' behaviour to Stoke's Law. The removed suspensions of <2-µm fractions were oven dried in beakers at 50 ºC. Dried clay cake remaining in the beaker was carefully scraped out, and ground to a fine powder using an agate mortar and pestle. The sample was now referred to as SP-fine.

The fine fraction of KGa-1b was collected at the University of Ottawa by sedimentation following the procedure by Tunney (1995). In a large beaker, 60 g of KGa-1b was dispersed in 4 litres of deionized water. While being stirred with a mechanical mixer, 0.1 M NaOH solution was added until the pH reached 9 (Fisher Scientific; Accumet basic pH meter; AB15), at which point stirring was stopped and the pH confirmed at un-agitated conditions. After 6 hours of undisturbed sedimentation, the top 15 cm of dispersion was siphoned off using a thin flexible plastic tube. This procedure was repeated several times in order to collect sufficient sample.

Through drop-wise addition of 0.1 M HCl solution until pH=6, the collected dispersion was flocculated and left to sediment. When the supernatant solution was clear, it was siphoned off and the remaining sediment alternately washed and centrifuged until no more Cl^- was present (confirmed with $AgNO_3$). The fine fraction of KGa-1b, hereafter referred to as K-fine, was then dried in a gravity convection oven at 60 ºC overnight.

A fraction of SP-fine and K-fine were kept aside for characterisation by XRD, NMR spectroscopy, FT-IR spectroscopy and TGA, and for later use in sorption experiments. The rest was divided for urea- and DMSO intercalation, to prepare precursors for modification with 3,6-dithia-1,8-octanediol (DTOD).

3.3. Experimental procedures

A general overview of the experimental procedure is given in Figure 3.3.1, with colour coding matching the spectra that will follow in this chapter. After the sedimentation procedures discussed in section 3.2 this section deals with the preparation of urea- and DMSO precursors, followed by melt-intercalation of the chelating agent DTOD.

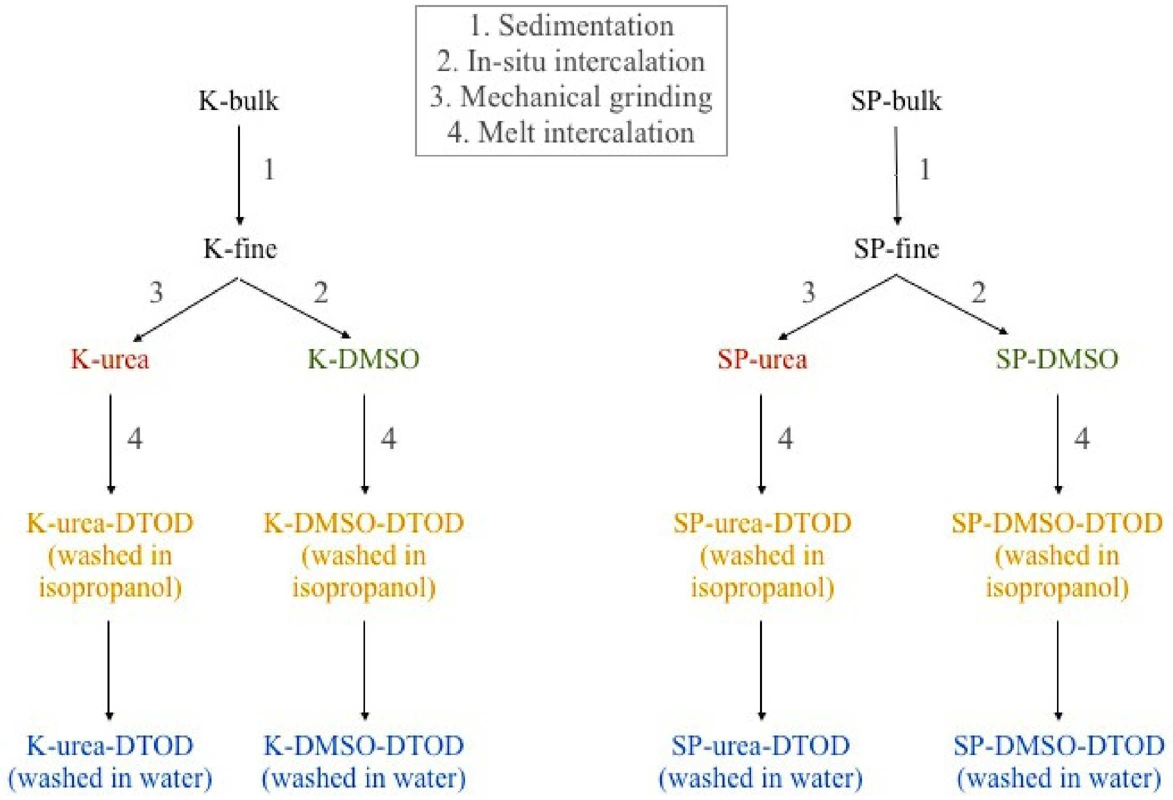

Figure 3.3.1. Schematic overview of experimental approach showing product evolution and processing steps. K refers to KGa-1b; SP refers of São Pedro, the Portuguese clay sample; bulk corresponds to the <63-µm fraction, fine is the purified clay by sedimentation corresponding approximately to the <2-µm fraction; fine fractions were modified with urea and DMSO (dimethyl sulfoxide), yielding 4 precursors that were each grafted with DTOD (3,6-dithia-1,8-octanediol). The same colour coding is used in the figures throughout this chapter.

3.3.1. Urea intercalation

The technique of urea intercalation into kaolinite minerals can be traced back to the ancient craftsmanship of Chinese porcelain that started probably around 500-600 A.D. (Weiss, 1963). At this time people were already aware that the pretreatment of kaolin (mixture of kaolinite, quartz and feldspar) by mixing it in a slurry of urine (containing urea), led to favourable ceramic properties (Weiss, 1963) now known to be from increased surface area and greater plasticity of the clay (Tsunematsu and Tateyama, 1999). Recent studies on urea-intercalated kaolinite have found enhanced properties for controlled release of fertilizers (e.g. Mahdavi *et al*., 2014; Sempeho *et al*., 2015), and paper coating (e.g. Shu et al., 2012; Zhu *et* *al*., 2014). For the purpose of this work, urea-intercalated kaolinite was performed in combination with dry milling to stimulate expansion of the interlayer and delamination of the mineral by causing fractures along the basal plane (Valášková *et al*., 2007), which allows access to a subsequent grafting compound through a replacement reaction.

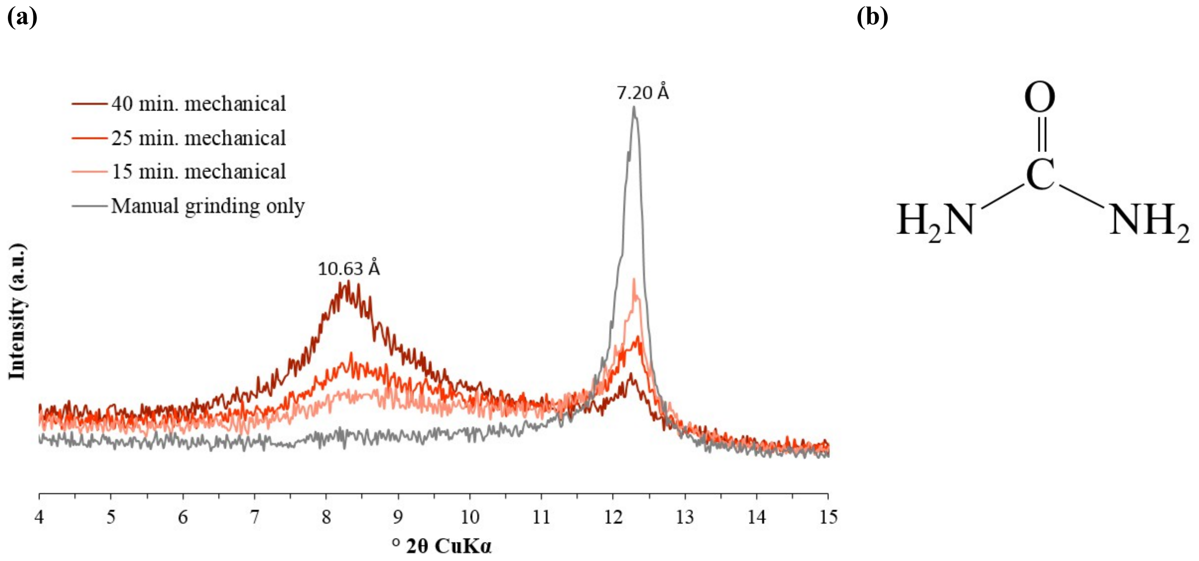

Figure 3.3.2. (a) The relative intensities of the XRD peaks corresponding to the d-spacings of natural kaolinite and urea-intercalated kaolinite after 2.5 hours of manual grinding followed by different intervals of mechanical grinding. The total time of mechanical grinding is indicated at each interval. These patterns follow the intercalation of urea between the layers of K-fine. Patterns after 10 and 35 minutes is omitted here for clarity. **(b)** Chemical structure of urea.

Aliquots of K-fine and SP-fine were intercalated with urea. For each sample, 8.0 g of urea was manually ground and homogenised with 5.0 g clay in a ceramic mortar and pestle for 2.5 hours, as per Letaief *et al*. (2006). Subsequent mechanical grinding was performed using a ceramic mill for several intervals of 5 or 10 minutes. It was found to be important to re-homogenise the mixture by hand in between these intervals, scraping off any of the urea-kaolinite powder stuck to the edge of the mill. The extent of intercalation was tracked by XRD analysis, and grinding was continued until the relative intensities of the natural- and urea-intercalated kaolinite peaks showed about 90% or more intercalation (see Fig. 3.3.2). The material was then washed in isopropanol, which rinses off residual urea but does not enter the interlayer space of kaolinite, until XRD analysis confirmed removal of remaining un-intercalated urea by absence of residual urea peaks (see Fig. 3.3.3). The resulting materials (K-urea and SP-urea) were characterised by XRD, NMR spectroscopy, FT-IR spectroscopy, and TGA.

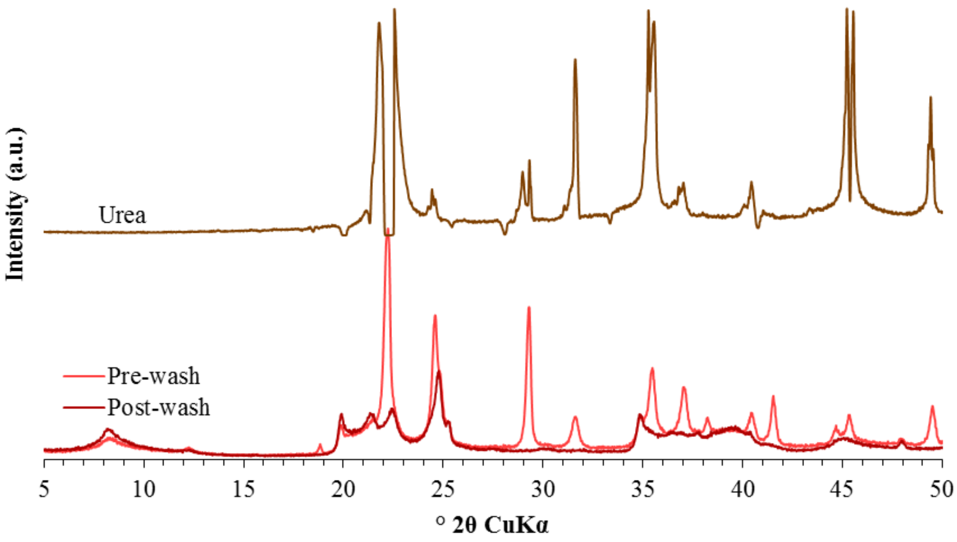

Figure 3.3.3. XRD patterns of K-urea before and after washing with isopropanol showing disappearance of peaks corresponding to residual urea. The pattern of the urea used is included.

3.3.2. DMSO intercalation

The intercalation of DMSO goes back to a study presented by Olejnik *et al*. (1968) who report on XRD and IR analyses of kaolinite samples intercalated with DMSO, a dipolar aprotic solvent (i.e. a proton acceptor only) meaning it can only form hydrogen bonds with the inner octahedral surface. The principle of DMSO intercalation is illustrated in Figure 3.3.4. In this study, aliquots of K-fine and SP-fine were intercalated with DMSO, by mixing 5.0 g of clay with 50.0 mL of DMSO and 2.0 mL of deionized water in a Florence flask (adapted from Letaief and Detellier, 2005). The reason for adding water is that it will break up the molecules in the pure liquid DMSO, thus increasing the amount of unbounded DMSO molecules that are free to react (Raussell-Colom and Serratosa, 1987). The mixtures were magnetically stirred under heat reflux (silicon oil bath) at 80ºC for 11 days. Finally the mixture was left to stir for 2 days at room temperature. In order to track intercalation success, several oriented slides were prepared during this process by pipetting a small amount of the suspension onto round glass slides that were oven-dried at 65ºC and could be analysed by XRD. When it was observed that the intercalation progress had stalled, or when the dispersion was becoming too viscous, more DMSO was added (in a range of 2 to 10 mL). When intercalation reached about 90% or more, as per the relative intensities of the natural- and DMSO-intercalated kaolinite peaks in XRD patterns, the material was finally recuperated by vacuum filtration of the mixture, oven-drying at 60 ºC, washing with isopropanol, oven-drying again, and gentle grinding of the DMSO-intercalated kaolinite samples (K-DMSO and SP-DMSO) in agate mortar and pestle. The products were then characterized by XRD, NMR spectroscopy, FT-IR spectroscopy and TGA.

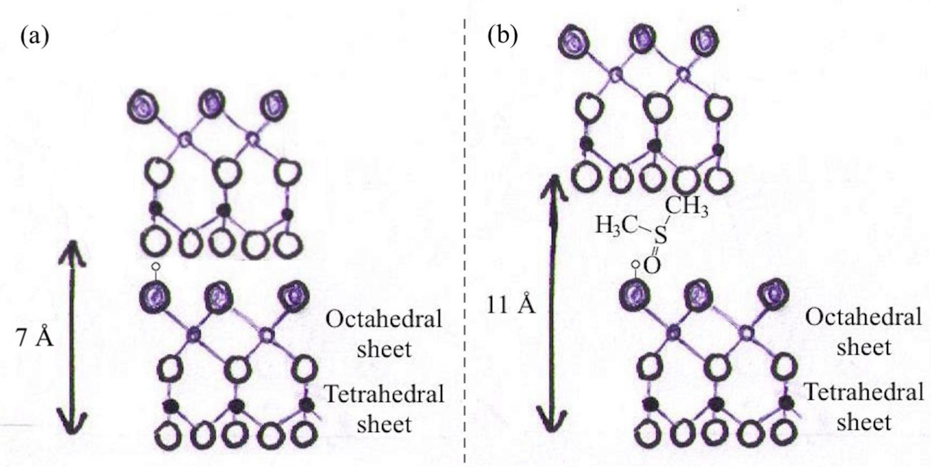

Figure 3.3.4. Schematic diagram illustrating the intercalation of DMSO **(b)** between the layers of a natural kaolinite mineral **(a)**. Only 1 of the hydrogen atoms of the OHs of the octahedral sheet is shown in both (a) and (b). For atom-key see Figure 1.1.1. (Adapted and redrawn from Letaief and Detellier, 2005 and Hayashi, 1995)

3.3.3. DTOD intercalation and grafting

2.0 g of each precursor (K-urea, SP-urea, K-DMSO, or SP-DMSO) was melt-intercalated with 8.0 g DTOD in a twin-neck round-bottom flask under N_2 at 180ºC. After about 20 hours the mixture was washed with isopropanol, centrifuged, oven-dried at 60ºC and gently ground to a fine powder with agate mortar and pestle for XRD and NMR analyses to confirm intercalation. If the compound was successfully intercalated, the basal spacing observed by XRD increased in accordance with the size occupied by the intercalated molecule (Fig. 3.3.5c), depending on its orientation in the interlayer region. The NMR spectrum exhibits peaks corresponding to those of the intercalated compound in isolation (Fig. 3.3.5a), though the exact chemical shift will probably change slightly because its incorporation between clay layers alters its magnetic environment, especially when it is covalently grafted.

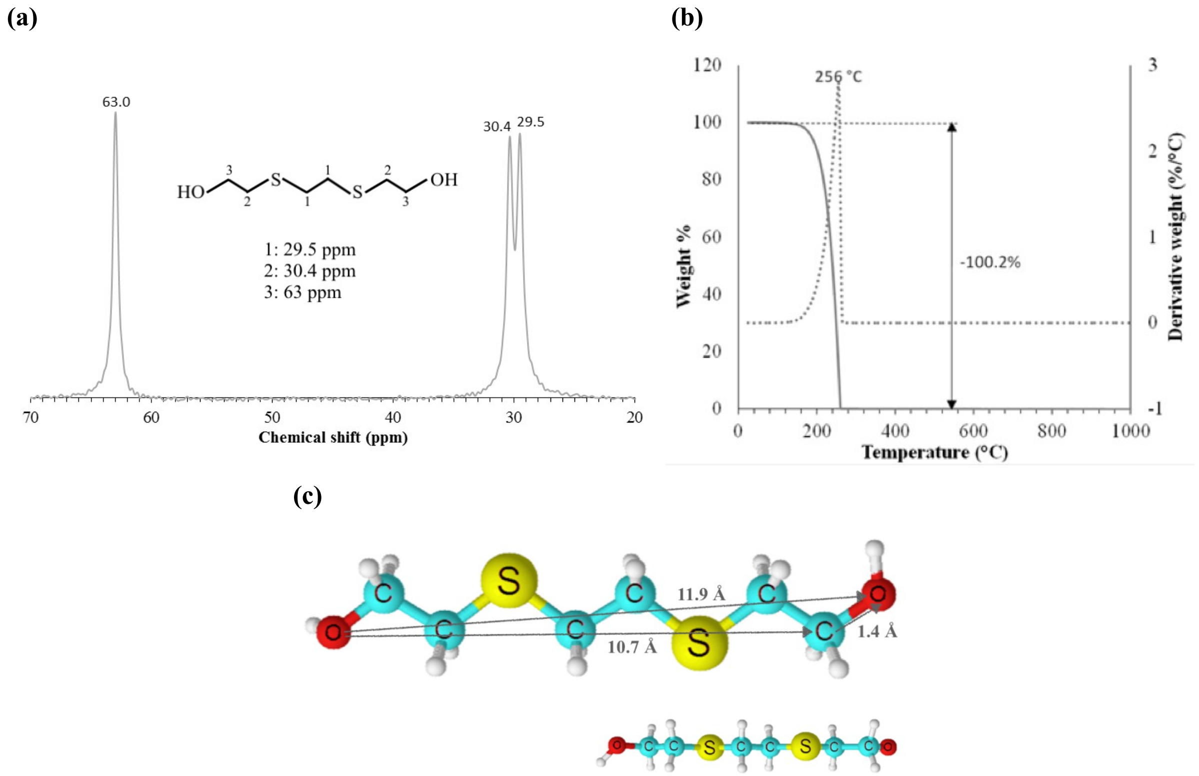

Figure 3.3.5. **(a)** Chemical shifts of DTOD (3,6-dithia-1,8-octanediol) observed by ^{13}C CPMAS NMR. **(b)** TGA and DTG (dotted line) of 3,6-dithia-1,8-octanediol in isolation. (**c**) Structure and interatomic distances in 3,6-dithia-1,8-octanediol estimated in ChemSketch.

The powder was subsequently washed in water for 24 hours to test for stability of the intercalated compound. This is necessary to test for it to be covalently grafted as well as for its subsequent application in metal sorption in aqueous solution. After the water-wash, the sample was again precipitated from solution by centrifugation, oven-dried at 60ºC and manually ground with agate mortar and pestle. Stability of DTOD was determined by a new round of NMR and XRD analysis. When no significant change was observed in the NMR and XRD patterns, grafting of the chelating compound DTOD was likely and the sample was then fully characterized by also performing TGA (pattern of isolated DTOD in Fig. 3.3.5b) and FT-IR. The sample names used are as outlined in Figure 3.3.1.

3.4. Results and discussion of KGa-1b characterisation and modification

3.4.1. Characterisation of the natural sample

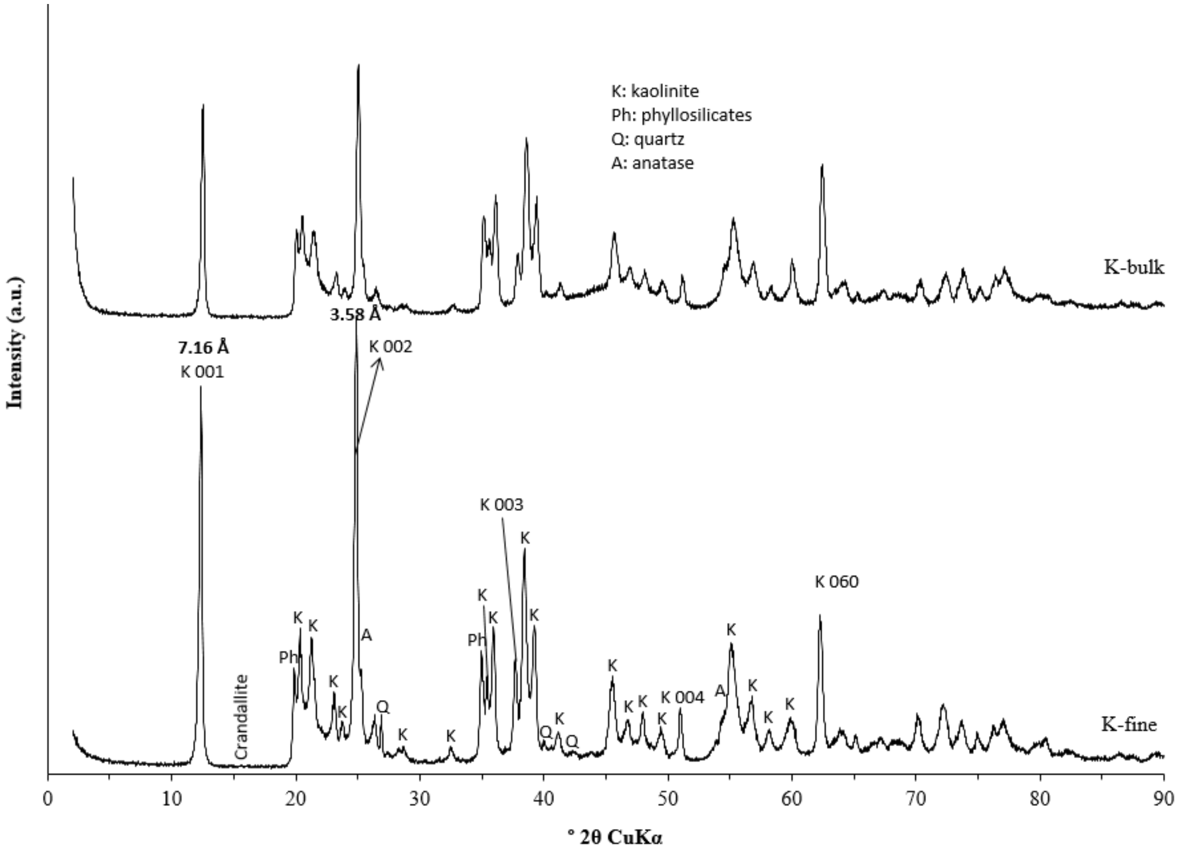

Figure 3.4.1. XRD patterns of the bulk fraction of KGa-1b (K-bulk) and the fine fraction collected by sedimentation (K-fine). Because peaks are mostly the same in K-bulk, labels have been included only once.

<u>XRD:</u> The XRD pattern of K-bulk shows a high degree of purity, demonstrated both by its low quartz content and its high resemblance to the purified fraction K-fine (Fig. 3.4.1). Pruett and Webb (1993) suggest this is because coarse sandstone (high permeability) covered the

deposit in Georgia, allowing a high water infiltration rate down to the location of KGa-1b, such that impurities were washed away. The sample was found to contain mostly kaolinite (d_{001} of 7.16Å), as well as some anatase, as indicated by the labelled peaks in the XRD patterns (Fig. 3.4.1). The peaks that occur around 4.47Å and 2.57Å are often used for semi-quantification of the phyllosilicate fraction in the <63-µm fraction and are therefore labelled as "Ph" even though they contain only kaolinite in this sample. A second peak occurs at 3.38 Å, between K*002* and Q*101*, that probably belongs to K*111* (Brindley and Robinson, 1946).

Semi-quantification according to the principles presented in chapter 2 yielded 96% kaolinite, 1-2% anatase, and 2% quartz. This is very similar to the semi-quantitative results reported by Chipera and Bish (2001) as part of extensive baseline studies of the samples in the Source Clays repository, who obtain 96% kaolinite, 3% anatase, and an impurity believed to be 1% crandallite. They, too, do not find significant differences between the XRD patterns of the bulk and fine-fraction of KGa-1b and present a pattern that is practically identical to the pattern shown here (Chipera and Bish, 2001). Pruett and Webb (1993), in their detailed study of KGa-1b, did not identify any crandallite. Its location in the XRD pattern is indicated here, but no measurable peak was found around this 2θ-angle (Fig. 3.4.1). Lecomte-Nana *et al.* (2013) also characterized KGa-1b and found anatase, quartz and no crandallite.

FT-IR: The FT-IR spectra of K-bulk and K-fine show no significant disparities in their absorption bands' positions, further indicating the high purity of the KGa-1b deposit in Georgia. It is possible to perform semi-quantification of kaolinite content based on the relative intensity of the band around 3700 cm^{-1} (here at 3688 cm^{-1}; Russell and Fraser, 1994). This suggests that the kaolinite content of K-bulk and K-fine has remained constant (Fig. 3.4.2).

Both spectra exhibit the fork-shape doublet that is characteristic of the OH-stretching region of kaolinite, with a peak at 3688 cm^{-1} attributed to in-phase (almost perpendicular to the *00l* plane) inner-surface OH stretching, two small peaks at 3668 and 3650 cm^{-1} of anti-phase (parallel to *00l* plane) inner-surface OH stretching, and another sharp peak at 3619 cm^{-1} of inner OH stretching (Ledoux and White, 1966; Valiculíková *et al.*, 2011; Madejová and Komadel, 2001).

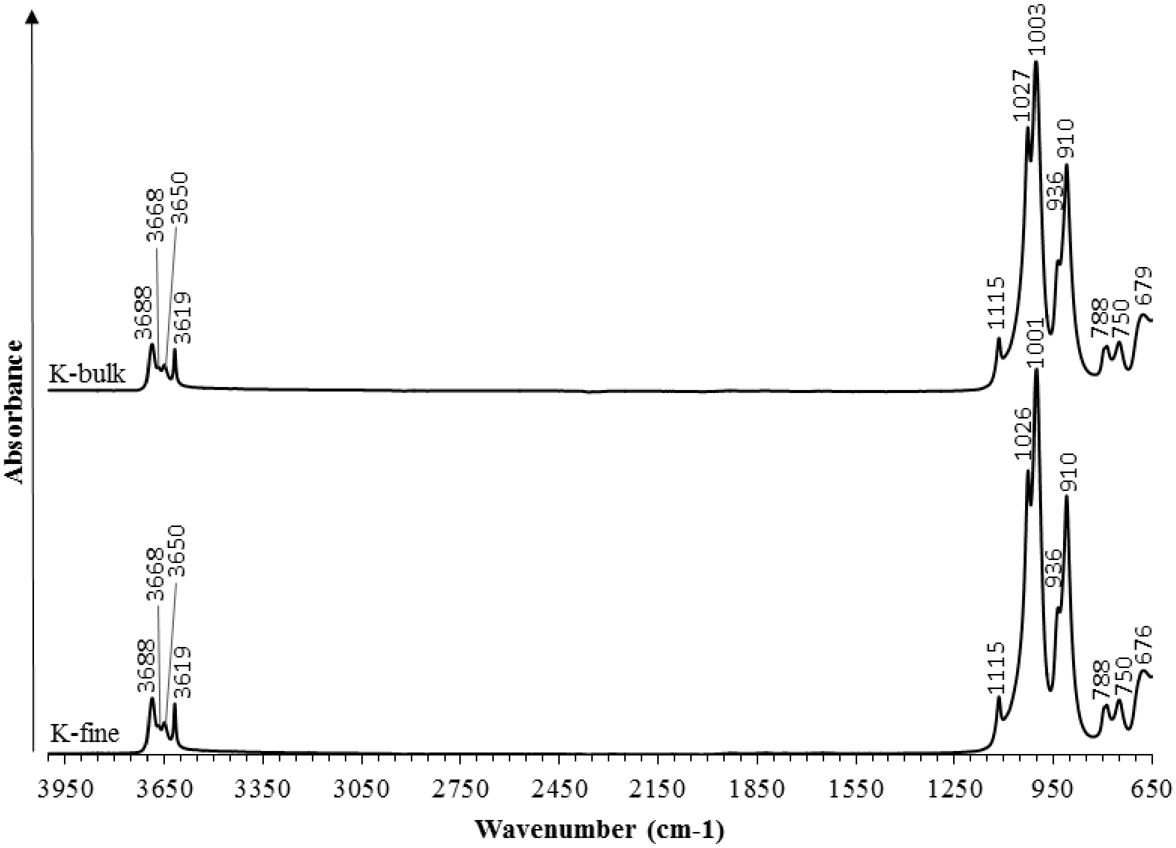

Figure 3.4.2. FT-IR spectrum of the bulk fraction (K-bulk) and fine fraction (K-fine) of KGa-1b.

The Si-O stretching region exhibits longitudinal Si-O stretching at 1115 cm^{-1}, in-plane Si-O stretching at 1026 cm^{-1} and 1001 cm^{-1} (Madejová and Komadel, 2001). The band at 936 cm^{-1} has been attributed to deformation of inner-surface OH groups, at 910 cm^{-1} to inner OH group deformation, and the bands at 788, 750 and 679 cm^{-1} to Si-O vibration (Madejová and Komadel, 2001; Saikia and Parthasarathy, 2010). In short, the sample exhibits bands that are well in accordance with the kaolinite minerals reported in the literature, and in particular corresponds to the absorbances by ATR crystal of KGa-1b reported by Madejová and Komadel (2001) as part of the Baseline studies.

Quartz seems to be almost absent since its characteristic doublet around 800 and 781 cm^{-1} is not observed (Russell and Fraser, 1994). Madejová and Komadel (2001) report that the absorption band at 788 cm^{-1} by ATR corresponds to 791 cm^{-1} of a KBr pellet, which is only attributed to quartz in fine-grained materials when it is unaccompanied by a second absorption towards 600 cm^{-1} (Wilson *et al.*, 1974).

NMR: The ^{29}Si CP-MAS NMR spectrum of the fine fraction of KGa-1b only displays one peak at -91.4 ppm (Fig. 3.4.3). The location of this peak is typical for kaolinite, with Q3 polymerisation and zero next-nearest neighbour Al in the tetrahedral sheet (Goodman and Chudek, 1994; Mägi *et al.*, 1984). However, it usually exhibits two peaks very close to each other, attributed to slight variations in Si-Al distances by interaction via interlayer hydrogen bonding (Thompson, 1985; Thompson and Barron, 1987). Thompson *et al.* (1992) also found two peaks for the ^{29}Si spectrum of KGa-1. In Becerro *et al.* (2009), however, the ^{29}Si spectrum of KGa-1b only exhibits one peak. This is probably due to an acquisition time that is too short, because doubling the acquisition time does yield a characteristic kaolinite doublet.

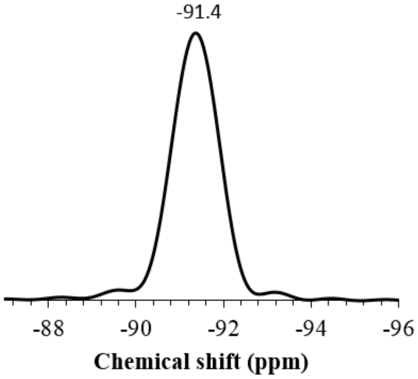

Figure 3.4.3. ^{29}Si CP-MAS NMR pattern of K-fine (1982 scans)

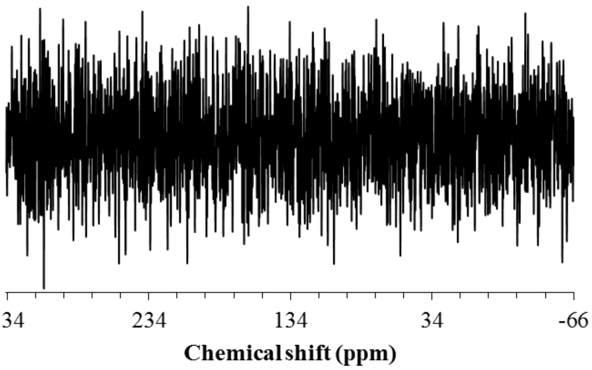

Fig. 3.4.4. ^{13}C CP-MAS NMR pattern of K-fine confirming no carbon was initially present (40960 scans).

The ^{13}C CP-MAS NMR spectrum shows that no significant amounts of organic matter were present in the starting material (Fig. 3.4.4).

TGA: The TGA pattern is also characteristic of kaolinite, with initial loss of small quantities of physisorbed water represented by a gently sloping and gradual decrease in mass prior to 300ºC, followed by one major endothermic mass-loss event observed around an inflection point at 514 ºC (for K-fine) due to dehydroxylation ($Al_2Si_2O_5(OH)_4 \rightarrow Al_2Si_2O_7 + 2H_2O$), yielding meta-kaolinite (Fig. 3.4.5; Mielenz *et al.*, 1953). Dehydroxylation corresponds to a loss of 14% of the initial sample weight, which is typical for kaolinite (Letaief and Detellier, 2011). Finally, just before 1000 ºC, kaolinite is known to undergo an exothermal crystallization into alumina and mullite that can only be seen by differential thermal analyses (DTA) (Watanabe *et al.*, 1987; Letaief and Detellier, 2011). No mass loss occurs before 500 ºC, indicating that no organic matter was present in the starting material. This was also supported by the absence of peaks in ^{13}C NMR (Fig. 3.4.4) and the FT-IR spectrum shown before where only mineralogical bands were identified (Fig. 3.4.2.).

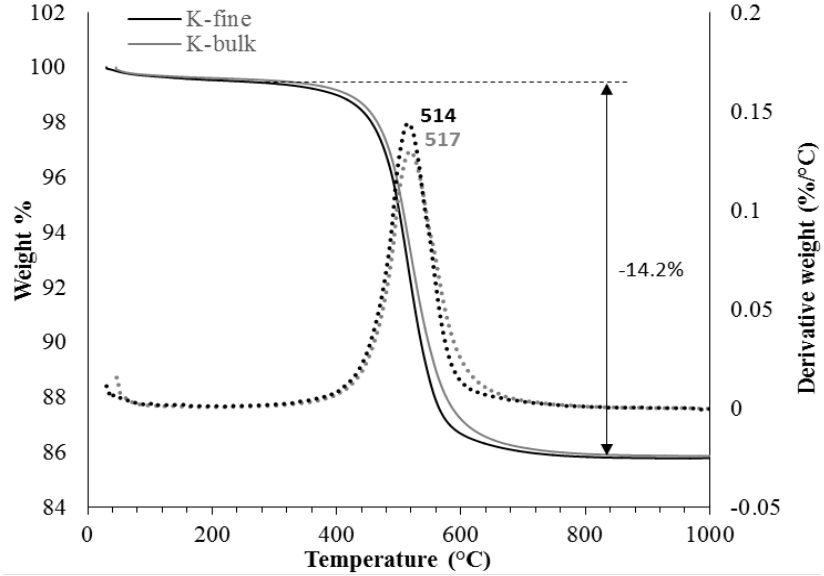

Figure 3.4.5. TGA pattern of the bulk- (K-bulk) and fine fraction (K-fine) of KGa-1b. Heated under nitrogen atmosphere.

3.4.2. Characterisation of K-DMSO precursor and its DTOD-grafted derivative

XRD: Since it is widely observed that the *hkl* reflections where *k*=3n (n is integer) experience fewer alterations than those peaks that do not fulfil this condition (Murray, 1988), the *060*-reflection is often used to verify the integrity of the mineral structure. The persistence of the *060*-reflections in the XRD pattern of the modified samples indicates that the mineral structure of kaolinite remained intact throughout the DTOD-intercalation and grafting processes (Fig. 3.4.6.), though the relative intensity and sharpness noticeably decreased after DMSO intercalation. The *001*-reflection of kaolinite shifted to 11.2 Å upon intercalation, which is in accordance with K-DMSO d-spacings reported by other authors (e.g. Frost *et al*., 1998; Letaief and Detellier, 2005; Mbaye *et al*., 2014). The DTOD-intercalated K-DMSO d-spacings increased somewhat to 11.7 Å after water washing was completed. This is sufficient space for DTOD to exist parallel or diagonally to the inner surface (see dimensions in Fig. 3.3.5). Washing in water does not significantly change the position of the *001*-reflection of the intercalated kaolinite, indicating that DTOD and kaolinite's inner surface probably covalently bonded (Tonlé *et al*., 2011).

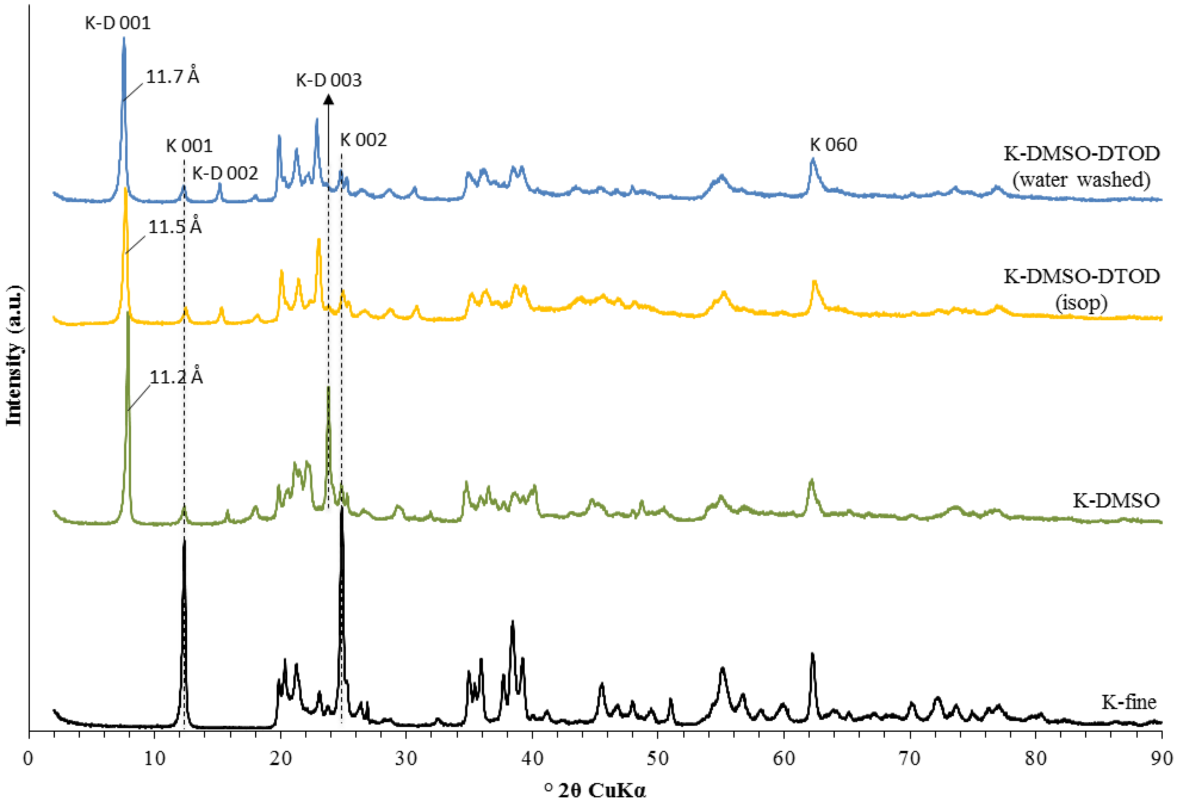

Figure 3.4.6. XRD patterns following the development of DTOD-intercalated K-DMSO precursor. K-fine included for more convenient comparison. K-D refers to DMSO-intercalated kaolinite.

NMR: ^{13}C CP-MAS NMR gives information about the environment of the organic molecule that is inserted between the clay layers. The pattern of K-DMSO exhibits the doublet at 43.1

and 44.1 ppm characteristic of DMSO-intercalated kaolinite (Fig. 3.4.7; e.g. Letaief and Detellier, 2005; Hayashi, 1995). Hayashi and Akiba (1994) and Thompson and Cuff (1985) both analysed how DMSO is positioned in a kaolinite interlayer space, reporting that the peak at 44.1 ppm is attributed to a methyl group keyed into the ditrigonal opening in the tetrahedral sheet (hexagonally shaped hole in tetrahedral sheet when imagining top view of Fig. 1.1.1), and that the peak at 43.1 ppm belongs to the methyl group parallel to the sheet (Fig. 3.3.4). The resonance at 40.8 ppm, however, indicates contamination most probably caused by excess DMSO deposited on the surface, meaning the sample was not sufficiently washed and/or dried. DMSO on its own has been reported to have a resonance peak around 40.0 ppm (AIST, n.d.) or 41.7 ppm (Hayashi and Akiba, 1994), which would match with this interpretation. Poor DMSO evaporation in lower-temperature ovens is not unusual (J. Fafard, 2015, pers. comm., 29 June) and did not seem to persist after intercalation with DTOD.

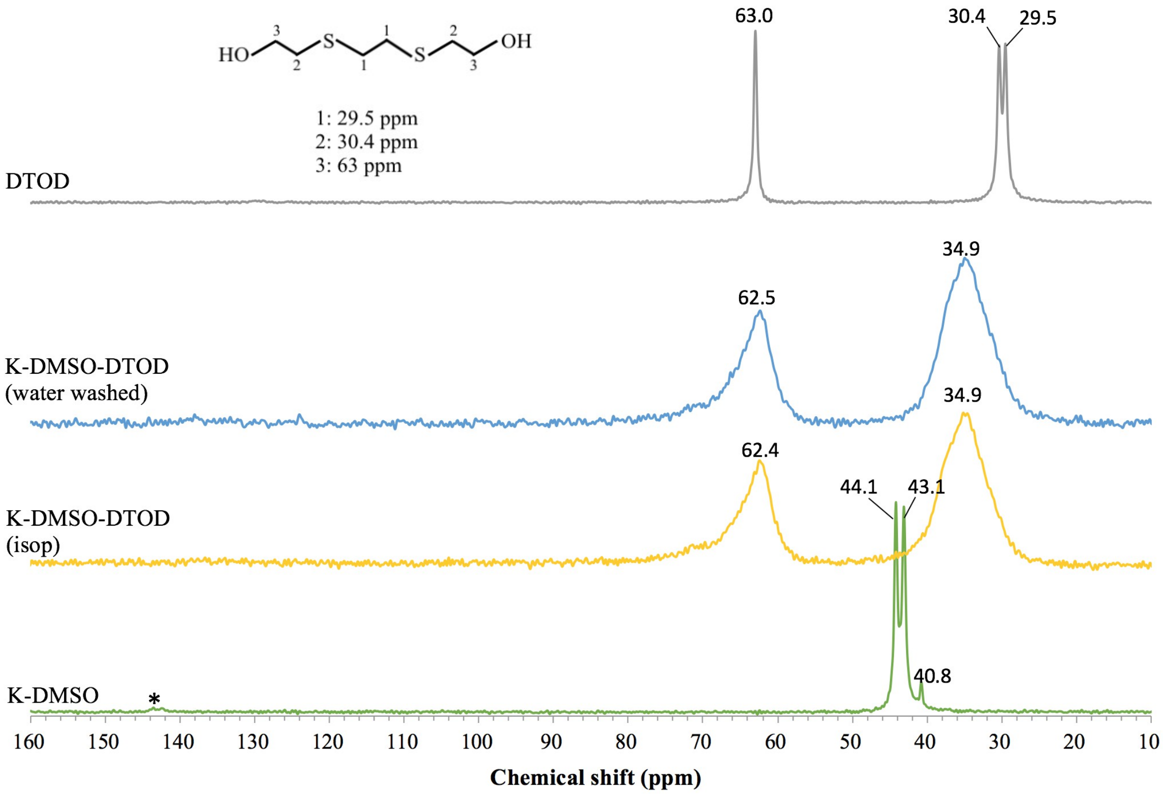

Figure 3.4.7. ^{13}C CP-MAS NMR spectra of K-DMSO precursor (3981 scans), the isopropanol (isop) washed (3512 scans) and subsequently water washed thio-kaolinite (4464 scans; line broadening = 5 Hz). Spectrum of DTOD (2700 scans) included for convenient comparison. * is spinning sideband.

After melt-intercalation of DTOD, the patterns of both the isopropanol- and water-washed sample exhibit peaks at 34.9 and around 62.5 ppm (Fig. 3.4.7). The peaks are broad and irregularly shaped, so they may contain several convoluted resonance bands suggestive of a heterogeneous sample. The persistence of the resonance peaks at practically identical positions before and after water washing indicates grafting of the DTOD compound (Detellier and Schoonheydt, 2014).

In comparison to the ^{13}C CP-MAS NMR spectrum of isolated DTOD, the C nucleus on the end of the DTOD chain experiences a smaller magnetic shift (63.0 to 62.5 ppm) than the peaks corresponding to the other two C nuclei (30.4 to 34.9 ppm). The grafted DTOD exhibits a smaller number of carbon sites than DTOD in isolation, suggesting it is grafted via two symmetrical sites: by both ends, or by both sulfur sites. Da Silva *et al*. (2015) reported a comparable silica-3,6-dithia-1,8-octanediol structure, where the alkyl chain connected to SiO-units by both ends. It is unlikely that the DTOD chain is connected by one end radiating diagonally into the interlayer space, because this would probably result in a greater number of resonance peaks. However, a small bump around 71 ppm occurs, meaning a minority of the alkyl chains might have bonded to the clay surface by only one end. This will become clearer when comparing to the interpretations of the following samples.

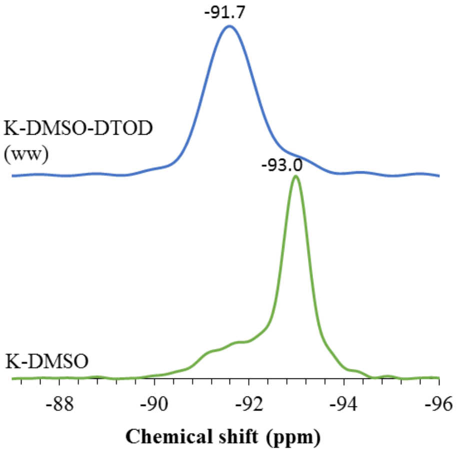

Figure 3.4.8. ^{29}Si CP-MAS NMR spectra of K-DMSO precursor and its DTOD-grafted derivative

Unfortunately it is difficult to tell the difference between aluminate (^{13}C-O-Al) and hydroxyl (^{13}C-O-H) substituents from a ^{13}C NMR spectrum, because their chemical shift positions are both around 60-63 ppm (Tunney and Detellier, 1994). The ^{29}Si CP-MAS NMR spectra of the DMSO precursor and the thio-modified kaolinite (Fig. 3.4.8) can give a better indication.

Both spectra exhibit one major peak, which is typically observed in intercalated kaolinite species (e.g. Matusik *et al*., 2013) because the increased d-spacing causes the interlayer interaction between Si and Al via hydrogen bonds to disappear (Thompson, 1985; Fig. 3.4.8). As aforementioned, this interaction is responsible for the doublet normally observed in the ^{29}Si NMR spectrum of natural kaolinite. The small peaks around -90 ppm in K-DMSO are attributed to remaining original kaolinite Si-sites (Hayashi and Akiba, 1994). When DTOD has been inserted, a small remaining bump of the main K-DMSO resonance peak remains. At this point original ^{29}Si peaks are not visible due to the overlapping of the -91.7-ppm peak. Close resemblance to the ^{29}Si NMR spectrum of K-fine is unsupportive of grafting on the Si-O sites.

FT-IR: The hydroxyl group of the octahedral has received wide attention in infrared studies. In a natural ordered kaolinite such as KGa-1b the orientation of the inner-surface hydroxyl groups is (almost) normal to the layer, and the inner hydroxyl group that forms the connection between the octahedral sheet and the tetrahedral sheet points towards the empty octahedral site (kaolinite is dioctahedral so only 2/3 of octahedral sites are occupied; Giese and Datta, 1973; Collins and Catlow, 1991).

The infrared spectrum of K-DMSO exhibits a markedly different OH-stretching pattern compared to the natural clay mineral (Fig. 3.4.9). All inner-surface hydroxyl bands occur at different wavenumbers, which makes sense with the DMSO-kaolinite association that occurs primarily via the hydroxyls (Fig. 3.3.4). The inner-hydroxyl stretching band at 3620 cm^{-1} persists, albeit at a lower relative intensity, indicating that the intrinsic layer structure of kaolinite, composed of a tetrahedral sheet connected to an octahedral sheet, is left intact (Tonlé *et al*., 2007). The newly appearing doublet at 3535 and 3501 cm^{-1} have been associated to the presence of water in K-DMSO, together with the broad absorption around – what would here be – 1658 cm^{-1} (Frost *et al*., 1998). These bands were earlier believed to correspond to hydrogen bonded methyl groups as an intermediate orientation of DMSO (Johnston *et al*., 1984). The peak at 3660 cm^{-1} is due to hydrogen bonding between the S=O group of DMSO with hydroxyls on the inner surface of the octahedral sheet (Horváth *et al*., 2010). The corresponding S=O stretching region is covered up by the intense Si-O stretching peak (Johnston *et al*., 1984).

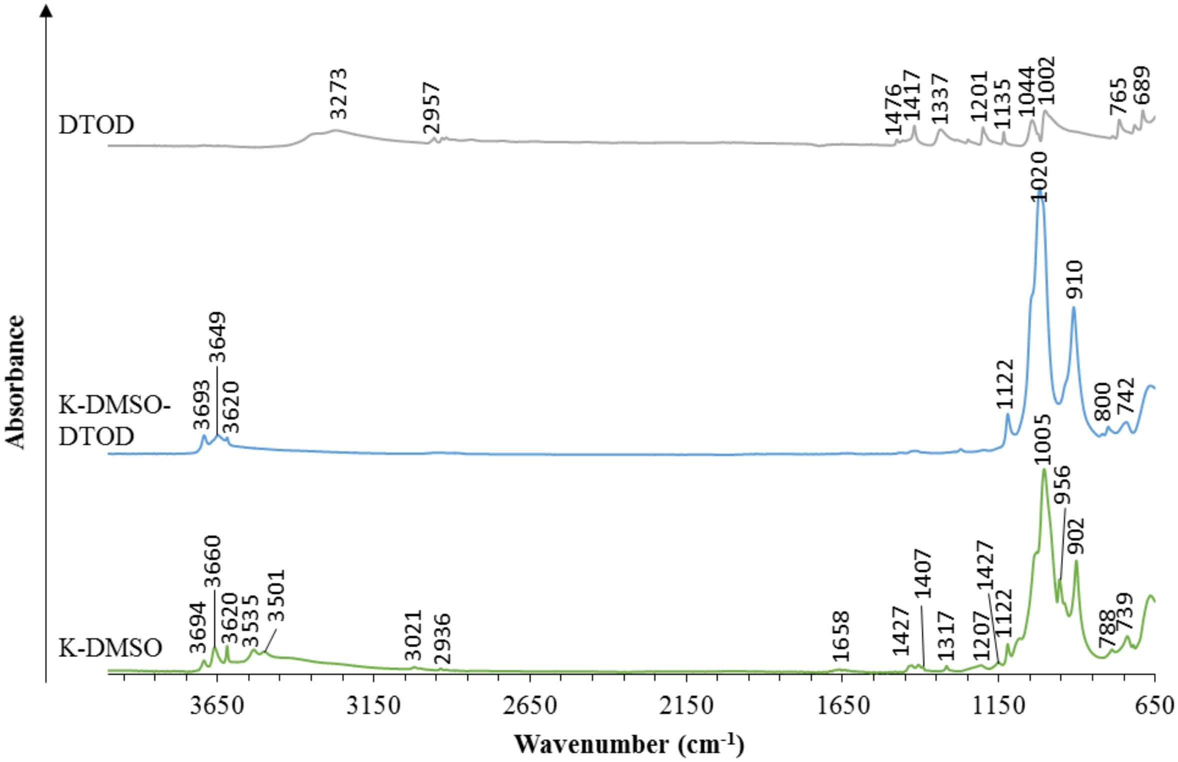

Figure 3.4.9. FT-IR spectra following the grafting of DTOD onto K-DMSO precursor.

The Si-O stretching region experienced fewer alterations, apart from the region between 900 and 1000 cm^{-1}, which corresponds to inner-surface OH deformations. The band occurring at 936 cm^{-1} in the natural sample (Figure 3.4.2), corresponding to Al-OH bending of the inner surface hydroxyl, decreases upon DMSO intercalation and is replaced by a new band at 956 cm^{-1}, further confirming the understanding that DMSO interacts with kaolinite via inner surface hydroxyls (Johnston *et al*., 1984). Moreover, the peak at 902 cm^{-1} is attributed to deformation of inner-surface hydroxyl groups hydrogen-bonded with DMSO's S=O (Horváth *et al*., 2010).

DMSO exhibits two identical methyl groups, one of which is keyed into the tetrahedral vacancy (Figure 3.3.4), as shown by its in-plane methyl deformation band that splits into two peaks at 1427 and 1407 cm^{-1} (Horváth *et al*., 2010). It has also been proposed that above 45 ºC DMSO exists in a second configuration where both of its methyl groups are liberated and they both rotate like a helicopter around its S=O base (Hayashi, 1997), quite like the initial interpretation by Johnston *et al*. (1984) on the peaks occurring at 3501 and 3535 cm^{-1}.

Observations of different S=O stretching bands (though largely hidden by Si-O stretching), as well as two water bending vibrations around 1610 and 1683 cm^{-1}, have led to the suggestion that DMSO might exist inside kaolinite not only in a hydrogen-bonded fashion with the octahedral sheet, but also linked by water molecules (Horváth *et al*., 2010). However, it is important to note that the exact nature of the DMSO-kaolinite interaction remains partly unresolved (Horváth *et al*., 2010).

In the DTOD modified sample, both Si-O and inner-surface OH vibrations have been affected. Expanded intercalated kaolinite will always exhibit a different OH stretching region because its interlayer hydrogen bonds have been broken, so it is not necessarily an element of proof for DTOD interaction with OH-groups (Ruiz Cruz and Franco Duro, 1999). A closer look reveals that the intensity of CH stretching vibrations are too low to be observed in DTOD-modified kaolinite (normally appearing in the 3000-2700-cm^{-1} region) and the band at 3649 cm^{-1} has returned almost to its original position in the natural sample of 3650 cm^{-1} (Fig. 3.4.2). The Al-OH vibration at 910 cm^{-1} is also like the natural sample and even exhibits a very weak shoulder around 936 cm^{-1}, suggesting an interaction between DTOD and the inner octahedral surface is weak. Compared to the natural sample, the Si-O stretching band has shifted from 1001 to 1020 cm^{-1}, and Si-O vibration bands at 788 and 750 cm^{-1} have moved to 800 and 742 cm^{-1} respectively. These observations could support bonding of DTOD to the siloxane sheet, which implies DTOD could potentially be grafted in smectitic clays too. However, the ^{29}Si NMR data presented before probably rule out this possibility.

TGA: The TGA of DMSO-intercalated KGa-1b exhibits two major peaks below 500 ºC, the first of which at 79 ºC represents, according to the contamination observations presented earlier, loss of surface-deposited DMSO (Fig. 3.4.10). Indeed, Hayashi (1995) reports that from two weight-loss events with inflection points around 57 and 157 ºC (here 79 and 167 ºC) when DMSO is heated, only the second peak remains when it is intercalated in kaolinite, except when the K-DMSO complex has not been completely dried (Hayashi, 1995). Hence, the TGA pattern of K-DMSO (Fig. 3.4.10) shows loss of intercalated DMSO at 167 ºC, which is an endothermic reaction (Letaief and Detellier, 2005), followed by dehydroxylation of kaolinite at a higher temperature than observed in the natural starting material (Fig. 3.4.5).

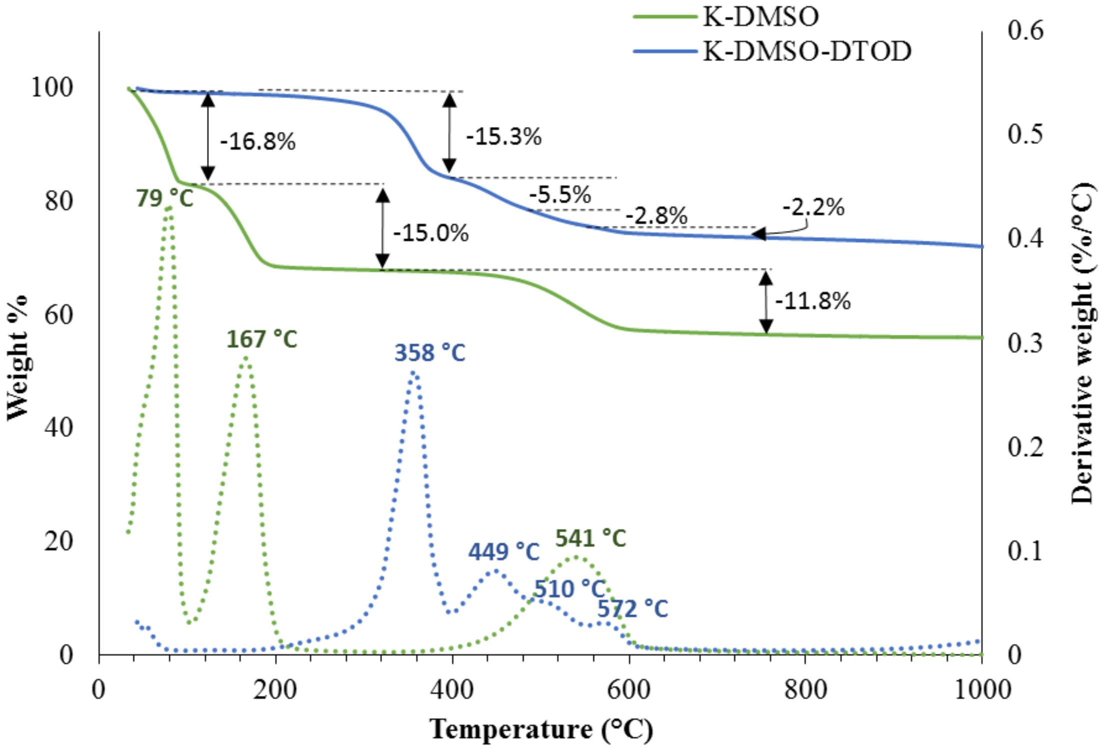

Figure 3.4.10. TGA patterns of K-DMSO and K-DMSO-DTOD (water washed). Heated under nitrogen atmosphere.

Excluding the loss of excess surface-deposited DMSO, both K-DMSO and the DTOD-intercalated derivative experience the same total % mass loss. The pattern of the thio-kaolinite sample K-DMSO-DTOD exhibits an increased heat resistance compared to the complete decomposition of DTOD in isolation at 256ºC (Fig. 3.3.5b). Apart from initial evaporation of physisorbed water, no mass loss occurs before 190 ºC, showing no more DMSO remains (Letaief and Detellier, 2011). The first mass-loss event is centred at 358 ºC, followed by several smaller events at inflection points of 449, 510 and 572 ºC. Such weight-loss peaks between 200 and 600 ºC are typical for grafted organo-clays (Tonlé *et al.*, 2011). dehydroxylation of kaolinite is affected compared to the natural sample (Fig. 3.4.5) as it is split into three smaller events, which is suggestive of modified clay surfaces, supporting the interpretation that DTOD has been grafted covalently, directly affecting the inner octahedral sheet (Letaief and Detellier, 2011). The peaks might correspond to those OH groups that were previously intercalated by DMSO, unaffected OH groups, and those affected by DTOD. Alternatively, the peak centred at 449 ºC could also be attributed to more strongly bound DTOD.

Assuming that the peaks before 500ºC correspond to loss of organic matter and those above 500 ºC correspond to kaolinite dehydroxylation, the loading of each organic moiety per unit of kaolinite ($Al_2Si_2O_5(OH)_4$) was calculated from the % mass loss in the TGA pattern. The % mass attributed to the organic compound was divided by the remaining % mass of the clay fraction, and subsequently each were converted by their known molar masses to yield a loading of 0.73 mole DMSO per mole of kaolinite and 0.40 mole of DTOD per mole of kaolinite. The former corresponds well to the value previously reported by Letaief and Detellier (2011) of 0.75 mole DMSO per kaolinite unit. If the peak at 449 ºC corresponds to a first dehydroxylation, K-DMSO-DTOD would consist of a loading of only 0.29 mole DTOD per kaolinite unit.

3.4.3. Characterisation of K-urea precursor and its DTOD-grafted derivative

<u>XRD:</u> The crystallinity of kaolinite is significantly reduced by the action of mechanical grinding, as was illustrated in Fig. 3.3.2, by the increasingly diminishing peak at 7.2 Å when the time of mechanical grinding was extended and a general dulling of peaks in the whole

pattern can be observed. Nevertheless the *060* reflection of kaolinite at 1.489 Å persists throughout all modifications, albeit at lower intensity once DTOD has been intercalated (Fig. 3.4.11). The d-spacing increases to 10.8 Å upon intercalation of kaolinite, corresponding to a layer increase of 3.6 Å. Numerous authors have reported such an increase in layer spacing from urea intercalation (e.g. Yan *et al.*, 2005; Zhenbang *et al.*, 2007; Tsunematsu and Tateyama, 1999; Mahdavi *et al.*, 2014).

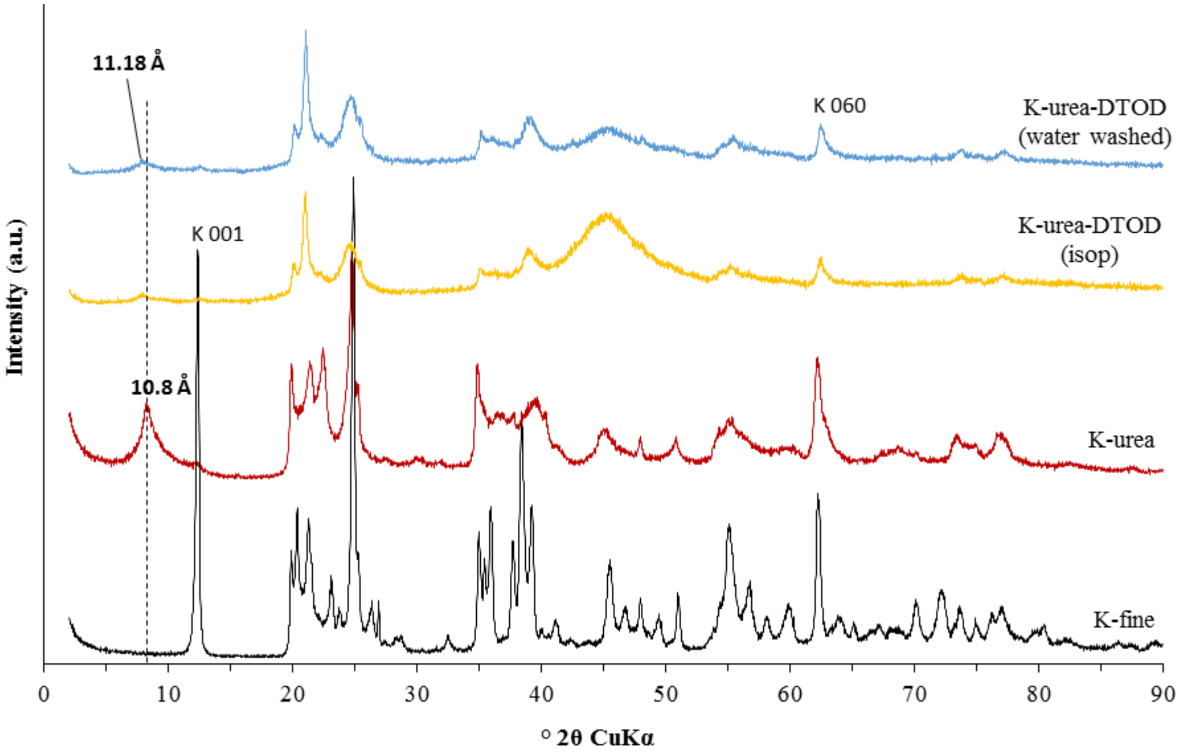

Figure 3.4.11. XRD patterns following the development of DTOD-grafted K-urea precursor. K-fine included for more convenient comparison.

The *001* reflection of DTOD-intercalated kaolinite almost diminished, suggesting that at least a significant portion of kaolinite exfoliated upon intercalation with DTOD (Frost *et al.*, 2001). The small peak that is visible at 11.18 Å corresponds to an interlayer space of roughly 4 Å, which could correspond to a monolayer-type arrangement of DTOD. Exfoliation is not uncommon in urea-intercalated kaolinite (Morsy *et al.*, 2014; Letaief *et al.*, 2011). The grinding action facilitates the intercalation of urea, because it weakens the hydrogen bonds holding the layers together, the particle size decreases and the specific surface area increases, (Valásková *et al.*, 2007). Grinding of kaolinite primarily leads to a decrease in the c-direction

(direction of the layer thickness), while the a- and b directions remain intact (Schrader *et al.*, 1970 cited in Suraj, 1997), as illustrated by a flattening of the d_{001} peak of kaolinite in its XRD pattern, while the *060* reflection remains (Fig. 3.4.11). However, grinding is not very precise or straightforward in terms of its effects on the structure of kaolinite. Several authors have noted agglomeration and a decrease in specific surface area when milling is continued for too long (e.g. Suraj *et al.*, 1997; Sánchez-Soto *et al.*, 2000). Gonzalez Garcia *et al.* (1991) demonstrated that both fragmentation of larger particles and aggregation of fine particles occur simultaneously. Depending on the crystallinity and the initial particle size of the starting material, the specific surface area decreases almost directly in a poorly crystalline sample that contained more than 80% <2-µm particles, while the more crystalline sample with 47% particles <2 µm experienced an increase in surface area for up to 36 hours of grinding (Gonzalez Garcia *et al.*, 1991).

NMR: The ^{13}C NMR spectrum of K-urea shows the characteristic resonance peak at 162.1 ppm from the one C atom present in urea (also reported by Letaief *et al.*, 2006; Letaief *et al.*, 2011), which is in agreement with urea on its own (Fig. 3.4.12). It is a challenging and time-consuming task to acquire a satisfactory ^{13}C NMR spectrum of urea. After application of the CP pulse, the ^{14}N nucleus of urea positioned between the protons and the central C atom decays very fast compared to the slowly decaying ^{1}H nucleus, such that the CP pulse does not get carried across effectively, resulting in a very long acquisition time (E. Ye, 2015, pers. comm., 12 August). In order to acquire a better spectrum than shown here, the experiment would need to be run at a higher magnetic field strength (Russell and Fraser, 1994; G. Facey, 2015, pers. comm. 24 June). This spectrum-acquisition challenge disappears when urea is intercalated in kaolinite, indicating the marked change in magnetic environment and therefore the seemingly strong association between urea and kaolinite.

A surprising resonance appears at 40.2 ppm, almost the same chemical shift as the aforementioned contamination in K-DMSO. Both precursor products were dried in the oven at the same time. Hence, as for K-DMSO, (poorly) evaporating DMSO probably deposited onto the surface of K-urea. The contamination disappears after intercalation with DTOD.

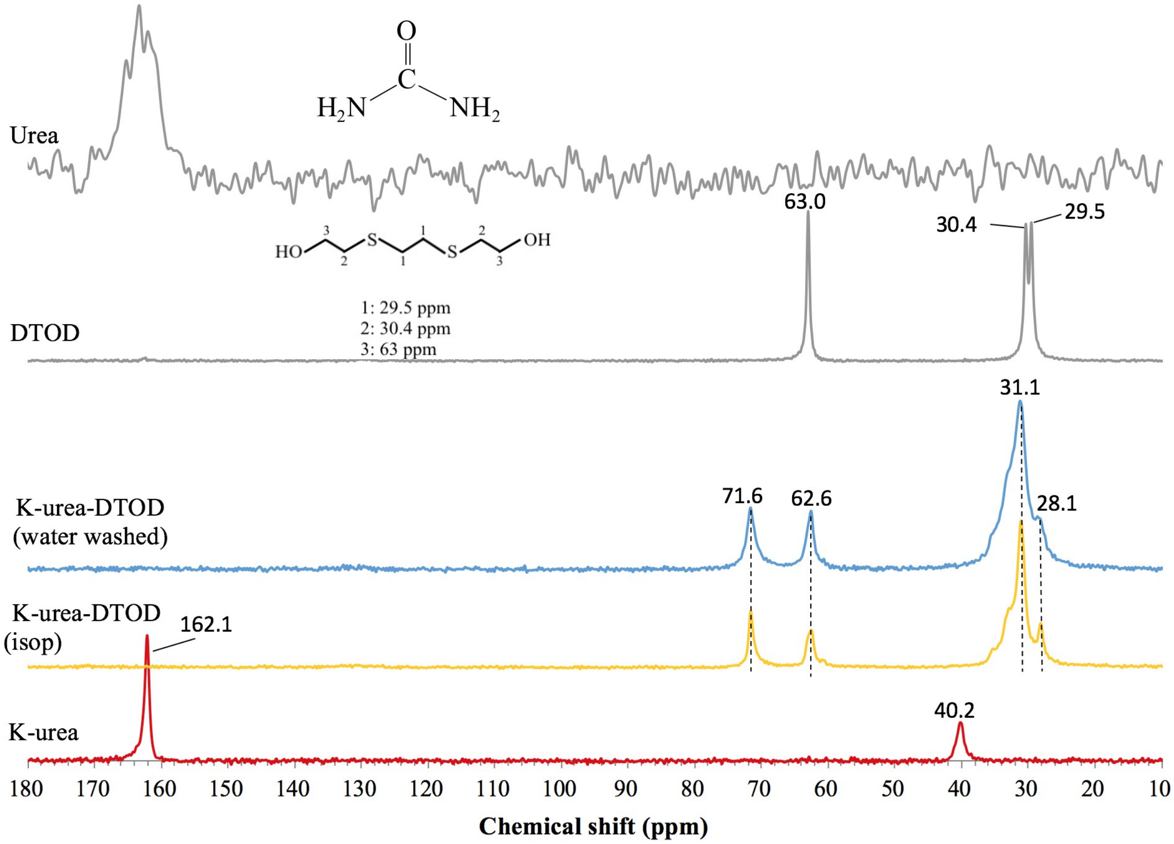

Figure 3.4.12. ^{13}C CPMAS NMR spectra following the development of DTOD- grafting onto K-urea (17381 scans), showing the product washed in isopropanol (isop; 1113 scans) and subsequently water-washed (1000 scans). Spectra of DTOD (2700 scans) and urea (112 scans; line broadening = 20 Hz) are included for reference.

A very different spectrum is observed compared to the DTOD intercalated K-DMSO precursor presented before, demonstrating the importance of the precursor for the final product. The C-3 peak of DTOD in isolation shifts and splits to two new chemical shifts at 71.6 and 62.6 ppm when inserted in K-urea, indicating two different environments are formed for the alkyl chain ends. This suggests that DTOD interacts with the inner surface of kaolinite by one of its ends only, the other end radiating into the interlayer space or environment surrounding an exfoliated clay surface face. DTOD bonding by one end radiating diagonally outwards, could occupy an interlayer space of about 4 Å as observed in the XRD pattern (See DTOD dimensions in Fig. 3.3.5c). This interpretation is in agreement with the small change in chemical shift observed in the remaining two peaks as well as the shoulders observed downfield from 31.1 ppm corresponding to all the new different magnetic environments created. Constant peak positions upon washing of the DTOD-intercalated sample with water is indicative of a successfully grafted product (Fig. 3.4.12). Though this may be the general position of the organic moiety, it should be noted that the complex and inhomogeneous nature of K-urea is probably responsible for some minor variations in DTOD-kaolinite associations.

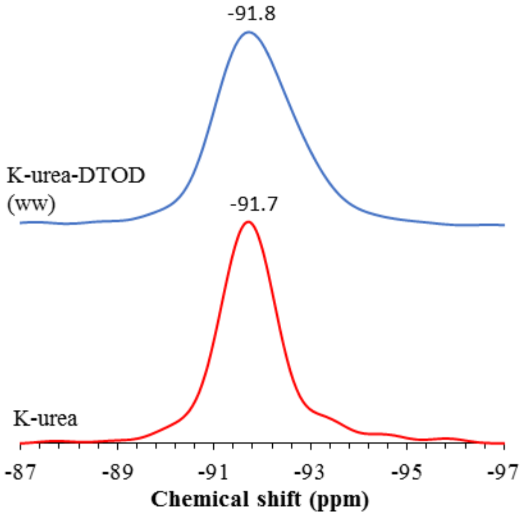

Figure 3.4.13. ^{29}Si CP-MAS NMR of K-urea and K-urea-DTOD (water-washed)

The ^{29}Si CP-MAS NMR of the urea-intercalated kaolinite exhibits one resonance at -91.7 ppm, also reported by Letaief *et al*. (2006), which is a subtle shift from -91.4 ppm in the natural kaolinite sample (Fig. 3.4.13). Subsequent grafting with DTOD leads to a smoother and somewhat broader peak at -91.8 ppm.

<u>FT-IR:</u> Analysis by FT-IR of the urea-kaolinite product is not straightforward because faults, location and extent of delamination depends on the kaolinite sample and exact intercalation conditions. As a result, values and interpretations in the literature are quite variable as well. FT-IR spectra of the urea-intercalated KGa-1b presented here (Fig. 3.4.14) display a modified inner-surface hydroxyl space with a new peak at 3697 cm^{-1} that belongs to symmetric NH-group vibration of urea interacting with the inner tetrahedral sheet (Horváth *et al*., 2010), as well as a new appearance at 3501 cm^{-1} that is associated with a hydrogen

bond between NH_2 and tetrahedral inner-surface oxygens (Ledoux and White, 1966; Mahdavi *et al*., 2014). A broad flat band around 3410 cm^{-1} is also due to urea and corresponds to the occurrence of asymmetric and symmetric NH_2 vibrations interacting with oxygen on the inner tetrahedral sheet (Frost *et al*, 1997), hence the shift compared to isolated urea. The band at 3620 cm^{-1} remains unchanged because it corresponds to internal hydroxyl groups.

In a next region of the spectrum (Fig. 3.4.14), the triplet around 1650 cm^{-1} most likely corresponds to NH_2 bending, coupled to CO stretching at 1672 cm^{-1}, and CN stretching is absorbed at 1473 cm^{-1} (Ledoux and White, 1966). According to Sempeho *et al*. (2015) the peak at 1591 cm^{-1} is due to a HNC+CN stretch. In the Si-O region most peaks have remained the same but flattened, apart from a shift in the doublet at 780 and 745 cm^{-1}, attributed to Si-O stretching. Urea in isolation exhibits a band at 1670 cm^{-1} attributed to C=O stretching, which is also observed in K-urea (Letaief *et al*., 2006).

The Si-O stretching region looks broadened and convoluted, with the only noticeable peak shift for the Si-O vibrations at 780 and 745 cm^{-1} (788 and 750 cm^{-1} in the natural sample). These observations suggest possible interactions with both the tetrahedral sheet via Si-O group and via the hydroxyls on the octahedral sheet.

Urea can be considered as a protic molecule (i.e. simultaneously a proton donor and acceptor), so that it could form hydrogen bonds with the inner surface of both sheets (Olejnik *et al*., 1968). Indeed, the interaction between kaolinite's inner surface and intercalated urea is traditionally believed to be by hydrogen bonding with both the hydroxyl surface of the octahedral sheet and the oxygen surface of the tetrahedral sheet (Weiss, 1961; Ledoux and White, 1966). Here, mostly changes related to interactions with the tetrahedral sheet are observed, supporting the suggestion that urea interacts by hydrogen bonding between its NH-group and the inner tetrahedral sheet (Horváth *et al*. (2010). A subsequent forced hydrogen bonding between C=O and octahedral hydroxyls has also been proposed (Horváth *et al*., 2010) which could explain some of the variations observed in the hydrogen stretching region despite a pretty constant Al-OH surface deformation at 936 cm^{-1}.

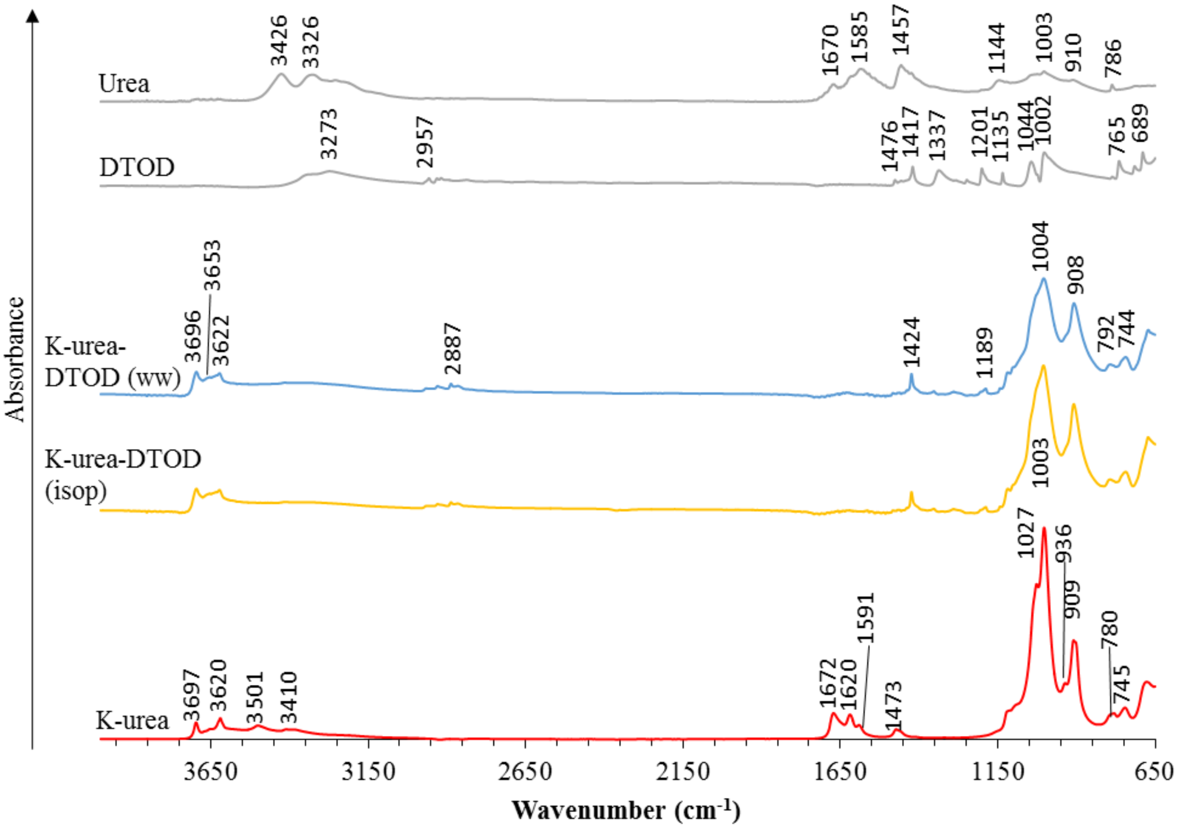

Figure 3.4.14. FT-IR spectra following the development of DTOD-grafted K-urea precursor. The isopropanol-washed and water washed K-urea-DTOD samples have absorption peaks at the same wavenumbers. Spectra of DTOD and urea are included for comparison.

Many K-urea bands disappear upon intercalation with DTOD, including the C=O stretch around 1670 cm^{-1}, further supporting that urea was completely removed (as observed earlier in the NMR spectra). The regions from 1520 to 1400 and 3000-2800 cm^{-1} are attributed to methylene vibrational modes (Vaia *et al*., 1994). Easily differentiated peaks at 1417 and around 2957 cm^{-1} in pure DTOD seem to shift in the thio-kaolinite samples to 1424 and 2887 cm^{-1} respectively, indicative of a bonding effect on the methyl ends. Also, some organic material may be deposited on the surface, which would explain why some particles in this sample were strongly aggregated crumbs that could not be ground to fine powder (Appendix C.2).

Compared to the inner-surface OH-stretching bands of natural kaolinite, K-urea-DTOD exhibits only one blunt band at 3653 cm^{-1} instead of the doublet in K-fine, and the band of inner-surface hydroxyl stretching has shifted from 3688 to 3696 cm^{-1}. Even the inner hydroxyl band has moved slightly by two wavenumbers to 3622 cm^{-1}, but this may just be a result of the peak broadening and flattening.

Some peaks in the Si-O region have also shifted compared to the natural sample, including those at 792 and 744 cm^{-1} (788 and 750 cm^{-1} in the natural sample). However, a more pronounced effect on the hydroxyl peaks suggests this is where bonding with DTOD occurs.

TGA: TGA patterns show that upon heating the kaolinite-urea intercalate, it loses physisorbed water on its external surface when it undergoes a first weight loss at an inflection point of 44 ºC, followed by decomposition of intercalated urea at 207 ºC, and finally the dehydroxylation of kaolinite at 487 ºC (Letaief *et al.*, 2006; Fig. 3.4.15). Evolved gas analysis of TGA coupled to FT-IR and mass spectroscopy by Cheng *et al.* (2014) also supports this, as they determined that ammonia, water, cyanic acid and carbon dioxide were released until a temperature of 450 ºC, followed by the production of only water and carbon dioxide at 500 ºC. The intercalated kaolinite samples exhibit a dehydroxylation temperature that is 27 and 44 ºC lower than the natural sample, a sign of decreased particle size and lower crystallinity (Cases *et al.*, 1982 cited in Sei *et al.*, 2006) – unsurprising for urea-milled clay. A temperature shift of 30-90 ºC is often observed in organically modified kaolinites (Langier-Kuźniarowa, 2002). As for the loss of the organic moiety DTOD, this occurs at an inflection point of 328 ºC, corresponding to a moderately weak grafting (Mercier and Detellier, 1995). This means that the less strongly grafted configuration by one DTOD chain extremity that has been suggested above is supported by TGA. A preliminary bump at 272 ºC supports the presence of a surface DTOD population, which would be more weakly bound yet decomposes at a higher temperature than DTOD in isolation (256 ºC; Fig. 3.3.5b).

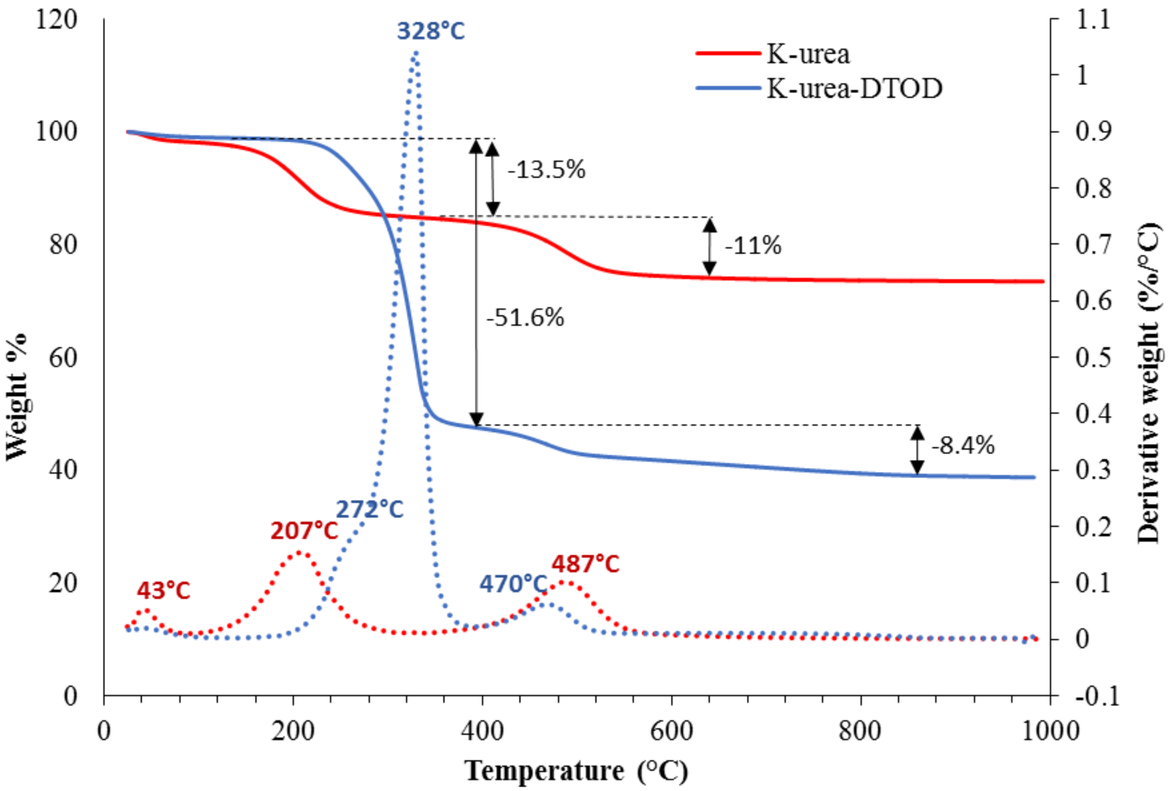

Figure 3.4.15. TGA pattern of K-urea precursor and its DTOD-grafted derivative K-urea-DTOD. Heated under nitrogen atmosphere.

A loss of more than 50% by weight of organic material is observed in the thio-kaolinite, indicating a very high loading with the organic moiety. Indeed, this sample contained some very sticky particles corresponding to excess organic matter that could not be washed off. The amount of each organic moiety per unit of kaolinite was calculated again, assuming the peaks at 470 and 487 ºC to be attributed to kaolinite dehydroxylation, and excluding the peak at 43 ºC corresponding to loss of sorbed water, giving an estimated loading of 0.69 mole of urea per unit of kaolinite in K-urea and a remarkable 1.51 mole of DTOD per kaolinite unit in K-urea-DTOD. Probably the loss at 272 ºC is unintercalated DTOD, interacting with the exposed external kaolinite surfaces. This would leave roughly 1 mole of DTOD per unit of kaolinite to be inserted between layers.

3.5. Results and discussion of SP characterisation and modification

3.5.1. Characterisation of the natural sample

XRD: The XRD patterns of sample SP reveal a more complex sample with a greater number of accessory mineral phases as well as the presence of more than one clay mineral (Fig. 3.5.1.). Peak identifications are given in figure 3.5.1. Sedimentation yields a purer fine fraction displaying relatively less intense quartz peaks. Presence of kaolinite was confirmed by heating an oriented slide to 500 ºC to differentiate from chlorite, leading to disappearance of the kaolinite peak but persistence of illite. TGA, presented shortly, also confirmed a major mass loss event at 502ºC (Fig. 3.5.5).

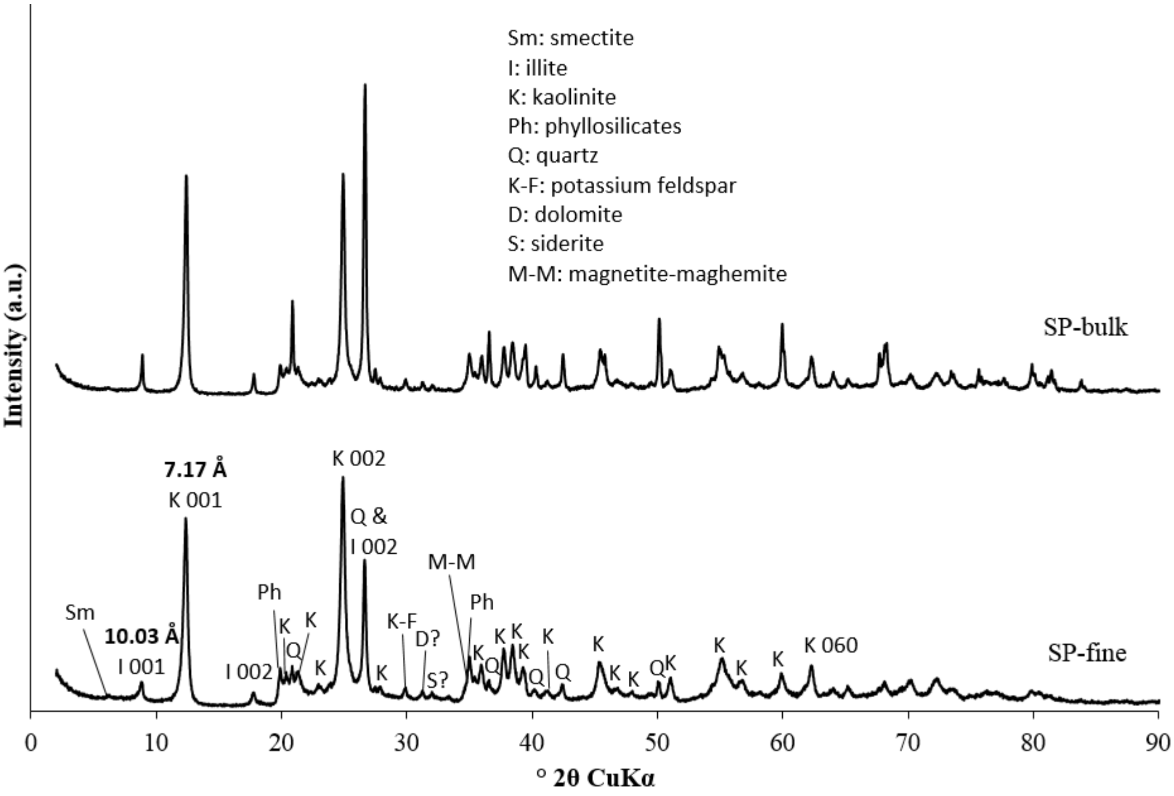

Figure 3.5.1. XRD patterns of the bulk fraction of São Pedro (SP-bulk) and the fine fraction collected by sedimentation (SP-fine).

Both dolomite and siderite have been identified as impurities, because no matching kaolinite reflections could be found at these d-spacings: 2.86 Å and 2.79 Å. Magnetite-maghemite is commonly found in clays coming from Taveiro (Rocha and Gomes, 2003), the likely presence of which has been indicated. Maghemite can form from the oxidation of iron carbonate minerals like siderite (Ellwood *et al*., 1989). Many accessory minerals have reflections that overlap those of kaolinite, so it is possible that small quantities of impurities remain undetected. Some of the small reflections just next to the main K*002* and Q*101* peaks likely contain feldspar (Brindley and Brown, 1980). Feldspar is an igneous rock formation, like quartz, and a slowly weathered mineral that occurs in small amounts in the clay-size fraction of soils (Brady and Weil, 2002). Together with other colloidal silicates (e.g. quartz and micas), they represent a dominant portion of many soils and are a major source of relatively unavailable (due to slow weathering) potassium for plants (Brady and Weil, 2002). It is therefore not surprising to find remaining feldspar and quartz phases.

Table 3.5.1. Semi-quantification (mass %) of mineralogical composition of the <2-μm fraction of sample SP, based on peak analyses by MacDiff (version 4.2.5; Petschick, 2001). Peak identifications according to Brindley and Brown (1980). Semi-quantification of phyllosilicate minerals was based on the oriented slides.

Mineral phase	D-spacing (Å)	Mass %
Phyllosilicates	4.47	85
Illite/mica	*10.22*	*12*
Kaolinite	*7.26*	*73*
Smectite	*14.75*	*<1*
Quartz	3.35	10
K-feldspar	2.99	1-2
Dolomite	2.86	2
Siderite	2.79	1-2

Semi-quantification of the <2-μm fraction of SP gave a kaolinite content of 73% (Table 3.5.1), mostly due to a greater amount of quartz in this sample. It should be noted though that 10% quartz is probably an upper boundary because its peak at 3.35 Å overlaps with that of I*003*. Since the Taveiro clay formation reportedly contains illite (Rocha and Gomes, 2003), the reflection around 10 Å is referred to as such in this report. However, identification of the oxidation state of iron in the mineral would be required to differentiate illite from other micas, which is not possible from the XRF results presented here (Bain and Smith, 1994).

XRF: Compared to KGa-1b (Appendix B) SP contains a greater fraction of SiO_2, which may be attributed to the presence of illite which has a 2:1 layer structure and therefore possesses twice as much SiO_2 per unit cell (Fig. 3.5.2). The presence of siderite (iron carbonate) was already suggested by XRD and would agree well with the iron content by XRF, as well as the small bump observed in TGA at 292 ºC that could originate from carbonate (presented shortly). XRF further indicates that the presence of potassium feldspar and anatase (TiO_2) are likely. Magnesium could be attributed to the smectite and/or illite phases as well as Mg-substituted siderite (Dubrawskit *et al*., 1989).

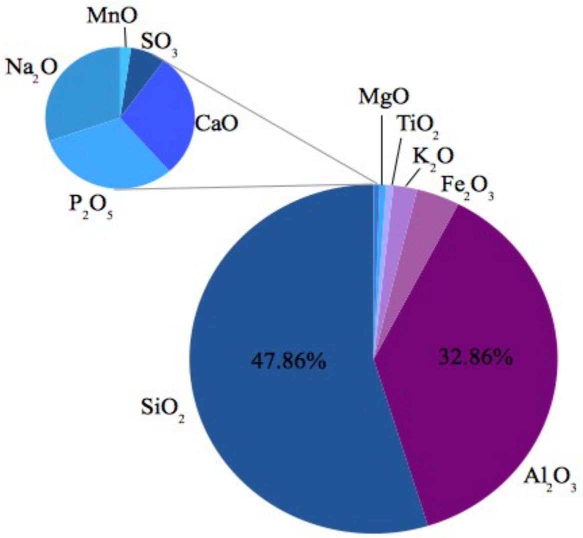

Figure 3.5.2. Quantitative XRF results of percentage oxide composition of the fine fraction of São Pedro. The whole circle represents a total of 87.5%.

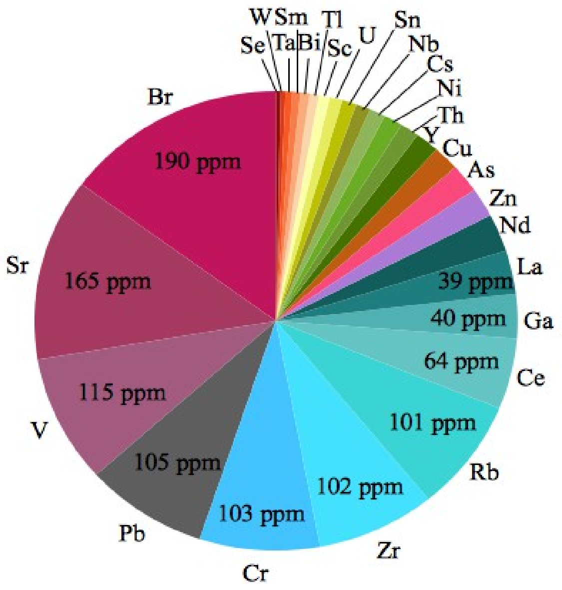

Figure 3.5.3. Quantitative XRF results of trace elements present in the fine fraction of São Pedro. The whole circle represents a total of 1281 ppm.

Trace metal analysis revealed a significant presence of lead, smaller concentrations of copper, arsenic and zinc, and an even smaller amount of nickel (Fig. 3.5.3) which should be taken into account in the sorption studies (chapter 4). No cadmium was detected.

FT-IR: The FT-IR spectra of SP-bulk and SP-fine display the OH-stretching region with the characteristic fork-shape of kaolinite surrounding 3650 cm^{-1}, as well as the Si-O stretching region from about 1150 to 650 cm^{-1} (Fig. 3.5.4). Though in slightly different positions, interpretation of the absorption bands is in conformity to the previously discussed KGa-1b natural sample: the first peak at 3691 cm^{-1} corresponds to in-plane inner surface OH stretching, the two smaller peaks following at 3666 and 3653 cm^{-1} are from anti-phase OH stretching, and the next spike of the fork at 3619 cm^{-1} is caused by internal OH stretching (Russell and Fraser, 1994; Madejová and Komadel, 2001; Valiculíková *et al.*, 2011).

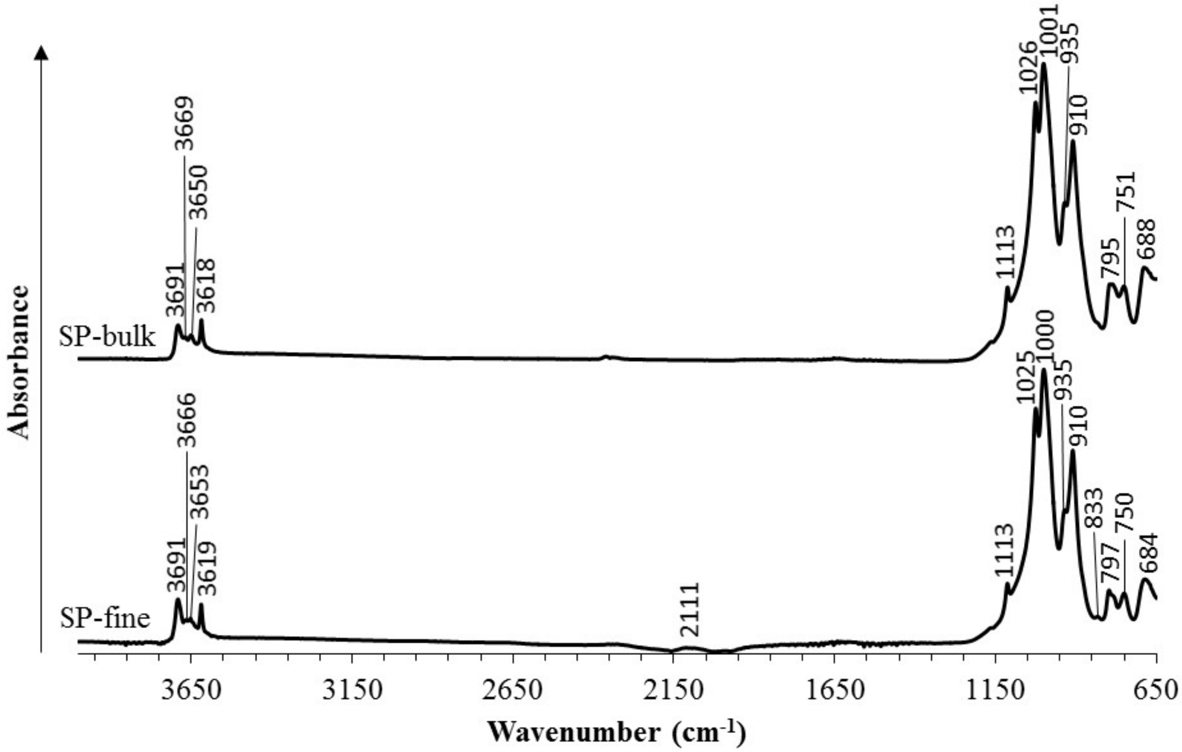

Figure 3.5.4. FTIR spectrum of the bulk fraction (SP-bulk) and fine fraction (SP-fine) of sample São Pedro.

Longitudinal Si-O stretching occurs at 1113 cm^{-1}, in-plane Si-O stretching at 1025 cm^{-1} and 1000 cm^{-1}, and deformation of the inner-surface- and inner hydroxyl groups are observed at 935 and 910 cm^{-1} respectively (Madejová and Komadel, 2001). The band at 797 cm^{-1} (Si-O) differs the most from the previously discussed KGa-1b, which is probably due to a higher quartz content which typically displays a characteristic doublet in this area (theoretical bands at 1085, 800 and 781 cm^{-1}; Russell and Fraser, 1994). The last bands at 750 and 684 cm^{-1} are from Si-O perpendicular vibration (Madejová and Komadel, 2001). A relatively more intense peak at 3691 cm^{-1} indicates a higher kaolinite content in SP-fine, as this peak can be used for semi-quantification (Russell and Fraser, 1994).

Other accessory minerals identified in XRD that potentially contribute minimally to the pattern are feldspars (Ca-plagioclase at 920 cm^{-1}) and goethite (893 and 794 cm^{-1}; Russell and Fraser, 1994). Dolomite absorbs at 2626 and 730 cm^{-1}, so is unlikely to be present in significant quantities (Ji *et al.*, 2009). Siderite and other carbonates exhibit peaks around 880 and 730-750 cm^{-1}, coupled to a broad peak around 1500-1600 cm^{-1} (Dubrawski *et al.*, 1989; Bishop *et al.*, 2013). Both the presence of organics or mineral impurities could explain the noisiness between 1500 and 3000 cm^{-1}.

The fact that the small doublet at 3666 and 3653 cm^{-1} within the characteristic fork consists of two distinct peaks, as well as the equal intensity of the absorption bands at 797 and 750 cm^{-1}, are indicative of well-ordered kaolinite (Russell and Fraser, 1994). Illite content seems to be low because it exhibits a characteristic absorption doublet at 825 and 750 cm^{-1} to which the very small band at 833 cm^{-1} can be attributed (Fig. 3.5.4).

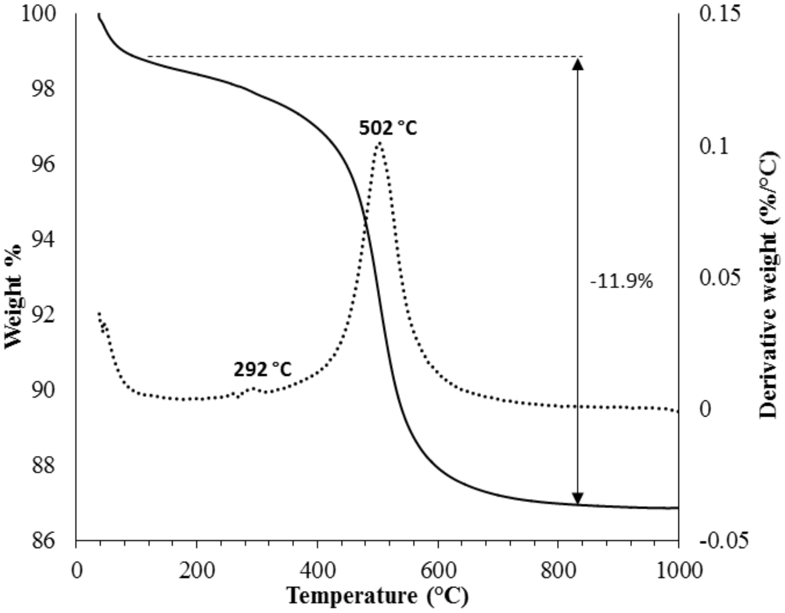

Figure 3.5.5. TGA spectrum of the fine fraction (SP-fine) of the sample São Pedro.

TGA: The TGA pattern is typical for kaolinite with a somewhat lower dehydroxylation temperature than KGa-1b, which corresponds to the lower kaolinite fraction present in this sample. A bump at 292 ºC hints to the presence of minute amounts of organics.

NMR: The ^{13}C CP-MAS NMR spectrum indicates that no significant amounts of organic matter was present in the parent material (Fig. 3.5.6).

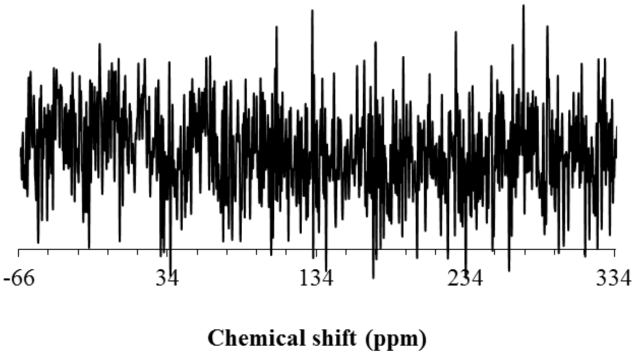

Figure 3.5.6. ^{13}C CP-MAS NMR pattern of SP-fine confirming no carbon was initially present (43320 scans)

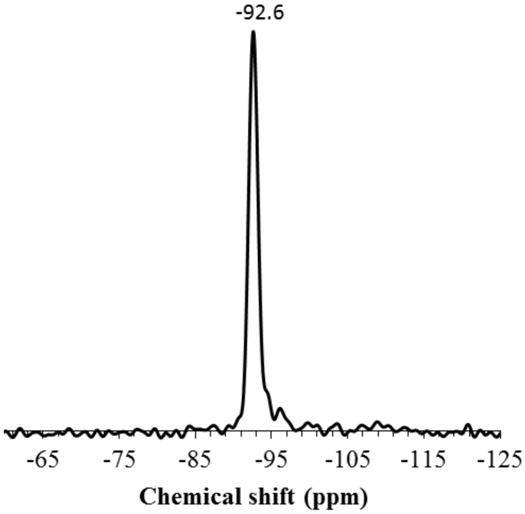

Figure 3.5.7. ^{29}Si CP-MAS NMR pattern of SP-fine (4434 scans)

The ^{29}Si CP-MAS NMR spectrum exhibits one peak differing by 1.2 ppm from the corresponding spectrum of KGa-1b (Fig. 3.4.7) at -92.6, suggesting the presence of zero next-nearest neighbour Al in the tetrahedral sheet as well as Q3 polymerization of phyllosilicates (Magi *et al.*, 1984; Goodman and Chudek, 1994). Russell and Fraser note that iron-containing samples may require longer experimental times due to dipolar interactions and a higher magnetic sensitivity overall (Russell and Fraser, 1994) which would explain somewhat higher noisiness despite a greater number of scans compared to KGa-1b. Irregularity around the central peak, particularly around -95.5 ppm could also be due to illite, which can have very broad and noisy spectra ranging from around -80 to -100 ppm (Thompson, 1984; Altaner *et al.*, 1988).

3.5.2. Characterisation of SP-DMSO precursor and its DTOD-grafted derivative

The characterisation results of SP-DMSO precursor product show an increase in d-spacing to 11.3 Å, conform to observations in K-DMSO presented in section 3.4.2. The *060* reflection persists throughout all modifications (Fig. 3.5.8). Its initial relative intensity is less than that of KGa-1b, but it also experiences less reduction throughout the modifications and exhibits a similar shape as the modified KGa-1b products (see Fig. 3.4.6).

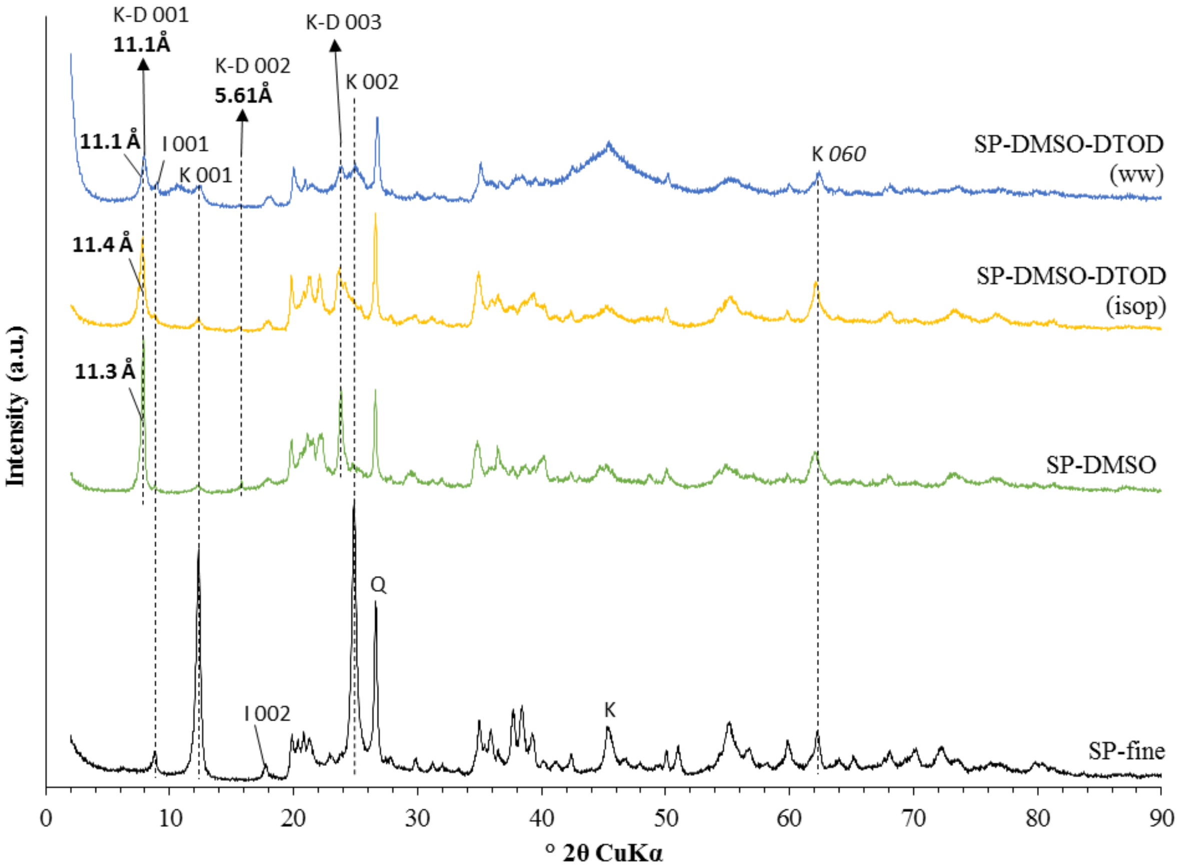

Figure 3.5.8. XRD pattern following the development of DTOD-grafted SP-DMSO precursor. SP-fine included for more convenient comparison. K-D refers to DMSO-intercalated kaolinite.

Both the XRD (Fig. 3.5.8) and the NMR spectra (Fig. 3.5.9) show that intercalation of DTOD did not occur. In XRD the d-spacing increased to 11.3 Å of DMSO-intercalated kaolinite (e.g. Frost *et al.*, 1998; Letaief and Detellier, 2005) from where it slightly collapses to a lower-intensity 11.1-Å peak after washing in water. As suggested by ^{13}C NMR, this is because only a small amount of organic loading of DMSO remains while no sign of DTOD can be detected in either the isopropanol-washed or water-washed DTOD samples. Although it is known from TGA of K-DMSO (Fig. 3.4.10) that DMSO is lost between 100 and 200 ºC, it seems from the NMR spectrum of SP-DMSO that some DMSO remains in the interlayer with only the kaolinite-DMSO link reflected by the 43.1-ppm peak of SP-DMSO remaining. Therefore, it would seem that the hydrogen bond with the octahedral sheet has been broken and only some DMSO is remaining in the ditrigonal opening of the tetrahedral sheet. Excess surface-deposited DMSO is not a problem in this sample.

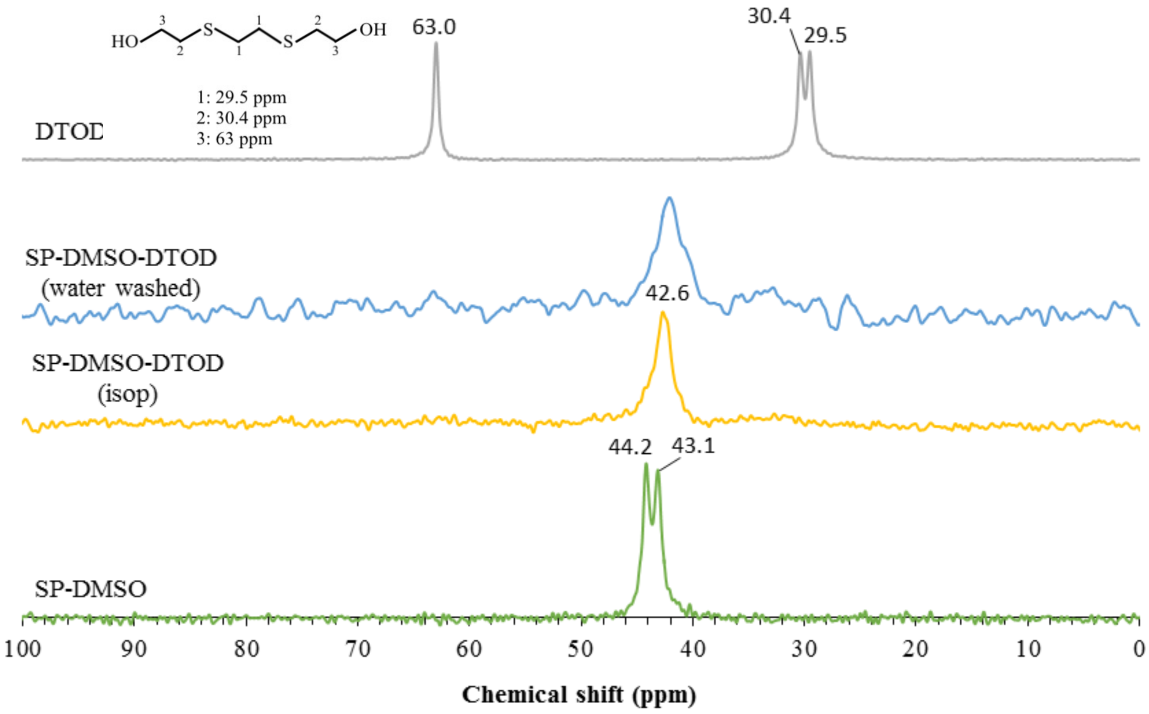

Figure 3.5.9. ^{13}C CPMAS NMR spectra following the development of DTOD-grafted SP-DMSO. Spectrum of DTOD is included for reference.

FTIR was only run for the DMSO-intercalated precursor sample of SP and is included in Appendix C.1.

3.5.3. Characterisation of SP-urea precursor and its DTOD-grafted derivative

The XRD peak of urea-intercalated kaolinite in São Pedro partially overlaps with the peak of illite, and it is clear that its relative intensity is not as pronounced as in the KGa-1b sample (Fig. 3.4.11) while the intensity of kaolinite *001* reflection is drastically worn down (Fig. 3.5.10). This may signify a greater extent of delamination. Persistence of the *060* reflection of kaolinite demonstrates that the integrity of the clay mineral was not damaged. A layer spacing increase of only 3.2 Å is observed when urea is intercalated, corresponding to an interlayer space that is 0.2 to 0.4 Å tighter than previously published results (Tsunematsu and Tateyama, 1999; Letaief *et al*., 2006; Zhengbang *et al*., 2007; Mahdavi *et al*., 2014), but the corresponding reflections here are rather amorphous. As for the thio-modified kaolinite produced from K-urea, some degree of exfoliation seems to have occurred based on the broad almost inexistent peak corresponding to the intercalated SP clay overlapped by I*001*.

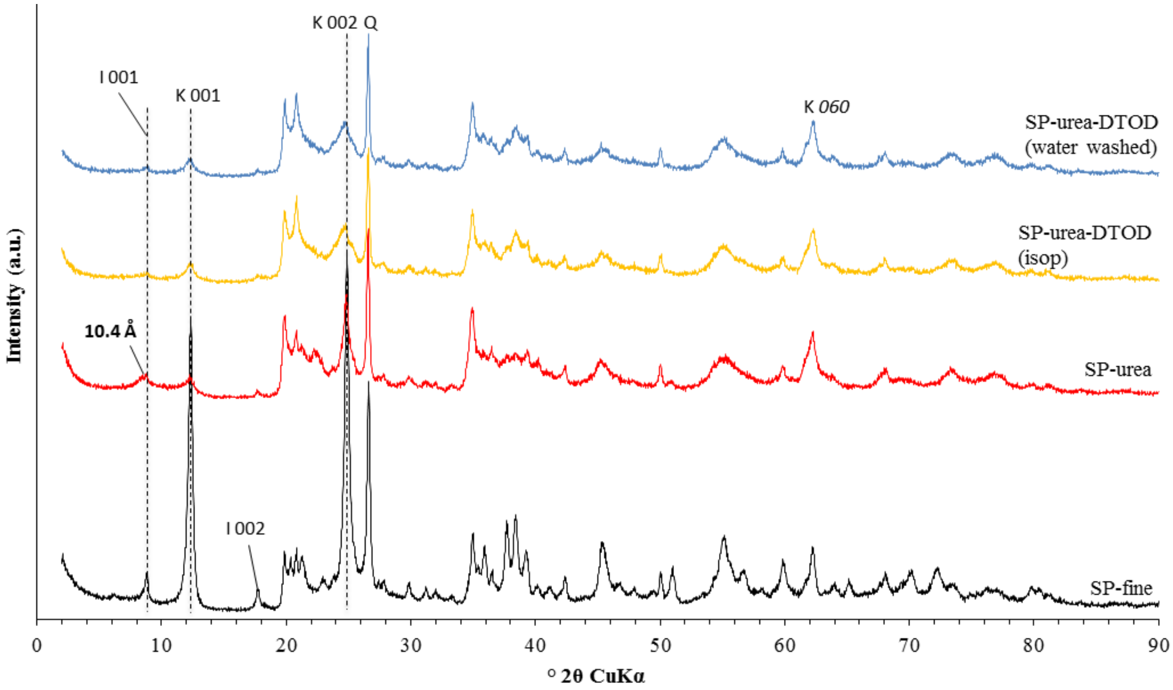

Figure 3.5.10. XRD patterns following the development of DTOD-grafted SP-urea precursor. SP-fine included for more convenient comparison.

<u>NMR:</u> NMR spectroscopy reveals a typical spectrum for kaolinite-urea intercalate with a chemical shift at 162 ppm (Letaief *et al*., 2006; Letaief *et al*., 2011) that also corresponds to urea on its own (Fig. 3.5.11). Resonances observed for the DTOD-modified samples are as in the modified K-urea precursor (Fig. 3.4.12), hence the same interpretation applies: Increase in the number of resonance peaks suggests the creation of new magnetic environments that

may occur by intercalation with the interlayer surface of DTOD by one of its ends. Absence of the irregularities in the isopropanol-washed SP sample, which was a nice powder without granules, supports the idea that excess DTOD was associated with the KGa-1b sample.

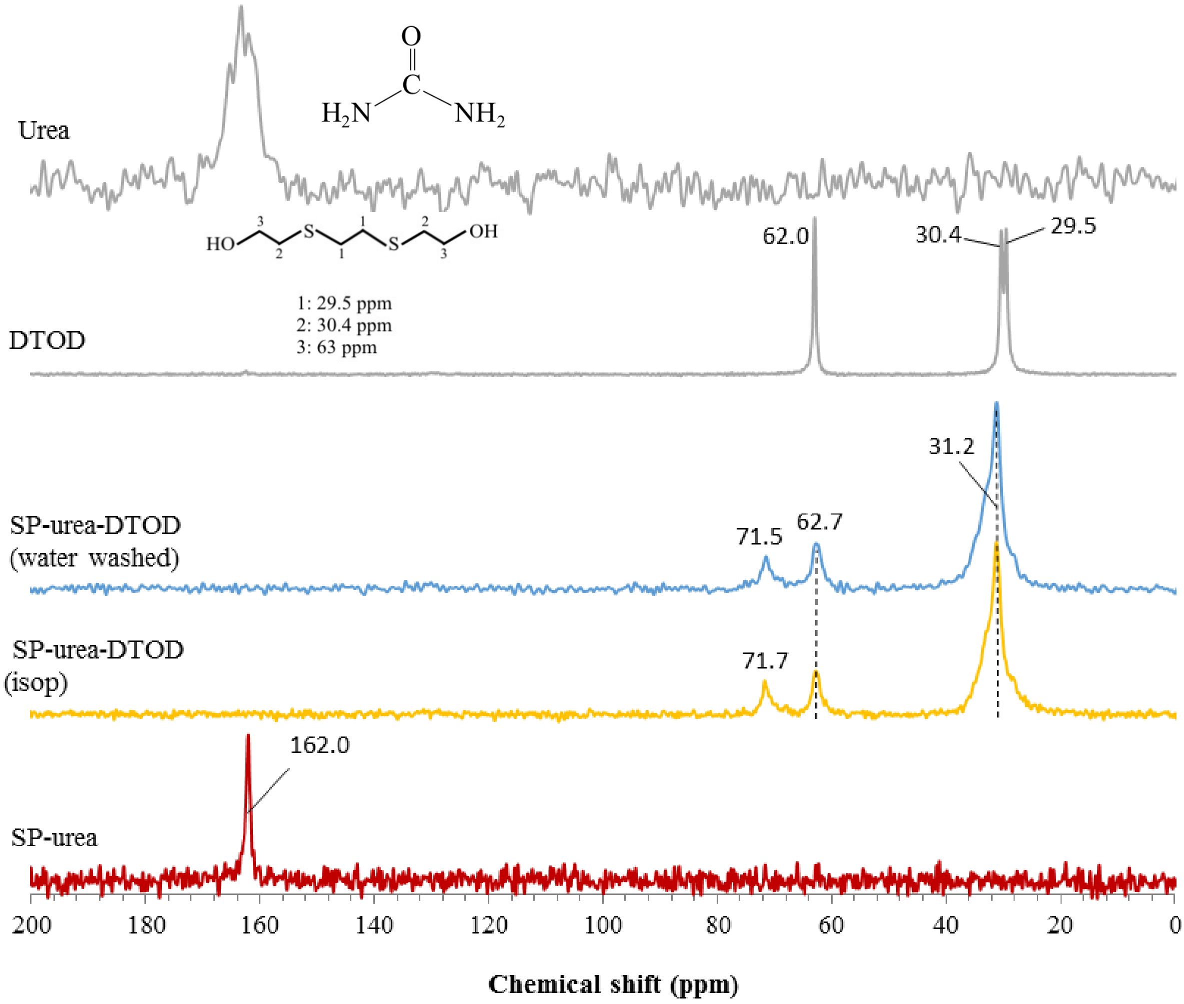

Figure 3.5.11. ^{13}C CP-MAS NMR spectra following the developments of DTOD grafting onto SP-urea precursor (25628 scans), showing the isopropanol (isop) washed product (isop; 4900 scans; line broadening = 5 Hz) and the subsequently water-washed product (6881 scans). Spectra of DTOD (2700 scans) and urea (112 scans; line broadening = 20 Hz) are included for reference.

The ^{29}Si NMR spectra does not exhibit any significant change from the natural sample SP-fine (Fig. 3.5.12), suggesting grafting to the inner octahedral surface may be more likely.

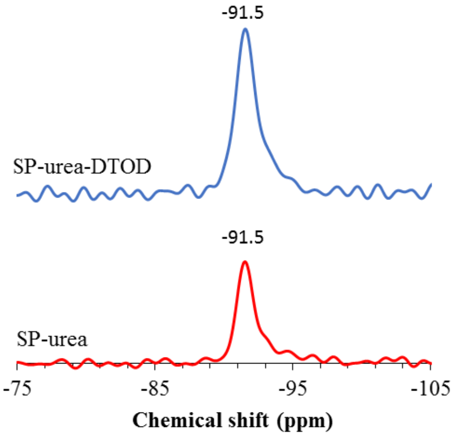

Figure 3.5.12. ^{29}Si CP-MAS NMR spectrum of SP-urea precursor and its DTOD-grafted derivative SP-urea-DTOD.

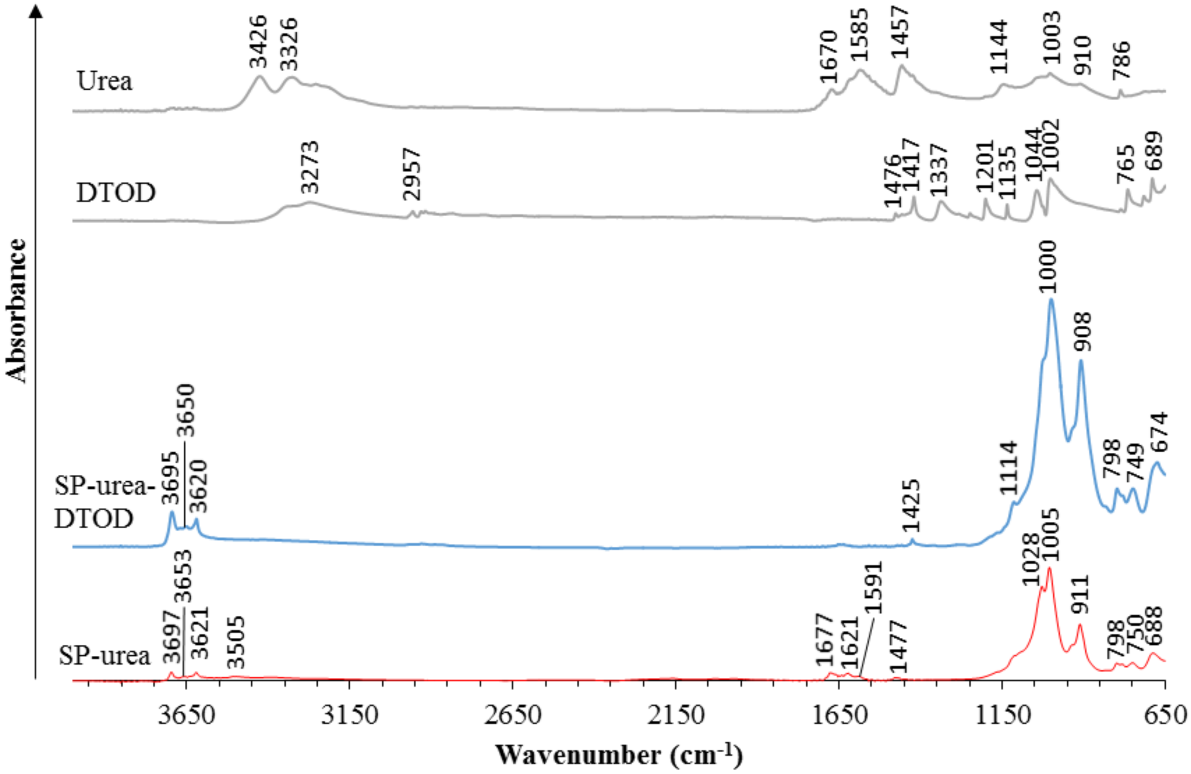

Figure 3.5.13. FTIR spectra following the development of DTOD-grafted SP-urea precursor. Spectra of DTOD and urea are included for more convenient comparison.

FT-IR: Interpretation of the FT-IR absorbance bands of SP-urea (Fig. 3.5.13) differs from the one presented for K-urea only in the Si-O vibrations occurring at 798 and 750 cm^{-1} (instead of 780 and 745 cm^{-1} in K-urea; Fig. 3.4.14), which may be attributed to the higher quartz content.

TGA: The TGA pattern of urea is more or less in agreement with the previously presented pattern of K-urea. The thio-kaolinite, however, exhibits a remarkably lower heat resistance indicative of weaker bonds between DTOD and kaolinite's inner surface (Fig. 3.5.14). In fact the first decomposition peak occurs at practically the same temperature as DTOD in isolation (Fig. 3.3.5b), so it might correspond to the compound on the outer surface of clay. Subsequent kaolinite dehydroxylation occurs at more or less the same temperature.

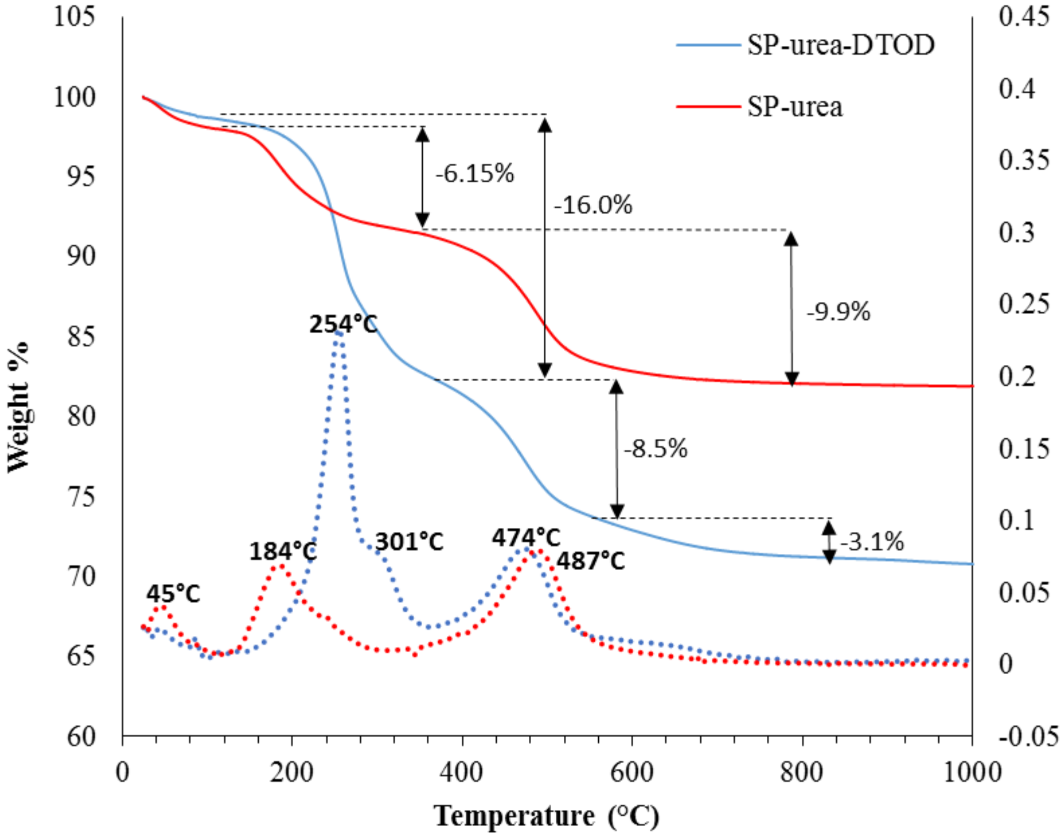

Figure 3.5.14. TGA patterns of SP-urea precursor and its DTOD-grafted derivative SP-urea-DTOD. Heated under nitrogen atmosphere.

Calculation of the organics loading yielded 0.29 mole urea per kaolinite unit in SP-urea and 0.27 mole DTOD per kaolinite unit in SP-urea-DTOD, considerably less than its KGa-1b counterpart K-urea-DTOD. Yet, also this sample exhibited a slight granule-like quality similar to that of K-urea-DTOD, which may support the hypothesis that urea samples are exfoliated leading to DTOD grafting on exfoliated surfaces, whereas in the K-DMSO precursor DTOD is really grafted in the interlamellar space.

3.6. Some remarks on grafting of DTOD

As was observed here by comparison of the thio-kaolinite originating from the urea- and the DMSO precursors, the configuration of grafted organo-kaolinites is known to depend heavily on the methodology applied (Tonlé, 2011), including both the preparation of the precursor as well as the process and parameters of the grafting step. Some general remarks and observations made during the grafting process might be useful for anyone who wishes to pursue the study of thio-kaolinite further. Grafting of DTOD was found to be a delicate process with all clay samples. Despite the fact that excess organic material is necessary to obtain a stable intercalated kaolinite (Raussel-Colom and Serratosa, 1987), an overly high loading of DTOD can lead to a very sticky material that is impossible to wash with isopropanol. A ratio of about 5 to 7 g DTOD to 1 g clay was found to work well, where 7 g probably approached the upper limit, as this amount of DTOD led to a material that contained only a minor amount of sticky particles. The success of the process may also be related to the contact time, i.e. the length of the melt-intercalation, though no big texture differences were observed here between 6 and 20 hours. Temperature optimisation could be studied too. Yang *et al*. (2012) experimented with the melt-intercalation grafting of γ-aminopropyl triethoxysilane (APTES) onto DMSO-precursor kaolinite at temperatures around the boiling points of both organic compounds (range of 175-220 ºC) and found the most successful grafting method, in monolayer arrangement and effective replacement of DMSO, to be at the highest temperature tested (220ºC) where APTES boils but does not pyrolyse. DTOD has a boiling point of 170ºC and a melting point of 63-64ºC (Sigma-

Aldrich, 2015a), urea melts between 132 and 135 ºC (Sigma-Aldrich, 2015b), DMSO has a boiling point of 189 ºC (Sigma-Aldrich, 2015c), so depending on the precursor, a melt-intercalation at an adjusted temperature from the one used for this study may lead to a more reproducible methodology.

3.7. Conclusions

In this chapter starting materials and synthesised products were characterized, each analytical technique giving cues about different components of the organo-clay associations and contributing to a general hypothesis on whether and how each clay sample was grafted. XRD gave information about the interlayer space that may be occupied after each reaction stage. NMR gave information about the magnetic environment of the organic moiety and consequently on the location in the molecule where a new bond with the kaolinite surface may occur. FT-IR gives cues about new types of bonds that may have formed and how existing bonds have been affected. TGA provides information about the amount of the organic moiety that has been inserted and how each modification affects the dehydroxylation temperature of the kaolinite mineral as well as the general heat resistance of the material.

The results suggest that the compound 3,6-dithia-1,8-octanediol was successfully melt-intercalated in the precursor samples K-urea, K-DMSO and SP-urea, to obtain the products K-urea-DTOD, K-DMSO-DTOD and SP-urea-DTOD. Negligible changes observed in the relevant patterns and spectra after washing in water for 24 hours are a strong indication that the organic moiety was grafted, particularly because the d-spacing of the *001* reflection of the expanded kaolinite exceeds that of water-intercalated kaolinite. TGA patterns show an increased heat resistance of DTOD compared to the isolated material in the grafted kaolinites of KGa-1b.

Functionalisation of the DMSO precursor (K-DMSO) leads to a comparatively large increase in d-spacing corresponding to an interlayer space of 4.5 Å. The presence of only two large peaks (one of which is probably composed of two overlapping resonances) in ^{13}C NMR spectra confirms the organic moiety is present in the sample and suggests bonding with the interlayer surface by both ends of the DTOD chain. FT-IR demonstrates that DTOD may be grafted onto both siloxane surface and aluminol surface, though the former is not supported by ^{29}Si NMR analysis. Thermal analysis displays an increased heat resistance and four mass loss events that correspond to a loading of 0.29 to 0.4 mole of DTOD per mole of kaolinite.

The urea precursors behave differently when intercalated with DTOD. XRD analysis suggests exfoliation of K-urea-DTOD and SP-urea-DTOD and, where present, an interlayer space of 4 Å. Analysis by ^{13}C NMR confirms the presence of the organic moiety and indicates the thio-compound was probably grafted by one end, from where it radiates into the interlayer space. FT-IR suggests that this occurs on the inner octahedral surface, though the possibility of interaction with the siloxane surface is not excluded. TGA of K-urea-DTOD exhibits an increased heat resistance and a very high loading of 1.51 mole of DTOD per mole of kaolinite, compared to a more weakly grafted species in SP-urea-DTOD (lower heat resistance) with a loading of only 0.27 mole per mole of kaolinite.

The marked differences in the graftability of DTOD on the two sets of urea- and DMSO-precursor products indicates that KGa-1b, São Pedro and their derivatives exhibit a distinct surface chemistry, the consequences of which will also be observed in their sorption behaviour in the next chapter.

CHAPTER 4
Heavy metal sorption studies

4.1. Rationale

One can find many studies in the scientific literature on heavy metal sorption by modified and/or natural clay minerals from simple solutions prepared by mixing metal salts in deionised (DI) water. Exhibiting a minimal number of variables, these systems can reveal the principal sorption mechanisms. This is one approach that was included in this study to determine the uninhibited zinc sorption capacity of each clay sample tested. As far as the author is aware, zinc sorption onto the reference clay KGa-1b has not been reported at this time.

Indeed, the potential of clay mineral materials to remove heavy metals in solution has been well illustrated in the literature using such "simple-system" approaches. However, apart from anecdotal evidence on the use of clay as a water purifier, medicinal aid in case of poisoning (Churchman *et al*., 2006), and perhaps application as a sorbent of excess fluorine in drinking water (Murray, 2007), studies on their use as a metal sorbent in actual wastewaters are rare – an observation that has also been made by the authors of a recently published paper on zinc remediation in wastewater from a metal plating facility (Hojati and Landi, 2015). Nonetheless, there seems to have been a peculiar recent interest at numerous conferences in the remediation of car-wash wastewater with this simple and inexpensive adsorption method to reduce COD, TSS, oils and grease contents (Kim *et al*., 2013; Baddor *et al*., 2014; Enoh and Christopher, 2015), as well as in the use of clay as a coagulant of organic contaminants and accelerator of particle settling and COD remediator (Jiang *et al*., 2004), but none of these studies have focused on heavy metal removal. Particularly application of grafted clay minerals in real wastewater or a comparison between performance in a model system versus a real system has received no coverage in the literature. Therefore, this study comprises another set of sorption studies performed in real wastewater, a complex mixture exhibiting countless variables and interactions that may potentially enhance or inhibit the ability of clay sorbents to remove heavy metals from solution.

A secondary reason for testing in wastewater is due to its natural buffering capacity (presence of phosphates, ammonium nitrates, etc.), minimizing the pH sensitivity of the sorption process with kaolinite, which is not only known to exhibit a pH dependent sorption capacity, but also to affect the pH of its surroundings upon metal sorption (Miranda-Trevino and Coles, 2003). Therefore, the need for addition of a buffer is avoided, which is known to compete with zinc for sorption onto kaolinite (Dimirkou *et al*., 2002)

Since the government constitutes the majority of activities in Ottawa and there is no pollution from major factories, heavy metal pollution is not a major concern (T. Lewis, 2015, pers. comm., 10 July). When spiked with zinc, the low-background-level wastewater environment is an appropriate model system for the zinc-sorption capacity of the the thio-kaolinite nanohybrid materials in a realistic environment.

4.2. Chemical reagents

Concentrated nitric acid (Fisher, trace metal grade) was diluted to 1%, $ZnCl_2$ (Sigma-Aldrich, 98% purity) was dissolved in deionised (DI) water or wastewater depending on the sample set, raw sewage was obtained from the Robert O. Pickard Envrionmental Centre in Ottawa (sampled after initial screening; see Fig. 1.3.2).

4.3. Methodology of sorption studies

Sorption of zinc was tested for the successfully grafted samples (K-DMSO-DTOD, K-urea-DTOD, and SP-urea-DTOD) and compared to the natural fine fractions of each parent material (K-fine and SP-fine). Sorption experiments were performed in three stages: (1)

preliminary study using different additions of the bulk fraction of KGa-1b and wastewater; (2) study of simple system using a 5 mL $ZnCl_2$ solution, and 50 mg of each clay sample; and (3) study of spiked wastewater system using 5 mL Zn-spiked wastewater, and 50 mg of each clay sample. $ZnCl_2$ is very hygroscopic, so the exact initial concentrations had to be measured by ICP-MS. The initial concentrations of zinc in set 2 and 3 are included in Figures 4.5.2 and 4.6.2. The treatments in the sample sets used at each stage are further specified in Table 4.3.1.

Table 4.3.1. Lists of sample sets studied at each stage. Each treatment was performed in triplicate unless otherwise noted. Treatment names referred to in subsequent figures are underlined.

Sample set 1: preliminary study	Sample set 2: simple system	Sample set 3: wastewater system
5 mL WW[a] + 5 mg K-bulk	5 mL Zn solution[b] + 50 mg K-fine	5 mL Zn-spiked WW[c] + 50 mg K-fine
5 mL WW + 10 mg K-bulk	5 mL Zn solution + 50 mg K-urea-DTOD	5 mL Zn-spiked WW + 50 mg K-urea-DTOD
5 mL WW + 20 mg K-bulk	5 mL Zn solution + 50 mg K-DMSO-DTOD	5 mL Zn-spiked WW + 50 mg K-DMSO-DTOD
5 mL WW + 50 mg K-bulk	5 mL Zn solution + 50 mg SP-fine	5 mL Zn-spiked WW + 50 mg SP-fine
5 mL WW + 100 mg K-bulk	5 mL Zn solution + 50 mg SP-urea-DTOD	5 mL Zn-spiked WW + 50 mg SP-urea-DTOD
5 mL WW (standard)	5 mL Zn solution (standard)	5 mL Zn-spiked WW (standard)
5 mL unfiltered WW	5 mL Zn solution (initial concentration) not subject to shaking or centrifugation	5 mL Zn-spiked WW (initial concentration) not subject to shaking or centrifugation (5 replicates)
5 mL DI water + 100 mg K-bulk (metal test)		5 mL WW (baseline metal concentrations)
		5 mL effluent (2 replicates)

[a] WW: wastewater
[b] Zn solution: $ZnCl_2$ salt in DI water
[c] Zn-spiked WW: solution of $ZnCl_2$ in wastewater

Apart from standards, one of the treatments in sample sets 2 and 3 did not undergo any shaking or centrifugation. These were used to calculate the initial concentration. Standards could not be used to that end mostly because of possible sedimentation of analytes by centrifugation. This sample-set order was designed such that the procedure could be adjusted if necessary from the results obtained as more and more scarce clay samples were used.

Raw sewage was obtained from the Robert O. Pickard Environmental Centre, the wastewater treatment plant of the city of Ottawa, on 20 March for the preliminary study and on 10 July for experiment set 3. Common wastewater quality indicators measured every-other day at the plant have been included for the relevant sampling days to indicate the extent of variability of these wastewater properties (Appendix E). A more homogeneous mixture was obtained by vacuum filtering the wastewater twice using no. 1 Whatman filter paper (90-mm Ø, cat no 1001 090; particle retention up to 11 µm). Mostly algae and suspended solids were recuperated and one small worm species.

Effluent water was also collected on 10 July to be able to compare the removal efficiency of the wastewater treatment plant and of the modified kaolinite samples. Effluent water from the Robert O. Pickard Environmental Centre is discharged into the Rivière des Outaouais. As its flow rate is very high, there are practically no limits on the ammonia concentration of effluent water, so that it reaches levels ranging from 20 to 40 mg/L, while other plants discharging into smaller water bodies may need to limit their effluent NH_3 concentrations to <5 mg/L (T. Lewis, 2015, pers. comm., 10 July). NH_3 is known to play a role in algal blooms, which was also observed in the raw sewage from 20 March that was left in the lab. This is partly why fresh sewage water was picked up for the subsequent experiment, and also because of other non-visible biochemical processes that may have taken place.

Table 4.3.2. Limits of detection (ppb) of the analytes quantified as well as the isotopes and CRC mode used for the elemental quantifications, collision mode (He) or no-gas mode (NoHe).

	Zn	Ni	Cu	As	Cd	Hg	Pb	Na	Mg	S	Ca	Cr	Mn	Fe
Set 1	0.023	0.009	0.001	0.000	0.005	0.015	0.006	0.281	0.141	-	0.416	0.022	0.027	1.092
Set 2	0.023	0.017	0.003	0.008	0.006	-	0.008	13.78	0.406	-	1.75	0.04	0.02	2.84
Set 3	0.157	0.013	0.030	0.002	0.002	0.186	0.004	7.886	0.461	0.107	2.607	0.023	0.028	1.038
Isotopes used for quantification and reaction cell settings:														
Set 1	66 NoHe	60 NoHe	63 He	75 He	111 NoHe	201 NoHe	208 NoHe	23 NoHe	24 NoHe	-	44 NoHe	52 NoHe	55 NoHe	57 He
Set 2	66 NoHe	60 NoHe	63 NoHe	75 NoHe	111 NoHe	-	208 NoHe	23 NoHe	24 NoHe	-	43 NoHe	52 NoHe	55 NoHe	57 NoHe
Set 3	66 NoHe	60 NoHe	63 NoHe	75 He	111 NoHe	201 NoHe	208 NoHe	23 NoHe	24 NoHe	34 He	43 NoHe	52 NoHe	55 NoHe	57 NoHe

Quality control of each ICP-MS run included rinsing with nitric acid, DI water, the metal standards mix A and mix B (see Table 2.5.2) at concentrations of 12.5, 25, 50, and 100 µg/L, and a final check of a known concentration. Several blanks were run with HNO_3 to calculate the limit of detection (Table 4.3.2). Data below the detection limit were not included in the results or shown as zero. Both natural clay samples (KGa-1b and SP) are known to contain titanium, either based on anatase observed in XRD and/or directly by elemental analysis. Therefore Zn analysis was checked for overlap by TiO with helium collision mode. This interference was not found to differ significantly from results obtained by no-gas mode, such that the latter were used in the quantification. The isotope and CRC mode (see section 2.5) used for each analyte were those that exhibited the lowest limit of detection, as presented in Table 4.3.2.

Data processing for each analyte involved corrections for any dilutions performed and normalization to the actual amount of solution and clay sample added to each vial (i.e. 4.979 mL solution and 49.5 mg clay for example) and the amount of zinc sorbed per gram of clay was determined. Subsequently % sorption was calculated where appropriate:

$$\%sorption = \frac{initial\,concentration - final\,concentration}{initial\,concentration}\ 100$$

Finally, a supernatant concentration was calculated for an ideal solution and clay mass (i.e. exactly 50 mg of clay and exactly 5 mL of solution), with the assumption that a linear relationship between the clay concentration and the sorption exists within a clay-concentration variation of no more than 2.1 mg in set 1, 0.9 mg in set 2, and 1.3 mg in set 3. An example of the data processing is included in Appendix D.

4.3.1. Preliminary study

Preliminary sorption studies were performed with the aim of finding out what metal(s) adsorb well onto the clay sample and to determine an appropriate clay addition. Moreover, the metal concentrations in the wastewater were not known initially and the need for and degree of metal spiking had to be assessed.

K-bulk was used because it was an abundant sample (there was not sufficient K-fine for use in a preliminary study) and its characterization showed a high purity, very similar to K-fine (see section 3.4.1). First the appropriate amount of K-bulk was added to 5 mL wastewater in a plastic 15-mL centrifuge vial (see sample list in table 4.3.1). Clay additions of 5 to 100 mg were used. A standard of wastewater only was also prepared, as well as a standard of unfiltered wastewater to test if metals were filtered out as complexes with organic and suspended solids. Finally, in order to account for metals released by the clay itself, a vial containing 5 mL DI water and 100 mg clay was prepared, with a pH lower than wastewater giving an upper boundary of metals released.

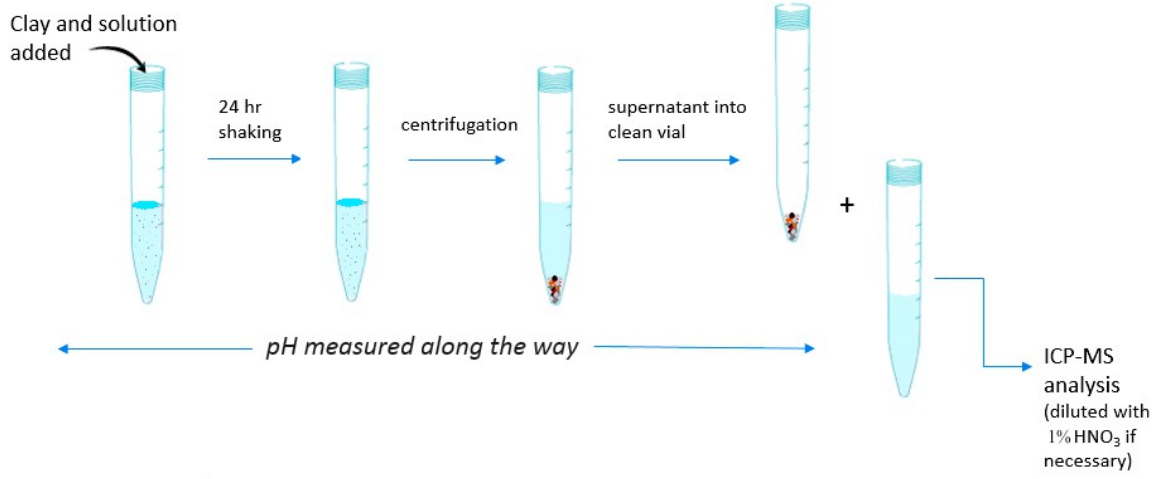

Figure 4.3.1. Diagram illustrating the general procedure followed for all sorption experiments.

In accordance with the procedure illustrated in figure 4.3.1, all tubes were then shaken horizontally on a rotary shaker at 300 rpm for 24 hours. Subsequently the pH of each mixture was measured using a Fisher Scientific Accumet AB15 basic pH meter (calibrated with buffer solutions of pH 4, 7, and 10). All tubes were then centrifuged, and their supernatants poured into clean vials. The pH was measured again and the supernatant solutions' metal concentrations were analysed by ICP-MS. Preliminary results were compared to previous studies found in the literature to determine an appropriate metal-to-clay mass ratio.

4.3.2. Simple system experiment

It was observed in the preliminary study (see results in section 4.4) that adsorption of zinc was obvious and increased at higher rates of clay addition, so simple systems were prepared by making a solution of 10 mg/L Zn(II) in DI water using $ZnCl_2$ salt (measurement of the exact zinc concentration relied on ICP-MS analysis). For each treatment, 50.0 mg of a natural fine fraction or thio-kaolinite sample was added to 5.0 mL of this solution (clay concentration of 10 g/L). A standard containing no clay was also included in the set as well as three solutions that were kept aside and not subject to any shaking or centrifugation to measure the initial concentration.

The clay and zinc concentrations used are comparable to those reported by Mbaye *et al*. (2014), who studied the sorption of lead onto natural and modified kaolinite using 100 mg clay in 10 mL solutions and found optimum sorption at a lead concentration of 10 mg/L.

Following the process illustrated in Fig. 4.3.1, samples were shaken horizontally at 300 rpm on a rotary shaker for 24 hours and all supernatant solutions were diluted 10 times with 1% nitric acid to prevent overloading of the ICP-MS equipment.

4.3.3. Wastewater system experiments

In the last set of experiments spiked wastewater systems of about 10 mg/L Zn^{2+}, using $ZnCl_2$ salt, were tested with 50.0 mg of natural fine fractions and thio-kaolinite samples. Since preliminary studies indicated negligible zinc presence compared to the desired concentration of 10 mg/L, initial presence in the wastewater was not taken into account when preparing the spiked wastewater. Nonetheless, baseline concentrations of the wastewater were still measured. Wastewater was filtered within 24 hours after pick-up at the wastewater treatment plant. All samples were subject to the same treatment as aforementioned, except for the initial-concentration-, effluent-, and baseline vials, which were not subject to any centrifugation to avoid encouraging analytes to precipitate out of solution.

4.4. Results and discussion of sorption set 1 – Preliminary study

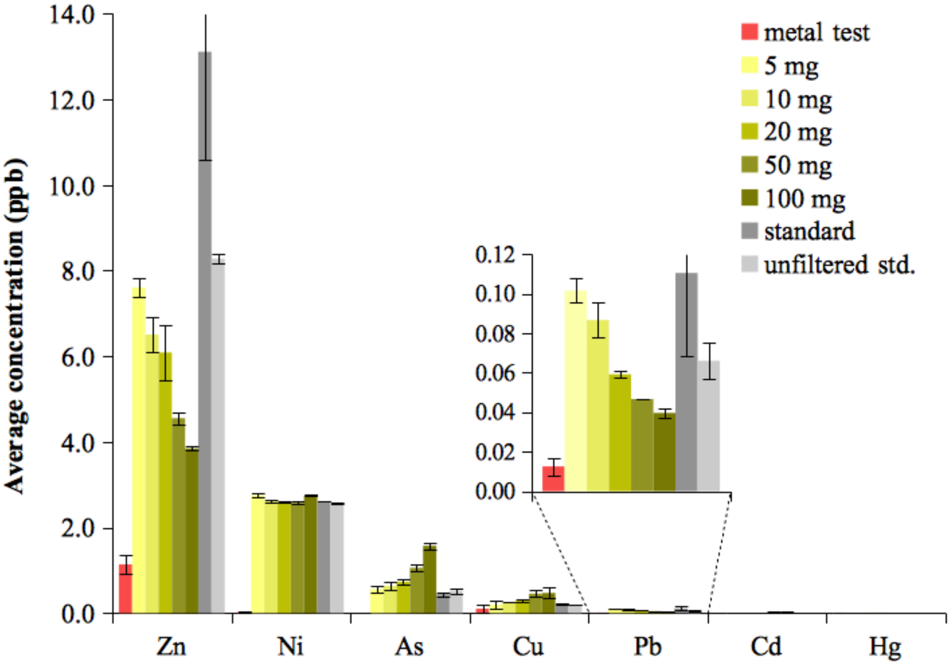

Figure 4.4.1. Average final concentrations of concomitantly measured metals by ICP-MS in supernatant solutions of the preliminary study (sample set 1) after shaking and centrifugation. Error bars represent standard errors of the mean. Where bars are absent, the concentrations were below the detection limit.

Metal concentrations in the raw wastewater were very low, in the ppb range (Fig. 4.4.1). Fortunately ICP-MS is very sensitive (up to ppt) and error margins are mostly brought about by sample preparation and homogenization. Metal release from the KGa-1b bulk fraction (K-bulk) in water at a pH of 5.7 (Fig. 4.4.2) is very low, as may be expected from kaolinite, with the highest release observed for Zn of 1.14 ppb on average, followed by Ni (0.04 ppb) and Cu (0.02 ppb). Hg was the only metal that was not detected in any of the samples. These results are in accordance with previously performed trace element analysis where KGa-1b was found to contain higher amounts of copper and nickel than most other elements, though the clay also contains relatively high concentrations of cerium and strontium, which might be worthwhile including in the ICP-MS analysis in a follow-up study (zinc was not included; Appendix B.2.1; Kogel and Lewis, 2001).

As was expected with regards to current wastewater trends (section 1.3.3), the sewage contained relatively high zinc concentrations. Comparison of metal concentrations measured in the standard and the clay-wastewater mixtures shows potentially good sorption trends for zinc and lead, both of which exhibit a gradual decrease in concentration (in the supernatant) as the clay addition is augmented (Fig. 4.4.1). A high affinity of kaolinite for lead has been previously noted by various authors (e.g. Scrudato and Estes, 1975; Coles and Yong, 2002; Amer *et al*., 2010). However, concentrations of lead are very low in this assay, adding doubt to the significance of this interpretation.

It is further observed that zinc and lead concentrations are higher in the filtered wastewater than in the original unfiltered raw sewage. Comparison with raw sewage metal data from the Robert O. Pickard Environmetal Centre shows consistently higher metal concentrations in the wastewater samples used here (Appendix E), suggesting metals were sorbed to suspended organics and solids that were filtered out and must have sedimented while in the ICP-MS autosampling unit, such that they were not included in the solution that was sampled.

Nickel concentrations appear to be unaffected by the presence of K-bulk and filtering. Anagho *et al*. (2013) also report low (~16%) sorption rates of kaolinite for nickel. Arsenic, on the other hand, is not detected in the metal release test in water. Yet it is present in low concentrations in the clay-amended wastewater, suggesting that the combination of clay and wastewater seems to promote release of certain metals into solution. This might be related to zinc sorption on sites with a higher affinity for zinc than arsenic, such that the latter may be released.

There was unfortunately a minor flaw in the experimental set-up, namely that separate vials containing only wastewater and undergoing no treatment were not included, so the initial concentration was not measured. However, as is illustrated in a later section by a significant "sorption" in the standard of sample set 3, a standard undergoing centrifugation and shaking is not representative of the initial concentration because some analytes sorbed to a very small amount of particulate matter settle out of solution. In any case, it can be assumed that such removal by centrifugation was constant in all treatments, so comparison within this preliminary sorption set is valid for the purpose of calculating an optimal sorption per gram of clay. Nonetheless, due to a potential discrepancy with the real initial concentration, the % sorption will be referred to here as a semi-quantification of the % sorption (Table 4.4.1).

Table 4.4.1. Semi-quantification of the % zinc sorption and the relative improvement, in terms of zinc sorption, of a higher clay addition in 5 mL of wastewater.

Treatment	Zinc sorption	Relative improvement
5 mg K-bulk	42%	-
10 mg K-bulk	50%	8.2
20 mg K-bulk	54%	3.3
50 mg K-bulk	65%	**11.5**
100 mg K-bulk	71%	5.6

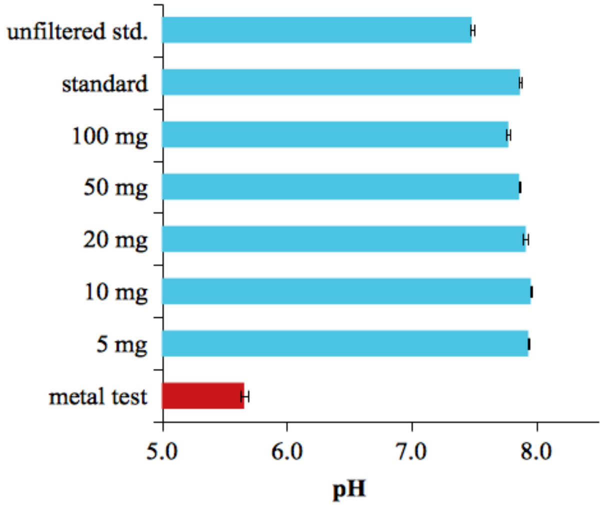

Figure 4.4.2. The pH after 24 hours of shaking of sample set 1. Error bars represent standard errors of the mean.

Semi-quantification and subsequent determination of the relative improvement shows that a clay addition of 50 mg yields optimum results (Table 4.4.1). For this reason, and because it matches clay concentrations used by other authors (e.g. Mbaye *et al.*, 2014), this clay addition (50 mg in 5 mL solution) was maintained for the subsequent sorption sets.

Finally, calcium, magnesium, chromium, iron and manganese concentrations were included in the ICP-MS analysis. Calcium and magnesium concentrations are as good as constant in all treatments with wastewater and hardly detected in the metal test in DI water (Fig. 4.4.3a). The same was observed for chromium and manganese (Fig. 4.4.3b and c). Iron, on the other hand, seemed to be sorbed by the clay (Fig. 4.4.3c), which may be another reason for some desorption observed for arsenic. To track potential release of metals other than the target heavy metal zinc, which may occur in a similar fashion as observed here for arsenic, other metal analytes were also included in the ICP-MS analyses of subsequent sorption sets.

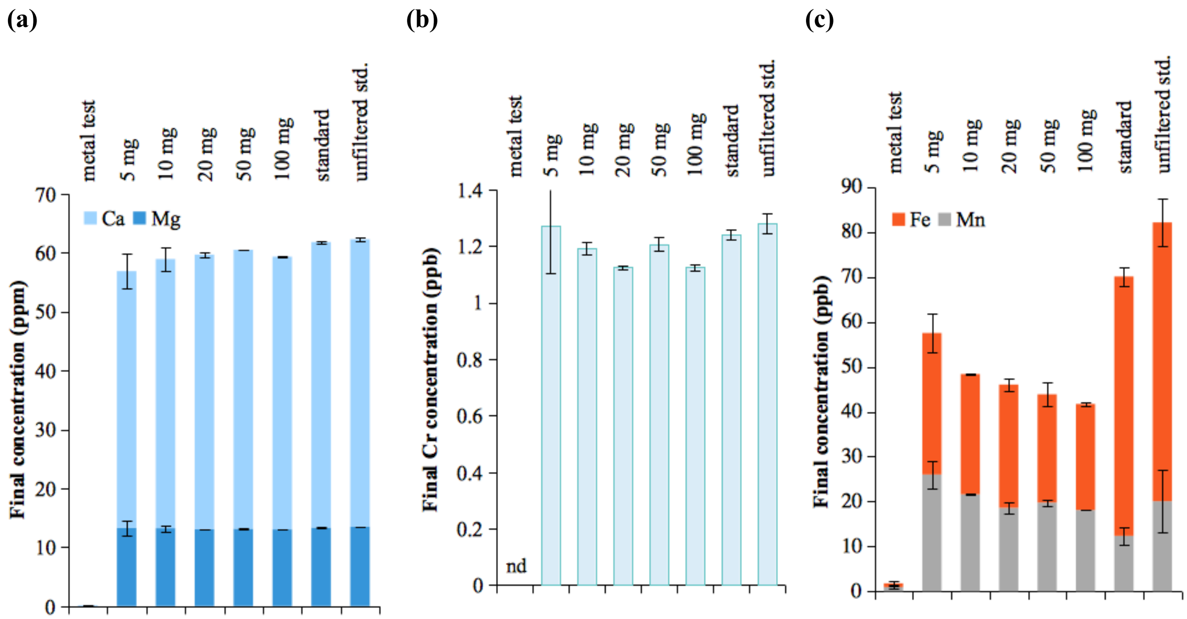

Figure 4.4.3. Average final concentrations of **(a)** calcium and magnesium, **(b)** chromium, and **(c)** iron and manganese in the supernatant solutions of the preliminary sorption study (sorption set 1) after shaking and centrifugation. Error bars represent standard errors of the mean. Sodium was over-range in all treatments.

4.5. Results and discussion of sorption set 2 – Simple system experiment

4.5.1. Zinc sorption

The zinc sorption efficiency of each clay sample, as well as the final concentrations found in the supernatant solutions after shaking and centrifugation are shown in Figures 4.5.1 and 4.5.2. The standard exhibits a removal rate that is near to nothing compared to the clay sorption rates. In the KGa-1b samples, the natural fine fraction (K-fine) removed less than half of the zinc in solution and the thio-kaolinite based on K-urea (K-urea-DTOD) even less. This might be due to the organic loading with DTOD which was too high, perhaps covering the non-thio sorption sites naturally present on the kaolinite, as well as the larger granules in this sample, leading to a less effective dispersion. K-DMSO-DTOD, on the other hand, offers the greatest improvement in sorption capacity as compared to its parent material (K-fine), from 38 to 64%.

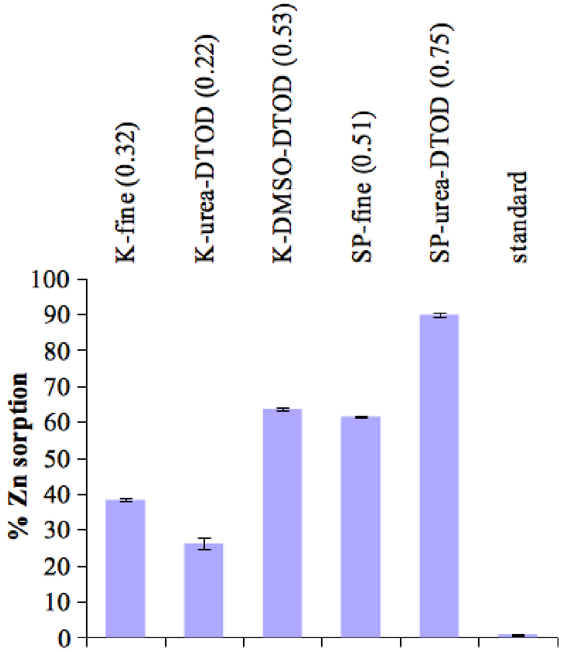

Figure 4.5.1. Average % zinc sorption by natural fine fractions and DTOD-grafted samples of KGa-1b (K) and sample São Pedro (SP) in zinc-spiked water. Numbers in parentheses give the amount of zinc sorbed in mg/g clay. Error bars represent standard errors of the mean.

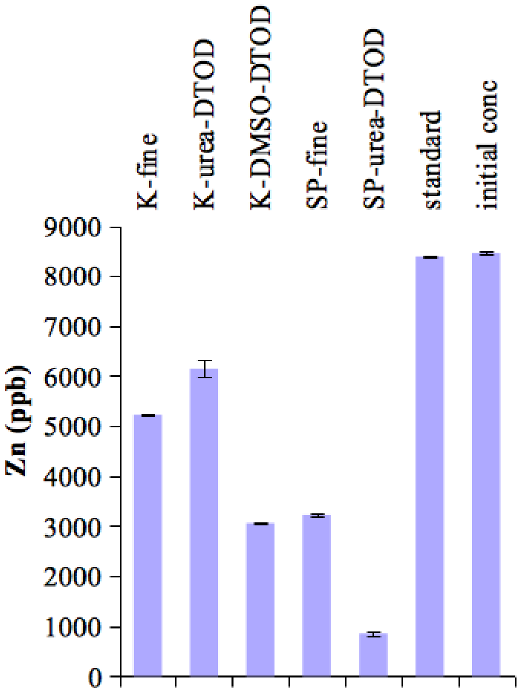

Figure 4.5.2. Average final concentration of zinc in the supernatant solutions of the zinc-spiked water for each clay-treated sample, the standard and the initial concentration, adjusted for the exact actual clay concentration. Error bars represent standard errors of the mean.

The natural fine fraction of sample São Pedro (SP-fine) has a higher inherent sorption capacity for zinc, removing almost as much as the thio-kaolinite derived from K-DMSO (K-DMSO-DTOD; Fig. 4.5.1). The highest sorption was obtained by the thio-kaolinite based on SP-urea (SP-urea-DTOD), which removed 90% of zinc, despite a relatively low loading of the chelating agent (see Fig. 3.5.14), suggesting the thio compound does not provide the only pathway to increased zinc sorption but rather the combination of increased surface area obtained by delamination with urea enhancing the sorption capacity of the natural fine fraction, boosted by a chelating functionality of DTOD. Moreover a moderate loading with DTOD leaves access to sorption and chelating sites, while these were probably blocked up in the sample K-urea-DTOD. The loading of 0.32 and 0.51 g. zinc per g. unmodified clay corresponds to 4.7 and 7.8 mmol/g clay, considerably higher than the zinc sorption of 8.4 µmol/g obtained with a large-particle-size kaolinite by Miranda-Trevino and Coles (2003) who used around 10 times more concentrated zinc solutions. Figure 4.5.2 shows the final concentrations measured by ICP-MS, to indicate the significance of the derived percentage sorption values.

The big difference in sorption performance of the thio-functionalized urea precursors (K-urea-DTOD and SP-urea-DTOD) is surprising. Perhaps the grinding time used to intercalate urea was too long in the case of K-urea-DTOD, which is known to lead to a decreased surface area and increase in particle size (Sánchez-Soto *et al.*, 2000). The higher sorption efficiency of SP-fine may also be related to its high iron content, as well as some manganese oxides (McLean and Bledsoe, 1992), to which metal cations (M) can sorb following the reaction scheme:

$>\text{Fe-OH}]^{-1/2} + \text{M(H}_2\text{O)}_6^{n+} \rightarrow >\text{Fe-O-M(H}_2\text{O)}_5]^{(n-3/2+)} + \text{H}_3\text{O}^+$ (McBride, 1994), where sorption onto manganese occurs in a similar fashion.

SP-fine might also have a greater sorption capacity because of prior milling at the ceramic factory Gresco & Grés, which increases the specific surface area (and improves the clay properties for use in ceramics).

4.5.2. Behaviour of other metal analytes

Since the preliminary study suggested a possible release of other metals as a result of sorption, and because XRF chemical analysis indicated the presence of other heavy metals in the kaolinite samples K-fine and SP-fine, it is important to consider how zinc sorption may affect the concentrations of other heavy metals present in solution. Nickel, copper, arsenic, cadmium and lead were concomitantly measured and referred to collectively as “other heavy metals" (Fig. 4.5.3.). Both standards and initial-concentration samples contain equally low levels of concomitantly analysed heavy metals (Fig. 4.5.3.) which can serve as baseline concentrations that must originate from contamination or interference in ICP-MS, since nothing apart from DI water and $ZnCl_2$ was added to these treatments. Both K-fine and SP-fine release a significant amount of heavy metals, but it only represents 1.65% and 0.76% of the amount of zinc they sorbed respectively. The heavy metal release by the natural fine fraction of KGa-1b (K-fine) is almost solely Ni. XRF analysis has shown a high content of copper in KGa-1b (25.2 ppm; Appendix B.2.1), but this is not released here.

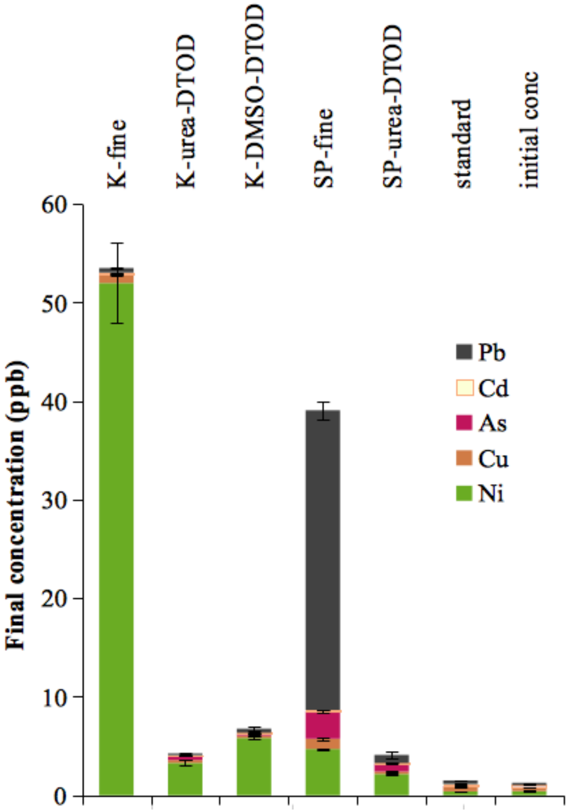

Figure 4.5.3. Average final concentration of all other heavy metals (excl. Zn) concomitantly measured in supernatant solutions of clay-treated samples, standards, and the initial concentration in sorption set 2. Error bars represent standard errors of the mean.

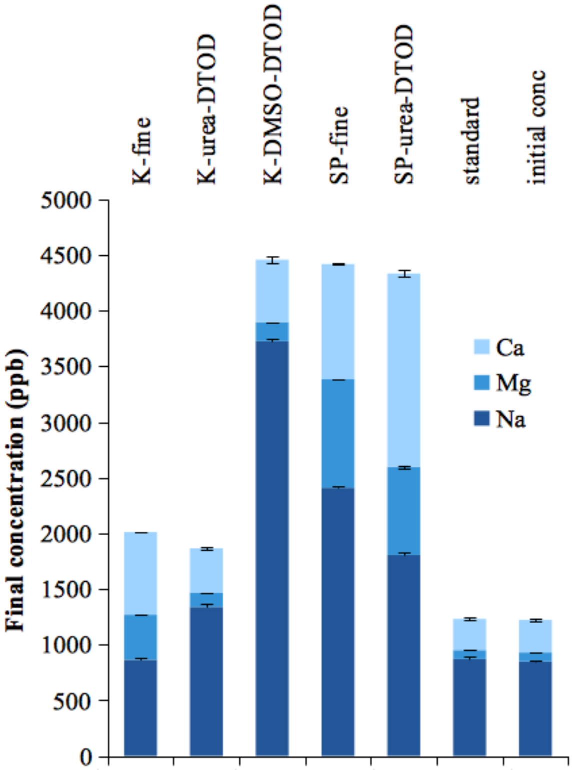

Figure 4.5.4. Average final concentration of the light metals analysed in supernatant solutions of clay-treated samples, standards, and the initial concentration in sorption set 2. Error bars represent standard errors of the mean.

The fine-fraction of São Pedro (SP-fine) releases lower overall concentrations, but of lead and arsenic, which is perhaps more worrisome. Their presence in SP-fine was also determined by XRF (see Fig. 3.5.3). Nickel release by SP-fine is very low despite comparable contents of nickel found by XRF for both K-fine (17.9 ppm) and SP-fine (16.1 ppm) (Fig. 3.5.3 and Appendix B.2.1), meaning nickel in SP-fine is either more strongly bound within the structure and/or SP-fine exhibits a greater number of sorption sites. Compared to arsenic content in SP-fine observed in XRF however, nickel content in SP-fine was lower but released in greater amounts than arsenic (Fig. 3.5.3). This may be attributed to the fact that nickel does not easily form insoluble precipitates (McLean and Bledsoe, 1992). Additionally, nickel is more attracted to Mn-oxides than Fe-oxides (Johnston, 2005), which are present at lower quantities in both samples. In fact, manganese is not mentioned at all of the chemical analyses of the Baseline studies (Appendix B.2.1).

Upon modification of both parent materials, the metal release decreases substantially, during this sorption study that is – the same amount of metals or more were probably released into the washing solvents (isopropanol and water) during the modification steps. The results suggest that the concentrations of other heavy metals are not a simple function of the zinc sorption obtained by each clay sample, but primarily the amount of processing involved in the sample preparation. Both natural fine fractions release considerable amounts of heavy metals, while in the grafted samples these may have been washed off in the intercalation and rinsing steps.

The concentrations of calcium, magnesium or sodium, which may be present as compensating cations, are not linearly related to the amount of zinc sorbed either (Fig. 4.5.4). Nonetheless, the samples that are more effective (K-DMSO-DTOD, SP-fine, and SP-urea-DTOD) do release higher summative concentrations of these light metals (Fig. 4.5.4), which may be indicative of the process of pH-independent sorption.

Release of chromium, manganese and iron are very low in all the KGa-1b samples, but the natural fine fraction of sample São Pedro (SP-fine) released significantly larger amounts of each (Fig. 4.5.5). The high iron concentration measured in SP-fine only indicates that it is easily released. Therefore the iron originally on SP-urea-DTOD must have been washed off during its preparation such that its concentration in the supernatant solutions is drastically reduced. Significantly higher amounts of chromium, manganese and iron are released by the natural fraction of sample São Pedro (SP-fine). While chromium and iron release are not so pronounced in the thio-derivative SP-urea-DTOD, this modified version does still release high amounts of manganese. Manganese concentrations in the São Pedro samples are lower than iron, as in the XRF chemical analysis (Fig. 3.5.2), and seems to be less easily washed off by the processing of SP-urea-DTOD.

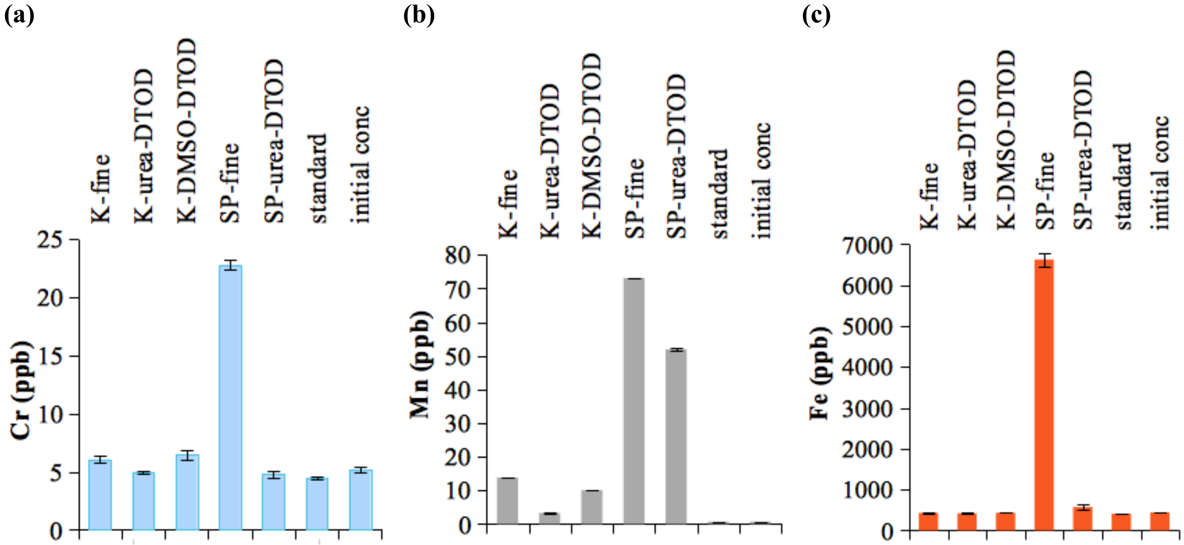

Figure 4.5.5. Average final **(a)** chromium, **(b)** manganese, and **(c)** iron concentrations measured in supernatant solutions of clay-treated samples, standards, and the initial concentration in sample set 2. Values are given in terms of ppb adjusted for the clay concentration. Error bars represent standard errors of the mean.

In general the results suggest that sample São Pedro contains many more elements initially sorbed on its surface, which are released upon sorption of zinc. Presence of fewer of these sorbed species on the natural fraction of KGa-1b explains its lower inherent sorption capacity and much lower release of “other metals”. Furthermore, the rather high amount of e.g. chromium released by SP-fine while much less is released by the processed SP-urea-DTOD, suggests that this species is rather loosely bound to the surface and easily lost in the processing steps to obtain the thio-grafted sample. This interpretation is also supported by the conclusion of Zachara *et al*. (1988) that chromate is weakly bound to kaolinite at varying sorbate and sorbent concentrations and the same might be true for iron, lead and arsenic in the case of SP-fine. Manganese, on the other hand, is also released after zinc sorption with the grafted SP-urea-DTOD, suggesting processing alone was not sufficient to release all manganese from this sample.

4.5.3. Role of pH

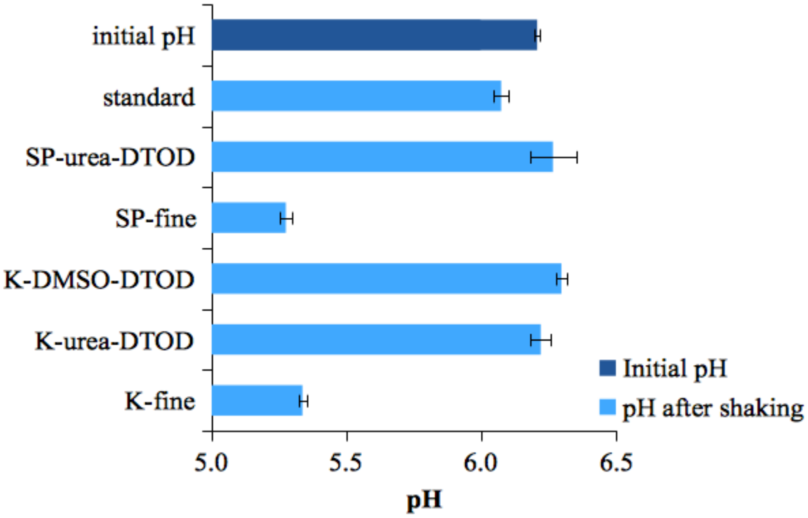

Figure 4.5.6. The pH values measured in sample set 2 after 24 hours of shaking (light blue) compared to the initial pH (dark blue). Error bars represent standard errors of the mean.

Because isomorphic substitutions on kaolinite are low, sorption sites on natural fine fractions of clay would be expected to be primarily pH-dependent, existing on edges where Si-OH and Al-OH groups are sensitive to protonation/deprotonation (Koteja and Matusik, 2015). Indeed, lowest post-sorption pH levels compared to the initial value were observed for both natural fine fractions (K-fine and SP-fine; Fig. 4.5.6), suggesting zinc and other metal species were adsorbed onto deprotonated edge sites. This involves a release of H^+ ions in solution, decreasing the pH, which in turn affects the sorption capacity of the clay. It seems that the other well-sorbing thio-kaolinite samples, SP-urea-DTOD and K-DMSO-DTOD, tend to bring about less of a decrease in pH (Fig. 4.5.6), which suggests that pH dependent sorption was not as pronounced in these treatments and their higher sorption efficiency can be attributed to increased surface area and chelation by the grafted DTOD compounds.

Wang *et al*. (2011) determined that lead sorption onto kaolinite occurs primarily as pH-dependent complexation where an increase in hydrogen ions decreases the formation of metal hydroxides formed on the clay surface. The lower pH in SP-fine in combination with competition by zinc may have played a role in the high lead levels measured in these supernatant solutions.

4.5.4. Qualitative assessment

Flocculation and settling of suspended particles in wastewater is important for its effective treatment and, depending on the individual treatment plant, involves any combination of the following parameters: the settling rate, the sludge volume index (volume of sediment), the fraction of solids that settles, turbidity of the supernatant, pollutant removal, and water recovery (Lee *et al*., 2014). After the 24-hour shaking period some of the suspensions had produced foam, namely SP-fine, SP-urea-DTOD, and K-DMSO-DTOD, which persisted for more than an hour in the two SP samples. The rate of sedimentation was also assessed qualitatively, observing fastest sedimentation in K-urea-DTOD, followed by SP-urea-DTOD > K-DMSO-DTOD > K-fine ≥ SP-fine. Sorption is known to affect clay particles' electrostatic properties and subsequently their coagulation and settling rate (Scheidegger and Sparks, 1996). Here the three samples that removed most zinc exhibited foam, but the settling rates do not correlate so well with the clays' performance – the fine fractions both remained in suspension during the observation time. The settling rate seems to be more related to the thio-functionalisation. The more granular samples, derived from urea-precursors and highly loaded with DTOD, sedimented most quickly, followed by the other thio-modified samples. Hence, the thio-functionalisation seems to improve the flocculation and settling qualities of their respective parent materials.

4.6. Results and discussion of sorption set 3 – Wastewater system experiment

4.6.1. Zinc sorption

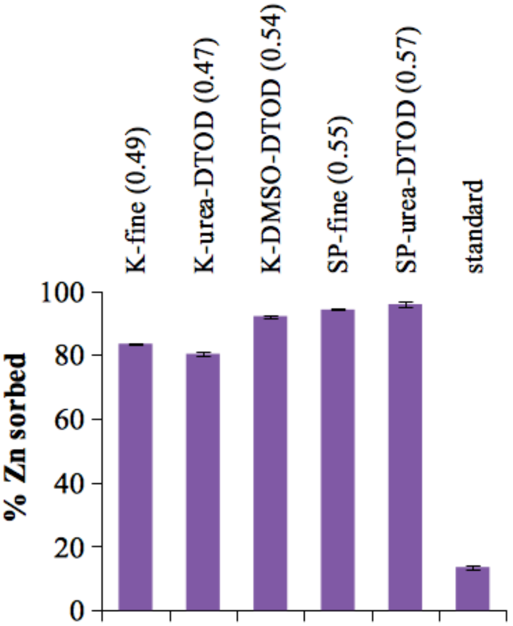

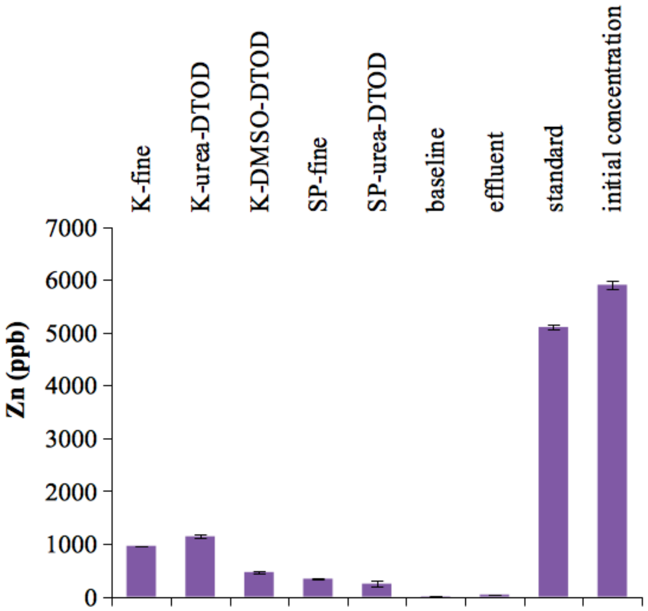

Figure 4.6.1. Average % zinc sorption by natural fine fractions and DTOD-grafted samples of KGa-1b (K) and sample São Pedro (SP) in sorption set 3. Numbers in parentheses give the amount of zinc sorbed in mg/g clay. Error bars represent standard errors of the mean.

Figure 4.6.2. Average zinc concentration measured in supernatant solutions of sorption set 3 including clay-treated samples and standards, as well as the baseline concentration (unspiked raw sewage), the effluent at the WWTP, and the initial concentration. Values are given in terms of ppb adjusted for the clay concentration. Error bars represent standard errors of the mean.

Consistently high removal efficiencies were observed across the board, most notably an increased loading from 0.32 mg to 0.49 mg per gram clay of K-fine, and from 0.22 mg to 0.47 mg per gram clay of K-urea-DTOD (Fig. 4.6.1). The average sorption observed in the standard treatment, containing spiked wastewater only subject to the same procedures as the clay-treatments, is significant (13.5%; Fig. 4.6.1), suggesting precipitation and/or complexation to suspended organics in the wastewater matrix that settled out of solution by centrifugation occurred. This accounts for 0.08 mg of the mg-zinc-per-g-clay sorption rates mentioned that should be subtracted from the calculated amounts given in Fig. 4.6.1. A similar pattern is still observed as in set 2: SP-urea-DTOD performs the best, followed by

SP-fine and K-DMSO-DTOD.

Surprisingly, a higher concentration of zinc was found in effluent water (39.5 ppb) compared to raw sewage (9.0 ppb). Comparison with raw-sewage and effluent data provided by the Robert O. Pickard Environmental Centre shows that the effluent concentration is rather normal and that the baseline concentration measured here is exceptionally low (Appendix E).

A factor to consider is related to the extent of complexation in solution, which seems to be low between zinc and many anions in solution so that it is more likely to sorb and settle out of solution in an insoluble form. In fact, Puls and Bohn (1988) report that zinc sorption onto kaolinite is enhanced in the presence of Cl^-, ClO_4^-, and SO_4^{2-}, which may have contributed to the consistently increased sorption rates observed here. Other factors will be discussed throughout this section.

4.6.2. Behaviour of other metals

While the release of other heavy metals was somewhat concerning in the simple system, their release in the wastewater system is consistently much lower for both natural fine fractions and rather similar for the thio-modified samples (Fig. 4.6.3). In particular, the lead concentration does not exceed the unspiked raw sewage (baseline) concentration in any of the samples. The discrepancies between the unspiked sewage (baseline) and Zn-spiked sewage (initial concentration) is probably because the latter was diluted with 1% nitric acid, leading to a lead concentration that was hardly detectable. While K-urea-DTOD does not perform as well in zinc sorption, it releases the least amount of other heavy metals – probably due to a combination of prior release in processing and locking in of some of the loosely sorbed species by the high DTOD loading.

Lower overall heavy metal concentrations can be explained by the presence of organic ligands and other sorption sites on a variety of suspended solids already present in the wastewater. This suggests that if a (modified) clay sample preferentially sorbs certain heavy metals – which they often do (Tiller, 1996 cited in Churchman, 2006; McBride, 1994), release or presence of metals that have a lower affinity for the clay sorbent are likely to be taken up by any of the other sorbing materials present.

Arsenic, cadmium, and lead are all present at very low concentrations and all mercury measurements are below the detection limit. Yet, a tendency towards arsenic release from most clay samples, particularly sample SP-urea-DTOD can be observed. Cadmium concentration, which was also detected up to a very low limit (see Table 4.3.2), suggests effective uptake by the thio-modified sample. Lead was mostly below the detection limit though SP-fine still seems to be releasing it.

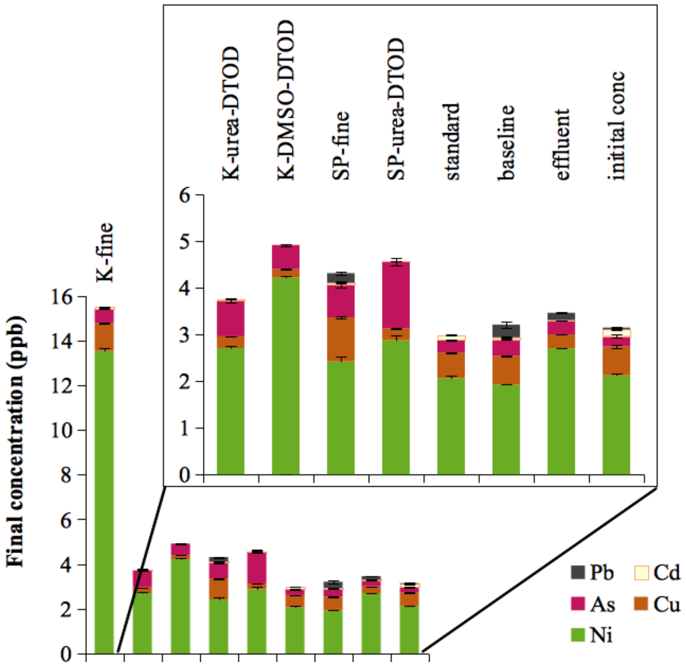

Figure 4.6.3. Average final concentration of all other heavy metals (excl. Zn) measured in supernatant solutions of clay-treated samples, standards, baseline (un-spiked raw sewage), effluent from the WWTP, and the initial concentration in sorption set 3. Overlaid figure is a zoom-in. Error bars represent standard errors of the mean.

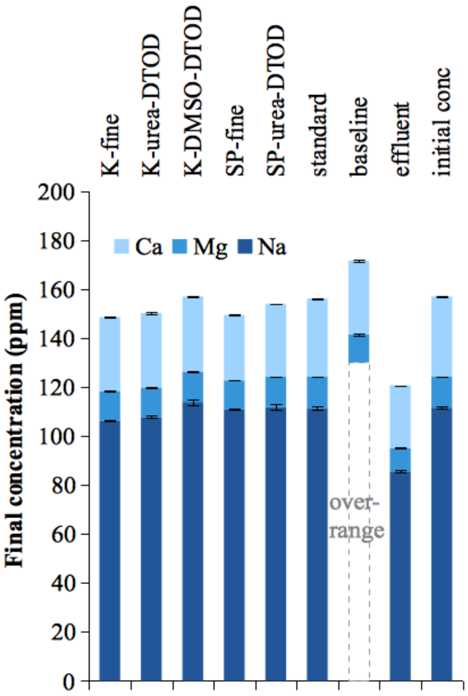

Figure 4.6.4. Average final concentration of the light metals analysed in solutions of clay-treated samples, standards, baseline (un-spiked raw sewage), effluent from the WWTP, and the initial concentration in sorption set 3. Error bars represent standard errors of the mean.

Nickel concentrations are more or less equal in all treatments, apart from a significant release from the natural fine fraction of KGa-1b (K-fine), as in sample set 2 though in much smaller quantities (Fig. 4.6.3). Copper concentrations are so low that it is just below the detection limit for all thio-kaolinite samples, but because the detection limit is not very precise and some copper is probably present, the measurements are included in Figure 4.6.3 anyway. Natural fine fractions display a tendency to release some copper while K-urea-DTOD actually seems to sorb some.

While in set 2 calcium and magnesium are clearly released by clay as a result of zinc sorption, the concentrations of these light metals actually slightly decreases in the wastewater system experiments (sorption in a range of 0.05 to 0.08 mg/g clay for magnesium [4-6% sorption] and 0.17 to 0.55 mg/g clay for calcium; Figure 4.6.4).

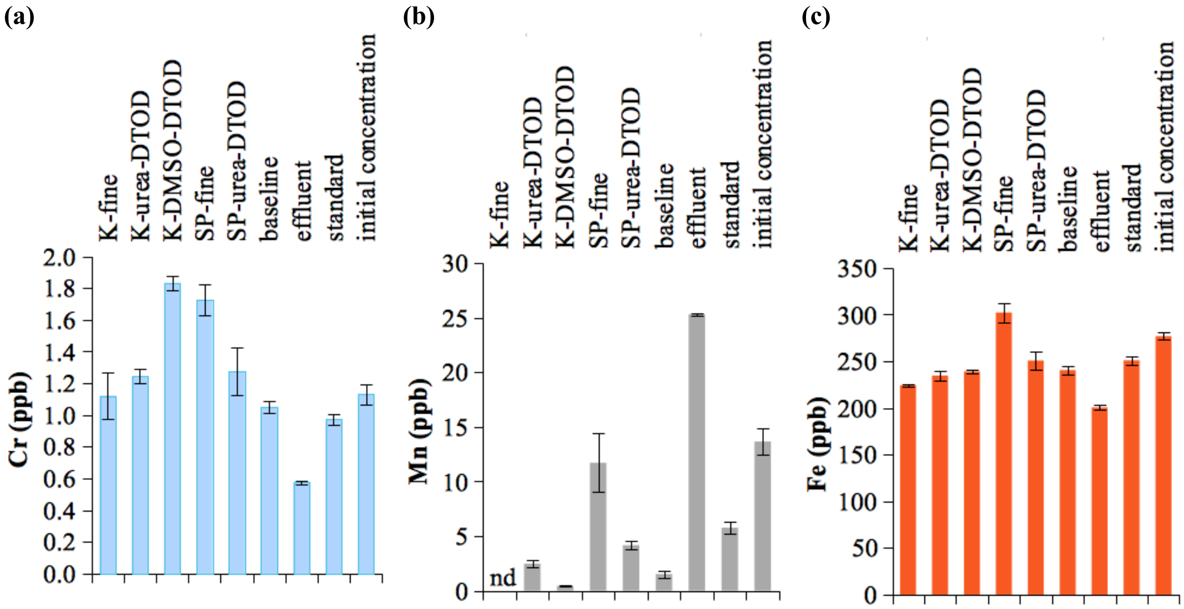

Figure 4.6.5. Average **(a)** chromium, **(b)** manganese, and **(c)** iron concentrations measured in supernatant solutions of clay-treated samples and standards, as well as the baseline concentration (unspiked raw sewage), the effluent at the WWTP, and the initial concentration. Values are given in terms of ppb adjusted for the clay concentration. Error bars represent standard errors of the mean.

Manganese was found in higher quantities in effluent water compared to raw sewage (baseline) concentrations. As for the identical observation for zinc, this can be explained by strong sorption to suspended organics and solids, removing manganese by the filtering step.

The results indicate the potential of some of the clay samples to reduce manganese concentrations, which can give a metallic taste to drinking water (Gautam *et al*., 2015), as all kaolinite samples apart from the natural fine fraction of São Pedro (SP-fine) do a good job at removing manganese (Figure 4.6.5b). The relative differences in manganese concentrations between the treatments with different clay samples is very similar to the pattern observed in sample set 2, where, in line with XRF chemical analysis (Fig. 3.5.2), the SP-fine treatment contains most manganese, followed by SP-urea-DTOD. However, due to interference in the ICP-MS by $^{37}Cl^{18}O$, and $^{23}Na^{32}S$, which is more likely here than in DI water, the manganese results may not be very reliable (McCurdy *et al*., 2006).

A higher iron concentration is found in the fine fraction of São Pedro (SP-fine) compared to the initial concentration of the Zn-spiked wastewater. Indeed chemical analysis of SP-fine also confirms that it contains iron (Fig. 3.5.2). The standard shows that some iron is removed during the shaking and centrifugation process, such that only treatments with K-fine, and to a lesser extent the thio-modified KGa-1b samples (K-urea-DTOD and K-DMSO-DTOD), led to a measurable uptake of iron during the sorption experiment.

4.6.3. Behaviour of sulfur

Figure 4.6.6a shows that the sulfur concentration was significantly higher in samples treated with a thio-kaolinite sorbent and consistent throughout all other treatments (N.B. these concentrations are even in ppm). Figure 4.6.6b further clarifies this, with the largest release relative to the initial concentration coming from K-DMSO-DTOD, of 10.01 mg sulfur per g clay in solution, followed by K-urea-DTOD and then SP-urea-DTOD. Assuming that the organics loading determined by TGA accurately represents the amount of intercalated and supposedly grafted DTOD and knowing the molecular weight of DTOD (182.3 g/mol), an estimation can be made of the fraction of DTOD released during the sorption experiment. Both in absolute and in relative terms, the modified sample based on the DMSO precursor most easily loses DTOD (Table 4.6.1).

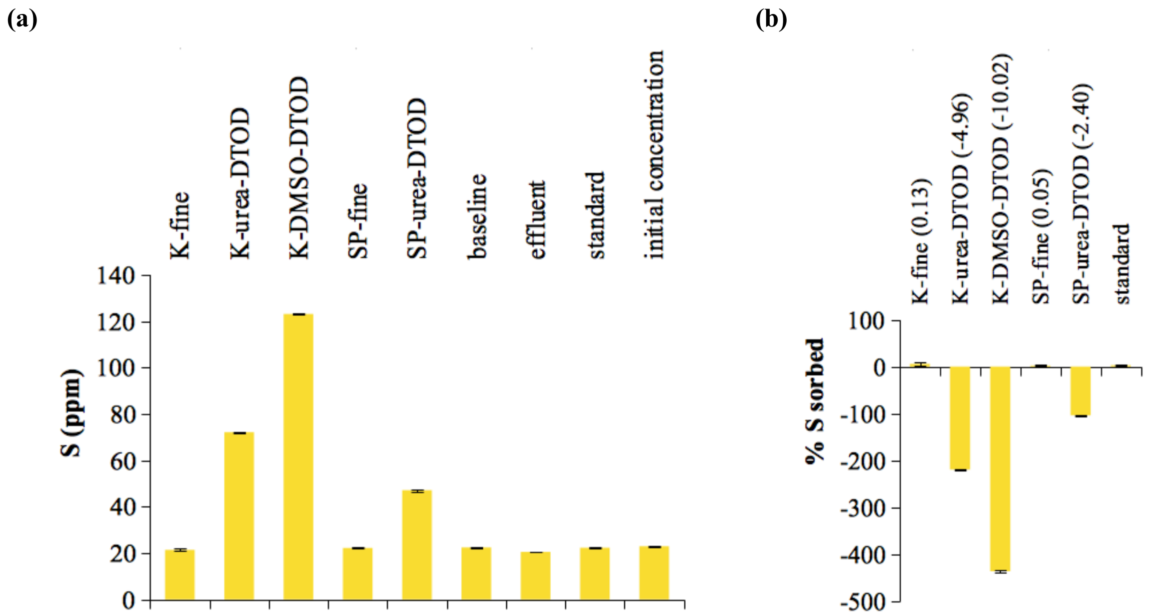

Figure 4.6.6. (a) Average final sulfur concentrations measured in supernatant solutions of clay-treated samples and standards, as well as the baseline concentration (unspiked raw sewage), the effluent at the WWTP, and the initial concentration. Values are given in terms of ppm adjusted for the clay concentration. Error bars represent standard errors of the mean. **(b)** Average % sulfur sorption by clay samples. Numbers in parentheses give the amount of sulfur sorbed in mg/g clay. Negative sorption equals release into solution. Error bars represent standard errors of the mean.

Table 4.6.1. Estimation of the amount of DTOD released in sorption experiment in mg and as a percentage of the amount of DTOD loaded onto the clay sample as determined by TGA.

Sample	DTOD released (mg)	DTOD released (%)
K-urea-DTOD	0.25	0.5
K-DMSO-DTOD	0.5	3.5
SP-urea-DTOD	0.12	1.3

4.6.4. Role of pH

Though the experimental parameters differ between the simple system and wastewater system, the removal obtained in the pH environments observed in the different experiments can give some hints about the likelihood of sorption processes contributing. At higher pH levels precipitation is more likely. The larger the pH change of solution after the sorption experiment, the more sorption is likely to have occurred on the pH-dependent protonation/deprotonation sites. Evidence of the latter is only observed in SP-fine (Fig. 4.6.7).

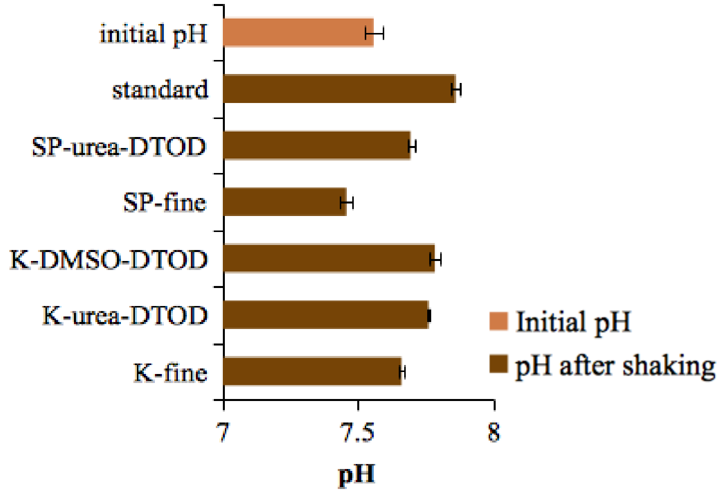

Figure 4.6.7. The pH after 24 hours of shaking compared to the initial pH of sample set 3. Error bars represent standard errors of the mean.

The pH in set 3 varied very little, maintaining a slightly basic character throughout the experiment between pH 7 and 8, normal levels for municipal sewage water. Nonetheless, both natural fine fractions, SP-fine and to a lesser extent K-fine, display a tendency towards a lower pH after shaking compared to the other samples. As in set 2, this can be attributed to kaolinite's low isomorphic substitutions and therefore high proportion of pH-dependent sorption sites.

Gu and Evans (2008) compared empirical and modelling evidence on the contribution of permanently charged sorption sites and pH-dependent sorption sites on kaolinite, demonstrating that in solutions with high ionic strength (0.1M), sorption of zinc onto kaolinite is almost entirely attributed to the pH-dependent sites, while at lower ionic strength (0.01 and 0.001M) sorption mostly occurs on permanent sites until a pH of about 6.2 and 7.5 respectively. Their results also indicate that the ionic strength of a solution has very little to no impact at pH values exceeding 7, like the wastewater system, while at pH between 5 and 6, as in sample set 2, sorption efficiency of kaolinite is clearly higher at low ionic strength (Gu and Evans, 2008). The same was observed for cadmium and nickel, but to a lesser extent for copper and lead, which exhibit a rather constant high sorption efficiency from about pH 5 to 6 onwards (Gu and Evans, 2008).

Dimirkou *et al*. (2002) studied the sorption of zinc onto kaolinite at different pH levels, initial concentrations and two concentrations of KNO_3 electrolyte solution. A general increase in sorption efficiency was observed as pH increases no matter what initial Zn or KNO_3 concentrations, though four out of ten samples exhibit a higher removal efficiency at pH 7 than 8 (Dimirkou *et al*., 2002). According to simulations performed by Koteja and Matusik (2015), the precipitation limit of zinc is at a pH of 7.4 and above, revealing why sorption increases with pH. From the results presented by Metwally *et al*. (1992) it seems that at pH 8, zinc sorption onto calcium-saturated kaolinite is dominated by precipitation as $Zn(OH)_2$, while at pH 7, the zinc potential was higher, suggesting adsorption reactions still occur at this pH. They also found that almost complete immobilization of a zinc-kaolinite system occurs around pH 9 (Metwally *et al*., 1992).

Following from these observations in previous studies, it is likely that pH is a major factor in the enhanced zinc sorption and reduced concentrations of other heavy metals observed in wastewater, which has a slightly basic pH around 7.5 (Fig. 4.6.7). With a higher pH value than in set 2, a greater number of pH-dependent sorption sites may have been available, and due to a high zinc concentration compared to other heavy metals, the consistent sorption increase observed for all clay treatments may be attributed to nucleation and precipitation onto the surface of kaolinite, however with caution because Lumsdon *et al*. (1995) report on the speciation of Zn in solution of LiCl and $LiClO_4$ that $ZnCl^+$ and Zn_2^+ are the dominant species up to a pH of 8.

4.6.5. Qualitative assessment

As in sample set 2, foaming was observed again after the shaking period, but this time only in the SP samples and persisting for a shorter period of time. Qualitative assessment of the sedimentation rate from fast to slow in this study was K-urea-DTOD > SP-urea-DTOD > K-DMSO-DTOD ≥ K-fine > SP-fine, matching quite well with the Zn-sorption efficiency of each sample. Overall the settling speed was an improvement compared to those observed in sample set 2.

4.6. Further discussion of observations made in the different sample sets

As has been briefly mentioned, wastewater contains organic matter onto which some additional precipitation and adsorption most probably occurred. Some studies have shown that metals may sorb better onto colloidal material of certain sizes, such as iron and lead that have a higher affinity for high molecular-weight (MW) complexes while zinc is more likely to be sorbed by low MW particles (Majone *et al*., 1998). Despite the fact that large particles suspended in the raw wastewater were filtered out, the particle sizes considered in such assessments were smaller than the molecular-weight cutoff of the filters used and filtration is therefore not expected to have a major influence on the solution's overall selectivity for certain metals.

Due to the absence of similarly performed sorption studies (i.e. measuring other metal species than zinc or the heavy metal species of interest, as well as performing a study in wastewater), possible explanations for the metal release and sorption patterns shown here have to be drawn from the study of other natural systems, such as landfill leachate or other contaminated soil and water systems. Analysis of the association of different heavy metal species to landfill leachate particles of differing size fractions has shown that most metals are present in the colloidal-size fraction that is dominated by organic matter, with the exception of lead (Gounaris, 1992) and arsenic (Klein and Niessner, 1996), which were found as dissolved species or associated to large inorganic particles. It was also determined for arsenic that it preferentially binds to humic-acid coated kaolinite than to kaolinite on its own (Saada *et al*., 2003). Zinc, on the other hand, has been found in all colloid fractions studied as well as in dissolved state (Gounaris *et al*., 1993).

The study of landfill leachate has also looked into the mobility of metals, and how strongly they are sorbed onto particulate matter, which may give further cues about the release of metal species observed after the zinc sorption of the spiked solutions has equilibrated. Leachate, like wastewater, has a complex and variable composition where a classification based on general variables like TOC, pH, or concentrations of salts can be deceiving (Majone *et al*., 1998). Specifically, the organic components may consists of ligands of widely varying complexity which exhibits significant consequences on the sorption ability of heavy metals contained in the leachate solution (Knox and Jones, 1979; Majone *et al*., 1998). Harmsen (1983), for example, found that iron and lead were sorbed to a greater extent by more complex organics with a high molecular-weight while zinc was associated to lower molecular-weight organics.

Sorption on organic matter occurs by means of proton displacement on acidic functional groups including phenolic, carboxylic, and sulfhydryl ligands (McBride, 2000). Some degree of synergy between organics and inorganic clay is likely because some heavy metals are known to be more attracted by organic matter than clay and vice versa, depending on environmental factors such as the solution pH (Mclaren *et al*., 1981 cited in Churchman *et al*., 2006). Petrović *et al*. (1999) report that zinc-humic acid complexes are increasingly stable at higher pH levels, which leads not only to increased zinc sorption at the higher pH levels tested by stimulating the chelation of zinc cations to humic acid bound to kaolin minerals, but also enhanced the sorption of humic acid to kaolinite by neutralization of the acids' negative charge. This also supports the idea of a potential synergy between inorganic and organic sorbents. The study by Petrovic *et al*. (1999) shows a similar potential for copper and lead, which may elucidate why lower amount of other heavy metals (particularly lead) were released by the natural and modified kaolinite samples (Fig. 4.6.3).

As has been described to some extent in this report, theories exist about the affinity of different metals for sorbent materials (clay surfaces and organic matter) based on their electronegativity and charge-to-radius ratios, but there are many exceptions to the predicted order of preference. Potassium and calcium ions, for instance, are more likely to sorb to soil humus than predicted, suggesting selection according to ionic size may play a role too (McBride, 1994). According to Jackson (1998 cited in Churchman *et al*., 2006), kaolinite sorption follows the divalent-cation-affinity order Pb > Ca > Cu > Mg > Zn > Cd, but this depends on solution concentrations. Also metal affinity for different clay minerals may switch from smectite to illite, for example, as the metal concentration changes (Churchman, 2006).

From the multitude of studies on heavy metals sorption with clay minerals it is clear that they are effective and sorbent materials with a high potential due to their relative abundance and possibility to be functionalised. However, due to the many variables involved and the lack of studies on their application in real wastewater systems it is difficult at this time to determine an optimal design of a wastewater treatment system to remove heavy metals by sorption. Further study on the interplay of factors like pH, organic ligands, competition by other heavy metals, presence of metal oxides, solution ionic strength, etc. would therefore be very useful. Though the aforementioned warning by Majone *et al*. (1998) that classification by a few general parameters can be deceiving should be kept in mind. Having insufficient knowledge of the interaction between the aforementioned factors at this time, it can only be suggested that a powerful and resilient heavy metal sorption system be composed of a high diversity of both inorganic and organic sorbents, so as to limit secondary release of metals and to be able to deal with variabilities in metal concentrations in the input (raw sewage) to the wastewater treatment plant.

4.7. Conclusions

The sorption capacity of the clay samples tested were remarkably different in spiked-DI-water and spiked-wastewater systems, as were the amounts of other heavy metals released. In the wastewater system higher zinc sorption was obtained and consequential release of other heavy metals was suppressed. This can be attributed mainly to the slightly alkaline nature of the wastewater, a natural buffering capacity, and a synergy with organic matter.

Regardless of the system, natural fine fractions released higher amounts of non-target metals, including heavy metals of concern. Such a consequence of sorption must be accounted for with a view on using clay minerals in wastewater treatment.

The results presented here demonstrate the importance of considering the interplay between organic and inorganic components of the system. It is postulated that a successful and adaptable sorption system for the removal of heavy metals on an industrial scale could be created by introducing a larger diversity of sorbent species, including organic matter with various types of ligands. This may also ensure that secondary release (i.e. the release of "other metals" observed in this study as a result of zinc sorption) is minimized. As such, study of sorption onto mixtures of different clay sorbent materials may prove to be useful towards a greater applicability of clay minerals in wastewater remediation strategies. The results further demonstrate that, despite the existence of an extensive knowledge base on sorption phenomena onto clay materials, the contribution of different processes that are involved in the sorption onto natural and modified kaolinite under certain conditions are very complex and the identification of the distinct mechanisms at play is a formidable task. Further studies should determine the relative contribution of the pH versus the species diversity in this phenomenon.

References

Agilent Technologies, Inc. (2009) Comparing collision/reaction cell modes for the measurment of interfered analytes in complex matrices using the Agilent 7700 Series ICP-MS – Technical Overview. Agilent Technologies [online]. Available at: http://www.chem.agilent.com/Library/technicaloverviews/Public/5990-3236EN.pdf [Accessed on 3 July 2015].

Agilent Technologies, Inc. (2010) Collision/reaction cells in ICP-MS – cell design considerations for optimum performance in helium mode with KED. Agilent Technologies [online]. Available at: http://www.queensu.ca/asu/instrumentation/ICP-MS/Collisionreactioncell.pdf [Accessed on 3 July 2015].

Agilent Technologies, Inc. (2010b) Agilent 7700 Series ICP-MS [online]. Available at: http://www.chem.agilent.com/Library/brochures/5990-4025EN.pdf [Accessed on 7 July 2015].

Agilent Technologies, Inc. (2014) Agilent 8800 Triple Quadrupole ICP-MS (brochure). Agilent Technologies [online]. Available at: http://www.chem.agilent.com/Library/brochures/5991-0079EN_8800_ICPQQQ_Brochure.pdf [Accessed on 3 July 2015].

AIST (n.d.) Spectral database for organic compounds SDBS. SDBS information. National Institute of Advanced Industrial Science and Technology [online]. Available at: http://sdbs.db.aist.go.jp/sdbs/cgi-bin/direct_frame_top.cgi. [Accessed 29 June 2015]

Alexandre, M. and Dubois, P. (2000) Polymer-layered silicate nanocomposites: preparation, properties and uses of a new class of materials. *Materials Science and Engineering,* 28, 1-63.

Altaner, S. P., Weiss Jr., C. A. and Kirkpatrick, R. J. (1988) Evidence from 29Si NMR for the structure of mixed-layer illite/smectite clay minerals. *Nature,* 331, 699-702.

Amer, M. W., Khalili, F. I. and Awwad, A. M. (2010) Adsorption of lead, zinc and cadmium ions on polyphosphate-modified kaolinite clay. *Journal of Environmental Chemistry and Ecotoxicology,* 2(1), 1-8.

Anagho, S. G., TchuifonTchuifon, D. R., Ndifor-Angwafor, N. G., NsamiNdi, J., MbadcamKetcha, J., Nchare, M. (2013) Nickel adsorption from aqueous solution onto kaolinite and metakaolinite: kinetic and equilibrium studies. *International Journal of Chemistry,* [04] ISSN 2306-6415.

Appenroth, K.-J. (2010) Definition of “heavy metals” and their role in biological systems. In: Sherameti, I. And Varma, A. eds. *Soil Heavy Metals.* Soil Biology – Volume 19. Springer-Verlag Berlin Heidelberg.

Baddor, I., M., Farhoud, N., Abdel-Magid, I., M., Alshami, S., Ahmad, F. H. and Olabi, A. (2014) Study of car wash wastewater treatment by adsorption. Paper presented to International Conference on Engineering, Information Technology and Science (ICEITS), Kuala Lumpur, Malaysia, 3 December 2014.

Bailey, S. W. (1980) Summary of recommendations of AIPEA nomenclature committee on clay minerals. *American Mineralogist,* 65, 1-7.

Bain, D. C. and Smith, B. F. L. (1994) Chemical analysis. In: Wilson, M. J. ed. *Clay Mineralogy: Spectroscopic and Chemical Determinative Methods.* London: Chapman & Hall.

Baron, A., Bernard, A., Deloye, F. X., Louvrier, J., Millet, J., Sierra, R., Struillou, R. and Voïnovitch, I. A., (1971) *L'analyse Minéralogique des Sols Argileux.* Paris: Éditions Eyrolles

Becerro, A. I., Mantovani, M. and Escudero, A. (2009) Mineralogical stability of phyllosilicates in hyperalkaline fluids: influence of layer nature, octahedral occupation and presence of tetrahedral Al. *American Mineralogist,* 94, 1187-1197.

Bergaya, F., Lagaly, G. and Vayer, M. (2006) Cation and anion exchange. In: Bergaya, F., Theng, B. K. G. and Lagaly, G. eds. *Handbook of Clay Science.* Developments in Clay Science, vol. 1. Elsevier Ltd.

Bhattacharyya, K. G. and Gupta, S. S. (2008) Adsorption of a few heavy metals on natural and modified kaolinite and montmorillonite: A review. *Advances in Colloid and Interface Science*, 140, 114-131.

Bian, R., Cheng, K., Zheng, J., Liu, X., Liu, Y., Li, Z., Li, L., Smith, P., Pan, G.; Crowley, D., Zheng, J., Zhang, X., Zhang, L. and Hussain, Q. (2015) Does metal pollution matter with C retention by rice soil? *Scientific Reports,* 5, 13233.

Bish, D. L. and Post, J. E. (1989) *Reviews in Mineralogy, vol. 20 – Modern Powder Diffraction.* Washington D. C.: Mineralogical Society of America.

Bishop, J. L., Lane, M. D., Brown, A. J., Hiroi, T., Swayze, G. A. and Lin, J.-F. (2013) Spectral properties of Ca-, Mg- and Fe- bearing carbonates. *44th Lunar and Planetary Science Conference. (Texas, United States, 18-22 March)*

Bolland, M. D. A., Posner, A. M. and Quirk, G. P. (1980) PH-independent and pH dependent surface charges on kaolinite. *Clays and Clay Minerals.,* 28, 412-418.

Borden, D. and Giese, R. F. (2001) Baseline Studies of the Clay Minerals Society Source Clays: Cation exchange capacity measurements by the ammonia-electrode method. *Clays and Clay Minerals,* 49(5), 444-445.

Brady, N. C. and Weil, R. R. (2002) *The Nature and Properties of Soils.* 13th ed. Upper Saddle River, New Jersey: Prentice Hall.

Brindley, G. W. and Robinson, K. (1946) The structure of kaolinite. *Mineralogical Magazine* , 27, 242-253.

Brindley, G. W. and Brown, G. (1980) Crystal Structures of Clay Minerals and their X-ray Identification. London: Mineralogical Society.

Carballa, M., Omil, F., Lema, J. M., Llompart, M., Garcia-Jares, C., Rodriguez, I, Gomez, M., Ternes, T. (2004) Behavior of pharmaceuticals, cosmetics and hormones in sewage treatment plant. Water Resources, 38, 2918-2926.

Cheng, H., Liu, Q., Liu, J., Sun, B., Kang, Y. and Frost, R. L. (2014) TG-MS-FTIR (evolved gas analysis) of kaolinite-urea intercalation complex. *Journal of Thermal Analysis and Calorimetry, 116, 195-203.*

Chipera, S. J. and Bish, D. L. (2001) Baseline studies of the Clay Minerals Society source clays: Powder X-ray diffraction analyses. *Clays and Clay Minerals,* 49(5), 398-409.

Churchman, G. J. (1990) Relevance of different intercalation tests for distinguishing halloysite from kaolinite in soils. *Clays and Clay Minerals,* 38(6), 591-599.

Churchman, G. J., Gates, W. P., Theng, B. K. G. and Yuan, G. (2006) Clays and clay minerals for pollution control. In: Bergaya, F., Theng, B. K. G. and Lagaly, G. eds. *Handbook of Clay Science.* Developments in Clay Science, Vol. 1. Elsevier Ltd.

Coles, C. A. and Yong, R. N. (2002) Aspects of kaolinite characterization and retention of Pb and Cd. *Applied Clay Science,* 22, 39-45.

Collins, D. R. and Catlow, R. A. (1991) Energy-minimized hydrogen-atom positions of kaolinite. *Acta Crystallographica Section B,* 47(5), 678-682.

Comber, S. D. W. and Gunn, A. M. (1996) Heavy metals entering sewage-treatment works from domestic sources. *Journal of the Chartered Institution of Water and Environmental Management,* 10, 137-142.

Comans, R. N. J. and Middelburg, J. J. (1987) Sorption of trace metals on calcite: applicability of the surface precipitation model. *Geochimica et Cosmochimica Acta,* 51, 2287-2591.

Conte, P., Spaccini, R., Piccolo, A. (2004) State of the art of CPMAS 13C-NMR spectroscopy applied to natural organic matter. *Progress in Nuclear Magnetic Resonance Spectroscopy,* 44, 215-223.

Costa, C., Reis, A. P., Ferreira da Silva, E., Rocha, F., Patinha, C., Dias, A. C., Sequeira, C. and Terroso, D. (2011) Assessing the control exerted by soil mineralogy in the fixation of potentially harmful elements in the urban soils of Lisbon, Portugal. Environmental Earth Science, 65(4) 1133-1145.

Costanzo, P. M. (2001) Baseline Studies of the Clay Minerals Society Source Clays: introduction. *Clays and Clay Minerals,* 49(5), 372-373.

Cruz, M., Jacobs, H. and Fripiat, J. J. (1973) The nature of the interlayer bonding in kaolin minerals. *Proceedings of the International Clay Conference, Madrid, 29-30 June 1972*. Madrid: Division de Ciencias C.S.I.C., pp 35-46.

da Silva, P. A. B., de Souza, G. C. S., Leotério, D. M. da S., Belian, M. F., Silva, W. E., Paim, A. P. S., Lavorante, A. F. (2015) Synthesis and characterization of functionalized silica with 3,6-dithia-1,8-octanediol for the preconcentration and determination of lead in milk employing multicommuted flow system coupled to FAAS. *Journal of Food Composition and Analysis,* 40, 177-184.

Detellier, C. and Schoonheydt, R. A. (2014) From platy kaolinite to nanorolls. *Elements,* 10, 201-206.

Dimirkou, A., Ioannou, A., Papadopoulos, P. and Paschalidou, C. (2002) Zinc sorption by kaolinite: influence of pH, electrolyte, and initial Zn concentrations with simultaneous release of Mg, Ca, Mn, and Cu ions. Communication*s in soil science and plant analysis,* 33 (15-18), 2917-2934.

Dubrawski, J. V., Channon, A.-L. And Warne, S. St. J. (1989) Ecaminationof the siderite-magnesite mineral series by Fourier transform infrared spectroscopy. *American Mineralogist,* 74, 187-190.

Duer, M. J. (2004) *Introduction to Solid-State NMR Spectroscopy.* Oxford: Blackwell Publishing Ltd.

Ellwood, B. B., Burkart, B., Rajeshwar, K., Darwin, R. L., Neeley, R. A., McCall, A. B., Long, G. J., Buhl, M. L. and Hickcox, G. W. (1989) Are the iron carbonate minerals, ankerite and ferroan dolomite, like siderite, important in paleomagnetism? *Journal of Geophysical Research,* 94(B6), 7321-7331.

Enoh, B. S. and Christopher, W. (2015) Adsorption of metal ions from carwash wastewater by phosphoric acid modified clay: kinetics and thermodynamic studies. *Chemistry and Materials Research,* 7(4).

Erickson, A. J., Weiss, P. T. and Guilliver, J. S. (2013) *Optimizing Stormwater Treatment Practices: A Handbook of Assessment and Maintenance.* New York: Springer-Verlag.

Eslinger, E. and Pevear, D. (1988) Clay minerals for Petroleum Geologists and Engineers. SEPM Short Course Notes, Vol. 22. Tulsa: Society of Economic Paleontologists and Mineralogists.

European Commission (2002) Heavy metals in waste – final report. *European Commisiosn DG ENV. E3* [online]. Available at: http://ec.europa.eu/environment/waste/studies/pdf/heavy_metalsreport.pdf [Accessed on 1 August 2015].

Farley, K. J., Dzombak, D. A. and Morel, F. M. M. (1985) A surface precipitation model for the sorption of cations on metal oxides. *Journal of Colloid and Interface Science,* 106(1), 226-242.

Fisheries Act (2010) Wastewater systems effluent regulations. 144 (12) {online]. Available at: http://www.gazette.gc.ca/rp-pr/p1/2010/2010-03-20/htmL/reg1-eng.htmL [Accessed on 21 July 2015].

Flora, S. J. S. and Pachauri, V. (2010) Chelation in metal intoxication. *International Journal of Environmental Research and Public Health,* 7(7), 2745-2788.

Frost, R. L., Tran, T. H., Kristof, J. (1997) The structure of an intercalated ordered kaolinite – a Raman microscopy study. *Clay minerals,* 32, 587-596.

Frost, R. L., Kristof, J., Paroz, G. N. and Kloprogge, J. T. (1998) Molecular structure of dimethyl sulfoxide intercalated kaolinites. *Journal of Physical Chemistry B,* 102, 8519-8532.

Frost, R. L., Makó, É., Kristóf, J., Horváth, E. and Kloprogge, T. (2001) Mechanochemical treatment of kaolinite. *Journal of Colloid and Interface Science,* 239, 458-466.

Fultz, B. and Howe, J. (2013) T*ransmission Electron Microscopy and Diffractometry of Materials*. Graduate Texts in Physics. Berlin Heidelberg: Springer-Verlag.

Galhano, C., Rocha, F. and Gomes, C. (1999) Geostatistical analysis of the influence of textural, mineralogical and geochemical parameters on the geotechnical behaviour of the 'Argilas de Aveiro' Formation (Portugal). Clay Minerals, 34, 109-116.

Gardolinski, J. E. F. C. and Lagaly, G. (2005) Grafted organic derivatives of kaolinite: II. Intercalation of primary n-alkylamines and delamination. *Clay Minerals,* 40, 547-556.

Gautam, R. K., Sharma, S. K., Mahiya, S. and Chattopadhyaya, M. C. (2015) Contamination of heavy metals in aquatic media: transport, toxicity and technologies for remediation. In: Sharma, K. S. ed. *Heavy Metals in Water: Presence, Removal and Safety.* Cambridge: The Royal Society of Chemistry.

Giese, Jr., R. F. (1973) Interlayer bonding in kaolinite, dickite and nactrite. *Clays and Clay Minerals,* 21, 145-149.

Giese, Jr., R. F. and Datta, P. (1973) Hydroxyl orientation in kaolinite, dickite and nacrite. *American Mineralogist,* 58, 471-479.

Giese, R. F. (1978) The electrostatic interlayer forces of layer structure minerals. *Clays and Clay Minerals,* 26(1), 51-57.

Giese, Jr., R. F. (1988) Kaolin minerals: structure and stabilities. In: Bailey, S. W. ed. Hydrous Phyllosilicates (exclusive of micas). Reviews in Mineralogy – volume 19. Chelsea, MI: Mineralogical Society of America.

Gonzalez Garcia, F., Ruiz Abrio, M. T. and Gonzalez Rodriguez, M. (1991) Effects of dry grinding on two kaolins of different degrees of crystallinity. *Clay Minerals,* 26, 549-565.

Goodman, B. A. and Chudek, J. A. (1994) Nuclear magnetic resonance spectroscopy. In: Wilson, M. J. ed. C*lay mineralogy: spectroscopic and chemical determinative methods*. London: Chapman & Hall.

Gounaris, V. (1992) Characteristics of colloids in landfill leachate. Ph.D. Thesis. Illinois Institute of Technology, Chicago, IL, USA.

Gounaris, V., Anderson, P. R., Holsen, T. M. (1993) Characteristics and environmental significance of colloids in landfill leachate. *Environmental Science and Technology,* 27, 1381-1387.

Gu, X. and Evans, L. J. (2008) Surface complexation modelling of Cd(II), Cu(II), Ni(II), Pb(II) and Zn(II) adsorption onto kaolinite. *Geochimica et Cosmochimica Acta,* 72, 267-276.

Guggenheim, S. and Martin, R. T. (1995) Definition of clay and clay mineral: joint report of the AIPEA nomvenclature and CMS nomenclature committees. *Clays and Clay Minerals,* 43(2), 255-256.

Guggenheim, S. and van Groos, A. F. K. (2001) Baseline Studies of the Clay Minerals Society Source Clays: Thermal analysis. *Clays and Clay Minerals,* 49(5), 433-443.

Guggenheim, S., Adams, J. M., Bain, D. C., Bergaya, F., Brigatti, M. F., Drits, V. A., Formoso, M. L. L., Galán, E., Kogure, T. and Stanjek, H. (2006) Summary of recommendations of nomenclature committees relevant to clay mineralogy: report of the Association Internationale pour l'Étude des Argiles (AIPEA) Nomenclature Committee for 2006. *Clay Minerals,* 41, 863-877.

Harmsen, J. (1983) Identification of organic compounds in leachate from a waste tip. *Water Research,* 17(6), 699-705.

Hayashi, S. and Akiba, E. (1994) Interatomic distances in layered silicates and their intercalation compounds as studied by cross polarization NMR. *Chemical Physics Letters*, 226, 495-500.

Hayashi, S (1995) NMR study of dynamics of dimethyl sulfoxide molecules in kaolinite/dimethyl sulfoxide intercalation compound. *Journal of Physical Chemistry,* 99, 7121-7129.

Hayashi, S. (1997) NMR study of dynamics and evolution of guest molecules in kaolinite/dimethylsulfoxide intercalation compound. *Jounal of Physical Chemistru,* 99, 712-7129.

Health Canada (2012) Triclosan: Chemical Abstracts Service Registry Number 3380-34-5. Environment Canada. Preliminary Assessment.

Hirschmugl, C. (2004) An introduction to infrared spectroscopy for geochemistry and remote sensing. In: King, P. L., Ramsey, M. S. and Swayze, G. A. eds. *Infrared Spectroscopy in Geochemistry, Exploration Geochemistry, and Remote Sensing.* Mineralogical Association of Canada – Short Course Series Volume 33.

Hojati, S. and Landi, A. (2015) Removal of zinc from a metal plating wastewater using an Iranian sepiolite: determination of optimum conditions. *Desalination and Water Treatment,* 53, 2117-2124.

Horváth, E., Kristóf, J. and Frost, R. L. (2010) Vibrational spectroscopy of intercalated kaolinites: Part I. *Applied Spectroscopy Reviews,* 45, 130-147.

IUPAC (1997) *Compendium of Chemical Terminology,* 2nd ed. (the "Gold Book"). Compiled by McNaught, A. D. and Wilkinson, A. Oxford: Blackwell Scientific Publicaitons [online]. Available at: http://goldbook.iupac.org/ [Accessed on 26 July 2015].

Jackson, T. A. (1998) The biogeochemical and ecological significant of interactions between colloidal minerals and trace elements. In: Parker, A. and Rae, J. E. eds. *Environmental Interactions of Clays.* Springer.

Janssens, K. (2004) X-ray based methods of analysis. In: Janssens and Van Grieken (eds.) *Comprehensive Analytical Chemistry XLII.* Elsevier.

Jenkins, R. (1989) Chapter 2 – Instrumentation. In: Bish and Post (eds.) *Modern Powder Diffraction.* Washington, D.C.: Mineralogical Society of America.

Ji, J., G, Y., Balsam, W., Damuth, J., Chen, J. (2009) Rapid identification of dolomite using a Fourier Transform Infrared Spectrophotometer (FTIR): A fast method for identifying Heinrich events in IODP Site U1308. *Marine Geology,* 258, 60-68.

Jiang, J.-Q., Zeng, Z. and Pearce, P. (2004) Preparation and use of modified clay coagulants for wastewater treatment. *Water, Air, and Soil Pollution,* 158, 53-65.

Johnston, C. T., Sposito, G., Bocian, D. F. and Birge, R. R. (1984) Vibrational spectroscopic study of the interlamellar kaolinite-dimethyl sulfoxide complex. *Journal of Physical Chemistry,* 88, 5959-5964.

Johnston, A. E. (2005) Trace elements in soil: status and management. In: *Essential trace elements for plants, animals and humans.* Seminar proceedings. NJF Seminar no. 370. Reykjavík, Iceland [15-17 August].

Koteja, A. and Matusik, J. (2015) Di- and triethanolamine grafted kaolinites of different structural order as adsorbents of heavy metals. *Journal of Colloid and Interface Science,* 455, 83-92.

Kim, C. G., Lee, H. J., Kim, Y. M. and Jiang, J. Q. (2013) Evaluation of the modified clays in the treatment of car-washing wastewater. *Asian Journal of Chemistry,* 25(10), 5851-5855.

King, P. L., Ramsey, M. S., McMillan, P. F. and Swayze, G. (2004) Laboratory Fourier Transform infrared spectroscopy methods for geologic samples. In: King, P. L., Ramsey, M. S. and Swayze, G. A. eds. *Infrared Spectroscopy in Geochemistry, Exploration Geochemistry, and Remote Sensing.* Mineralogical Association of Canada – Short Course Series Volume 33.

Kirkpatrick, R. J. (1988) MAS NMR spectroscopy of minerals and glasses. In: Hawthorne, F. C. (ed.) *Reviews in Mineralogy, vol. 18 – Spectroscopic methods in mineralogy and geology.* Washington, D.C.: Mineralogical Society of America.

Klein, T. and Niessner, R. (1996) Characterization of heavy metal containing hydrocolloids from seepage water of a municipal waste disposal with ultrafiltration and flow field-flow fractionation. Vom Wasser, 87, 373-385.

Knox, K. and Jones, P. H. (1979) Complexation characteristics of sanitary landfill leachates. *Water Research,* 13, 839-846.

Kogel, J. E. and Lewis, S. A. (2001) Baseline studies of the Clay Minerals Society Source Clays: Chemical analysis by inductively coupled plasma-mass spectroscopy (ICP-MS). *Clays and Clay Minerals,* 49(5), 387-392.

Kurniawan, A., Ismadji, S., Soetaredjo, F. E. and Qyucitra, A. (2015) Natural clays/clay minerals and modified forms for heavy metals removal. In: Sharma, S. K. ed. *Heavy Metals in Water: Presence, Removal and Safety.* Cambridge: The Royal Society of Chemistry.

Langier-Kuźniarowa, A. (2002) Thermal analysis of organo-clay complexes. In: Yariv, S. ed. *Organo-Clay Complexes and Interactions.* New York: Marcel Dekker, Inc.

Le Chatelier, H. (1887) De l'action de la chaleur sur les argiles. *Société française de minéralogie et de cristallographie,* 10, 204-211.

Lecomte-Nana, G., Bonnet, J.-P., Soro, N. (2013) Influence of iron on the occurrence of primary mullite in kaolin based materials: A semi-quantitative X-ray diffraction study. *Journal of the European Ceramic Society,* 33, 669-677.

Ledoux, R. L. and White, J. L. (1966) Infrared studies of hydrogen bonding interaction between kaolinite surfaces and intercalated potassium acetate, hydrazine, formamide, and urea. *Journal of Colloid and Interface Science,* 21, 127-152.

Lee, C. S., Robinson, J. and Chong, M. F. (2014) A review on application of flocculants in wastewater treatment. *Process Safety and Environmental Protection,* 92, 489-508.

Letaief, S. and Detellier, C. (2005) Reactivity of kaolinite in ionic liquids: preparation and characterization of a 1-ethyl pyridinium chloride-kaolinite intercalate. *Journal of Material Chemistry,* 15, 4734-4740.

Letaief, S., Elbokl, T. A. and Detellier, C. (2006) Reactivity of ionic liquids with kaolinite: Melt intersalation of ethyl pyridinium chloride in an urea-kaolinite pre-intercalate. *Journal of Colloid and Interface Science,* 302, 254-258.

Letaief, S., Tonlé, K., Diaco, T., Detellier, C. (2008) Nanohybrid materials from interlayer functionalization of kaolinite. Application to the electrochemical preconcentration of cyanide. *Applied Clay Science,* 42, 95.

Letaief, S. and Detellier, C. (2011) Application of thermal analysis for the characterisation of intercalated and grafted organo-kaolinite nanohybrid materials. *Journal of Thermal Analysis and Calorimetry,* 104, 831-839.

Letaief, S., Leclercq, J., Liu, Y. and Detellier, C. (2011) Single kaolinite nanometer layers prepared by an in situ polymerization-exfoliation process in the presence of ionic liquids. *Langmuir,* 27, 15248-15254.

Levey, M. (1959) Clay and its technology in ancient mesopotamia. *Centaurus,* 6(2), 149-156.

Lumsdon, D. G., Evans, L. J. and Bolton, K. A. (1995) The influence of pH and chloride on the retention of cadmium, lead, mercury and zinc by soils. *Journal of Soil Contamination,* 4(2), 137-150.

Madejová, J. and Komadel, P. (2001) Baseline Studies of the Clay Minerals Society Source Clays: Infrared methods. *Clays and Clay Minerals,* 49(5), 410-432.

Madejova, J., Balan, E. and Petit, S. (2011) Application of vibrational spectroscopy to the characterization of phyllosilicates and other inductrial minerals. EMU Notes in Mineralogy. 9, 171-226.

Magi, M., Lippmaa, E., Samoson, A., Engelhardt, G. and Grimmer, A. R. (1984) Solid-state high-resolution silicon-29 chemical shifts in silicates. *Journal of Physical Chemistry*, 88, 1518-1522.

Mahdavi, F., Rashid, S. A. and Yusop, M. K. (2014) Intercalation of urea into kaolinite for preparation of controlled release fertilizer. *Chemical Industry & Chemical Engineering Quaterly,* 20(2), 207-213.

Majone, M., Papini, M. P., Rolle, E. (1998) Influence of metal speciation in landfill leachates on kaolinite sorption. *Water Research,* 32(3), 882-890.

Matusik, J., Klapyta, Z. and Olejniczak, Z. (2013) NMR and IR study of kaolinite intercalation compounds with benzylalkylammonium chlorides. *Applied Clay Science,* 83-84, 426-432.

Mbaye, A., Diop, C. A. K., Miehe-Brendle, J/, Senecz, F. and Maury, F. (2014) Characterization of natural and chemically modified kaolinite from Mako (Senegal) to remove lead from aqueous solutions. *Clay Minerals,* 49, 527-539.

McBride, M. B. (1994) *Environmental Chemistry of Soils*. New York: Oxford University Press.

McBride, M. B. (2000) Chemisorption and precipitation reactions. In: *Handbook of Soil Science.* Summer, M. E. ed. CRC Press LLC.

McCurdy, E., Woods, G. and Potter, D. (2006) Unmatched removal of spectral interferences in ICP-MS using the Agilent octopole reaction system with helium collision mode. *Agilent Technologies.*

Mackenzie, R. C. (1991) Geosciences in thermal analysis development. In: Smykatz-Kloss, W. and Warne, S. S. J. eds. *Lecture Notes in Earth Sciences*, 38, Thermal analysis in the Geosciences. Springer-Verlag.

McLean, J. E., Bledsoe, B. E. (1992) Behavior of metals in soils. EPA, Ground water issue [online]. Available at: http://www.epa.gov/superfund/remedytech/tsp/download/issue14.pdf [Accessed 26 September 2015].

McMillan, P. F. and Hofmeister, A. (1988) Infrared and Raman spectroscopy. *Reviews in Mineralogy and Geochemistry,* 18, 99-159.

Mercier, L. and Detellier, C. (1995) Preparation characterization and applications as heavy metals sorbents of covalently grafted thiol functionalities on the interlamellar surface of montmorillonite. *Environmental Science and Technology,* 29, 1318-1323.

Mermut, A. R. and Cano, A. F. (2001) Baseline studies of the Clay Minerals Society Source Clays: chemical analyses of major elements. *Clays and Clay Minerals,* 49(5), 381-386.

Metwally, A. L., Mashhady, A. S., Falatah, A. M. and Reda, M. (1992) Effect of pH on zinc adsorption and solubility in suspensions of different clays and soils. *Zeitschrift für Pflanzenernährung und Bodemkunde,* 156(2), 131-135.

Mielenz, R. C., Schieltz, N. C. and King, M. E. (1953) Thermogravimetric analysis of clay and clay-like minerals. *Second National Conference on Clays and Clay Minerals,* 2, 285-314.

Millberg, L. S. (n.d.) Ceramic Tile. In: *How Products Are Made – Vol. 1* [online]. Available at: http://www.madehow.com/Volume-1/Ceramic-Tile.htmL [Accessed on 8 August 2015].

Miranda-Trevino, J. C. and Coles, C. A. (2003) Kaolinite properties, structure and influence of metal retention on pH. *Applied Clay Science,* 23, 133-139.

Mitchell, W. G. and Jones, M. M. (1978) Four new chelating agents containing vicinal thioether groups. *Journal of Inorganic and Nuclear Chemistry,* 40, 1957-1961.

Mohanty, K., Das, D., Biswas, M. N. (2006) Preparation and characterization of activated carbons from *Sterculia alata* nutshell by chemical activation with zinc chloride to remove phenol from wastewater. *Adsorption,* 12, 119-132.

Moll, Jr., W. F. (2001) Baseline Studies of the Clay Minerals Society Source Clays: Geological origin. *Clays and Clay Minerals,* 49(5), 374-380.

Monteiro, S. C. and Boxall, B. A. (2010) Occurrence and Fate of Human Pharmaceuticals in the Environment. In: Whitacre, D. M. ed. *Reviews of Environmental Contamination and Toxicology*. Springer Science+Business Media.

Morsy, F. A., El-Sherbiny, S., Hassan, M. S. and Mohammed, H. F. (2014) Modification and evaluation of Egyptian kaolinite as pigment for paper coating. *Powder Technology,* 264, 430-438.

Müller, G. (1967) Diagenesis in argillaceous sediments. In: *Developments in Sedimentology.* Netherlands: Elsevier.

Murray, H. H. (1988) Kaolin minerals: their genesis and occurrences. In: Bailey, S. W. ed. *Hydrous Phyllosilicates (exclusive of micas).* Reviews in Mineralogy – volume 19. Chelsea, MI: Mineralogical Society of America.

Murray, H. H. (2007) *Applied clay mineralogy: occurrences, processing and application of kaolins, bentonites, palygorskite-sepiolite, and common clays.* Amsterdam: Elsevier

Newman, A. C. D. and Brown, G. (1987) The chemical constitution of clays. In: Newman, A. C. D. ed. *Chemistry of Clays and Clay Minerals*. London: Mineralogical Society.

Nicholson, F. A., Smith, S. R., Alloway, B. J., Carlton-Smith, C., Chambers, B. J. (2003) An inventory of heavy metals inputs to agricultural soils in England and Wales. *The Science of the Total Environment,* 311, 205-219.

Olejnik, S., Aylmore, L. A. G., Posner, A. M., Quik, J. P. (1968) Infrared spectra of kaolin mineral-dimethyl sulfoxide complexes. The *Journal of Physical Chemistry,* 71(1), 241-249.

Oliveira, A., Rocha, F., Rodrigues, A., Jouanneau, J., Dias, A., Weber, O. and Gomes, C. (2002) Clay minerals from the sedimentary cover from the Northwest Iberian shelf. Progress in Oceanography, 52, 233-247.

Pasquet, J., Chevalier, Y., Pelletier, J., Couval, E., Bouvier, D. and Bolzinger, M.-A. (2014) The contribution of zinc ions to the antimicrobial activity of zinc oxide. *Colloids and Surfaces A: Physicochemical and Engineering Aspects,* 457, 263-274.

Petit, S. (2006) Fourier transform infrared spectroscopy. In: Bergaya, F., Theng, B. K. G. and Lagaly, G. eds. *Handbook of Clay Science.* Developments in Clay Science. Elsevier Ltd.

Petit, S. (2013) Infrared spectroscopy – Part II: Instrumentation [lecture notes]. University of Poitiers, France, delivered on 8 November 2013.

Petrović, M., Kaštelan-Macan, M. and Horvat, A. J. M. (1999) *Water, Air, and Soil Pollution,* 111, 41-56.

Petschick, R. (2001) MacDiff 4.2.5. Powder Diffraction Software.

Plante, A. F., Fernández, J. M. and Leifeld, J. (2009) Application of thermal analysis techniques in soil science. *Geoderma,* 153, 1-10.

Prasad, A. S. (2009) Zinc: role in immunity, oxidative stress and chronic inflammation. *Current Opinion in Clinical Nutrition and Metabolic Care,* 12(6), 646-652.

Pruett, R. J. and Webb, H. L. (1993) Sampling and analysis of KGa-1B well-crystallized kaolin source clay. *Clays and Clay Minerals,* 41(4), 514-519.

Puls, R. W. and Bohn, H. L. (1988) Sorption of cadmium, nickel, and zinc by kaolinite and montmorillonite suspensions. *Soil Science Society of America Jounal,* 52, 1289-1292.

Qureshi, J. A., Thurman, D. A., Hardwick, K., and Collin, H. A. (1985) Uptake and accumulation of zinc, lead and copper in zinc and lead tolerant *Anthoxanthum odoratum* L., *New Phytologist,* 100, 429-434.

Raussell-Colom, J. A. and Serratosa, J. M. (1987) Reactions of clays with organic substances. In: Newman, A. C. D. ed. *Chemistry of Clays and Clay Minerals.* London: Mineralogical Society.

Reynolds, Jr. R. C. (1989) Principles of Powder Diffraction. In: *Reviews in Mineralogy, vol. 20 – Modern Powder Diffraction.* Washington D.C.: Mineralogical Society of America.

Rocha, F. and Gomes, C. (2003) Assessment of the relevant properties of smectitic clays from Aveiro and Coimbra regions with regard to their potential use as liners in waste landfills. *Environment 2010; Situation and Perspectives for the European Union.* Porto, Portugal: 6-10 May.

Ross, C. S. and Kerr, P. F. (1930) Dickite, a kaolin mineral. *Journal Mineralogical Society of America,* 15(1) 34-39.

Ruiz Cruz, M. D. (2007) Genesis and evolution of the kaolin-group minerals during the diagenesis and the beginning of metamorphism. In: Nieto, F. and Jiménez-Millán, J. eds. *Diagenesis and Low-Temperature Metamorphism. Theory, Methods and Regional Aspects.* Seminarios SEM, 3,41-52.

Ruiz Cruz, M D. and Franco Duro, F. I. (1999) New data on the kaolinite-potassium acetate complex. *Clay Minerals,* 34, 565-577.

Ruiz-Hitzky, E. and van Meerbeek, A. (2006) Clay mineral- and organoclay-polymer nanocomposite. In: Bergaya, F., Theng, B. K. G. and Lagaly, G. eds. *Handbook of Clay Science.* Developments in Clay Science Vol. 1. Elsevier Ltd.

Russell, J. D. and Fraser, A. R. (1994) Infrared methods. In: Wilson, M. J. ed. *Clay mineralogy: spectroscopic and chemical determinative methods*. London: Chapman & Hall.

Saada, A., Breeze, D., Crouzet, C., Cornu, S. and Baranger, P. (2003) Adsorption of arsenic (V) on kaolinite and on kaolinite-humic acid complexes: Role of humic acid nitrogen groups. *Chemosphere,* 51, 757-763.

Saikia, B. J. and Parthasarathy, G. (2010) Fourier Transform infrared spectroscopic characterization of kaolinite from Assam and Meghalaya, Northeastern India. *Journal of Modern Physics,* 1, 206-210.

Sánchez-Soto, P. J., Jiménez de Haro, M. C., Pérez-Maqueda, L. A., Varona, I. and Pérez-Rodríguez, J. L. (2000) Effects of dry grinding on the structural changes of kaolinite powders. *Journal of The American Ceramics Society,* 83(7), 1649-1657.

Sanidanesh, M., Alwi, S. R. W. and Manan, Z. A. (2013) Potential of heavy metal recovery from wastewater and sewage sludge. Proceedings of the 6th International Conference on Process Systems Engineering

(PSE ASIA), 25-27 June, Kuala Lumpur.

Scheidegger, A. M. and Sparks, D. L. (1996) A critical assessment of sorption-desorption mechanisms at the soil mineral/water interface. *Soil Science,* 161(12), 813-831.

Scrudato, R. J. and Estes, E. L. (1975) Clay-lead sorption relations. *Environmental Geology,* 1, 167-170.

Sears, M. E. (2013) Chelation: harnessing and enhancing heavy metal detoxification – a review. *The Scientific World Journal,* article ID 219840.

Sei, J., Morator, F., Kra, G., Staunton, S., Quiquampoix, H., Jumas, J. C. and Olivier-Fourcade, J. (2006) Mineralogical, crystallographic and morphological characteristics of natural kaolins from the Ivory Coast (West Africa). *Journal of African Earth Sciences,* 46, 245-252.

Sempeho, S. I., Kim, H. T., Mubofu, E., Pogrebnoi, A., Shao, G., Hilonga, A. (2015) Encapsulated urea-kaolinite nanocomposite for controlled release fertilizer formulations. *Journal of Chemistry,* article ID 237397.

Shu, X., Yan, C. and Chen, J. (2012) Application of urea-intercalated kaolinite for paper coating. *Applied Clay Science,* 55, 114-119.

Sigma-Aldrich (2015a) Properties. 235334 - 3,6-dithia-1,8-octanediol [online]. Available at: http://www.sigmaaldrich.com/catalog/product/aldrich/235334?lang=en&region=CA [Accessed on 24 July 2015].

Sigma-Aldrich (2015b) Product Specification – Urea – ACS reagent, 99.0-100.5% [online]. Available at: http://www.sigmaaldrich.com/Graphics/COfAInfo/SigmaSAPQM/SPEC/U5/U512 8/U5128-BULK_________SIAL_____.pdf [Accessed on 4 August 2015].

Sigma-Aldrich (2015c) Product information – dimethyl sulfoxide [online]. Available at: https://www.sigmaaldrich.com/content/dam/sigma-aldrich/docs/Sigma/Product_Information_Sheet/d8418pis.pdf [Accessed on 4 August 2015].

Silverstein, R. M., Bassler, G. C. and Morrill, T. C. (1991) *Spectrometric identification of organic compounds.* Fifth edition. New York: John Wiley & Sons.

Silverstein, R. M. and Webster, F. X. (1998) *Spectrometric Identification of Organic Compounds.* 6th ed. New York: John Wiley & Sons, Inc.

Smith, S. R. (2009) A critical review of the bioavailability and impacts of heavy metals in municipal solid waste composts compared to sewage sludge. *Environment International,* 35, 142-156.

Środoń, J., Drits, V. A., McCarty, D. K., Hsieh, J. C. C. and Eberl, D. D. (2001) Quantitative X-ray diffraction analysis of clay-bearing rocks from random preparations. *Clays and Clay Minerals,* 49(6), 514-528.

Stietiya, M. H., Duqqah, M., Udeigwe, T., Zubi, R. and Ammari, T. (2014) Fate and distribution of heavy metals in wastewater irrigated calcareaous soils. *The Scientific World Journal, 2014*, ID 865934, 11 pages.

Suraj, G., Iyer, C. S. P., Rugmini, S., Lalithambika, M. (1997) The effect of micronization on kaolinites and their sorption behaviour. *Applied Clay Science,* 12, 111-130.

Tan, D., Yuan, P., Annabi-Bergaya, F., Liu, D. and He, H. (2015) Methoxy-modified kaolinite as a novel carrier for high-capacity loading and controlled-release of the herbicide amitrole. *Scientific Reports,* 5(8870).

Tandon, S. K., Sharma, B. L. and Singh, S. (1988) Chelation in metal intoxication XXVII: Chelating agents containing vicinal thioether groups as antidotes of lead toxicity. *Drug and Chemical Toxicology,* 11(1), 71-84.

Taylor, H. E. (2001) *Inductively Coupled Plasma-Mass Spectrometry: Practiced and Techniques.* San Diego: Academic Press.

The Clay Minerals Society (2003-2015) Baseline Studies of The Clay Minerals Society Sources Clays [online]. Available at: http://www.clays.org/SOURCE%20CLAYS/SCreferences.htmL [Accessed May-August, 2015].

Thompson, J. G. (1984) ^{29}Si and ^{27}Al nuclear magnetic resonance spectroscopy of 2:1 clay minerals. *Clay Minerals,* 19, 229-236.

Thompson, J. G. (1985) Interpretation of solid state ^{13}C and ^{29}Si nuclear magnetic resonance spectra of kaolinite intercalates. *Clays and Clay Minerals,* 33(3), 173-180.

Thompson, J. G. and Cuff, C. (1985) Crystal structure of kaolinite: dimethylsulfoxide intercalate. *Clays and Clay Minerals,*33(6), 490-500.

Thompson, J. G. and Barron, P. F. (1987) Further consideration of the ^{29}Si nuclear magnetic resonance spectrum of kaolinite. *Clays and Clay Minerals,* 35(1), 38-42.

Thompson, J. G., Uwins, P. J. R., Whittaker, A. K. and Mackinnon, D. R. (1992) Structural characterisation of kaolinite:NaCl intercalate and its derivatives. *Clays and Clay Minerals,* 40(4), 369-380.

Tonlé, I. K., Diaco, T., Ngameni, E. and Detellier, C. (2007) Nanohybrid kaolinite-based materials obtained from the interlayer grafting of 3-aminopropyltriethoxysilate and their potential use as electrochemical sensors. *Chemistry of Materials,* 19, 6629-6636.

Tonlé, I. K., Letaief, S., Ngameni, E., Walcarius, A. and Detellier, C. (2011) Square wave voltammetric determination of lead(II) ions using a carbon paste electrode modified by a thiol-functionalized kaolinite. *Electroanalysis,* 23(1), 245-252.

Tsunematsu, K. and Tateyama, H. (1999) Delamination of urea-kaolinite complex by using intercalation procedures. *Journal of the American Ceramic Society,* 82(6), 1589-1591.

Tunney, J. J. and Detellier, C. (1993) Interlamellar covalent grafting of organic units on kaolinite. *Chemistry of Materials,* 5, 747-748.

Tunney, J. J. and Detellier, C. (1994) Preparation and characterization of two distinct ethylene glycol derivatives of kaolinite. *Clays and Clay Minerals,* 42(5), 552-560.

Tunney, J. J. (1995) New nanocomposite materials from kaolinite as a mineral precursor. PhD. In Chemistry, University of Ottawa, Ottawa, Canada.

Tunney, J. J. and Detellier, C. (1996) Chemically modified kaolinite. Grafting of methoxy groups on the interlamellar aluminol surface of kaolinite. *Journal of Material Chemistry,* 6(10), 1678-1685.

USGS (n.d.) A laboratory Manual for X-Ray Powder Diffraction: Kaolinite Group [online]. Available at: http://pubs.usgs.gov/of/2001/of01-041/htmLdocs/clays/kaogr.htm [Accessed on 8 December 2014].

Vaia, R. A., Teukolsky, R. K., Giannelis, P. (1994) Interlayer structure and molecular environment of alkylammonium layered silicates. *Chemistry of Materials,* 6(7), 1017-1022.

Valášková, M., Rieder, M., Matějka, V., Čapková, P. and Slíva, A. (2007) Exfoliation/delamination of kaolinite by low-temperature washing of kaolinite-urea intercalates. *Applied Clay Science,* 35, 108-118.

Valiculíková, L., Plevová, E., Vallová, S. and Koutník, I. (2011) Characterization and differentiation of kaolinites from selected czech deposits using infrared spectroscopy and differential thermal analysis. *Acta Geodynamica et Geomaterialia,* 8(1), 59-67.

Wada, K. (1961) Lattice expansion of kaolin minerals by treatment with potassium acetate. *The American Mineralogist,* 46, 78-91.

Wang, S., Nan, Z., Cao, X., Liao, Q., Liu, J., Wu, W., Zhou, T., Zhao, C., Jin, W. (2011) Sorption and desorption behavior of lead on a Chinese kaolin. *Environmental Earth Sciences,* 63, 145-149.

Watanabe, T., Shimizu, H., Nagasawa, K., Masuda, A. and Saito, H. (1987) ^{29}Si- and ^{27}Al-MAS/NMR study of the thermal transformations of kaolinite. *Clay Minerals,* 22, 37-48.

Weiss, A. (1961) Eine schichteinschulußverbindung von kaolinit mit harnstoff. *Angewandte Chemie,* 73(22), 736.

Weiss, A. (1963) A secret of Chinese porcelain manufacture. *Angewandte Chemie – International Edition,* 2(12), 697-748.

Wilson, M. J., Russel, J. D. and Tait, J. M (1974) A new interpretation of the structure of disordered α-cristobalite. *Contributions to Mineralogy and Petrology,* 47, 1-6.

Yan, C. J., Chen, J. Y., Zhang, C. Z., Han, L. X. (2005) Kaolinite-urea intercalation composites. *The American Ceramic Society,* 84(12), 9301-9305.

Yang, S., Yuan, P., He, H., Qin, Z., Zhou, Q., Zhu, J. and Liu, D. (2012) Effect of reaction temperature on grafting of γ-aminoprolyl triethoxysilaten (APTES) onto kaolinite. *Applied Clay Science,* 62-63, 8-14.

Yariv, S. (1991) Differential thermal analysis (DTA) of organo-clay compexes. In: Smykatz-Kloss, W. and Warne, S. S. J. eds. *Lecture Notes in Earth Sciences*, 38, Thermal analysis in the Geosciences. Springer-Verlag.

Yariv, S. (2002) Introduction to organo-clay complexes and interactions. In: Yariv, S. (ed.) *Organo-Clay Complexes and Interactions.* New York: Marcel Dekker, Inc.

Young, R. A. and Hewat, A. W. (1988) Verification of the triclinic crystal structure of kaolinite. *Clays and Clay Minerals,* 36(3), 225-232.

Zachara, J. M., Cowan, C. E., Schmidt, R. L. and Ainsworth, C. C. (1988) Chromate adsorption by kaolinite. *Clays and Clay Minerals,* 36(4), 317-326.

Zamek, J. (2006) Pottery production practices: stoneware clay body formulas part 3 [online]. Ceramic Industry Magazine. Available at: http://www.ceramicindustry.com/articles/87856-pottery-production-practices-stoneware-clay-body-formulas-part-3 [Accessed on 9 August 2015].

Zhang, M., Gao, B., Jin, J., Chen, H., Yao, Y., Fang, J. and Creamer, A. E. (2015) Use of nanotechnology agains heavy metals present in water. In: Sharma, S. K. ed. *Heavy Metals in Water: Presence, Removal and Safety.* Cambridge: The Royal Society of Chemistry.

Zhengbang, P., Zhuoqin, L., Chao, Y., Xike, T., Jinbo, F. and Jianhua, Z. (2007) Exfoliation of kaolinite by urea-intercalation precursor and microwave irradiation assistance process. *Frontiers of Earth Science in China,* 1(1), 26-29.

Zhu, X., Chen, J., Chen, J., Lei, X. and Yan, C. (2014) Urea intercalation compound production in industrial scale for paper coating. *Chemical Industry & Chemical Engineering Quarterly,* 20(2), 241-248.

Appendix A – Preliminary clay characterisation studies at the University of Aveiro, Portugal

A.1. Introduction

In search of an appropriate clay sample to work with, a preliminary study was conducted at the University of Aveiro, Aveiro, Portugal. Four Portuguese clay samples from the Bustos- (samples B4 and B5; Bustos is marked as BST in Fig. 3.2.1c) and the Taveiro Formations (samples R2 and SP) were analysed to determine a suitable material for a future study involving the synthesis of clay nanocomposites for heavy metal sorption. Wet sieving was performed to collect the <63-µm fraction and sedimentation according to Stoke's Law to collect the fine fraction (<2 µm). Samples were characterized by X-ray diffraction (XRD), X-ray fluorescence (XRF) spectrometry, and sedigraph. Cation-exchange capacity (CEC) was determined by ammonium acetate method with Kjeldahl distillation. These results are presented here in a condensed form.

A.2. Semi-quantification based on XRD patterns

Peak areas in the XRD pattern of the <63-µm fraction of the clays were used to calculate the semi-quantitative mineral contents, using the correction factors outlined in Table 2.1.1. The ratio of smectite, illite, and kaolinite were assessed based on oriented slides (natural, heated to 500ºC, and treated with ethylene glycol), which was multiplied with the fraction of phyllosilicates calculated from the <63-µm fraction. Following Galhano *et al*., (1999), a factor of 0.1 was used for phyllosilicates when no smectite was detected (see Table 2.1.1.). Results of these calculations are summarized in Table A.1.

Table A.1. Semi-quantificaiton (mass %) of mineralogical composition of each sample, based on peak area calculations by MacDiff (version 4.2.5; Petschick, 2001). Phyllosilicate minerals were obtained from <2-µm-fraction oriented slides, as outlined in Table 2.1.1. Feldspars include K-, Ca-, and Na/Ca-feldspars.

	B4	**B5**	**R2**	**SP**
Phyllosilicates	*67*	*69*	*35*	*57*
Smectite	24	2	14	<1
Illite/mica	21	41	9	8
Kaolinite	22	26	12	49
Quartz	15	21	53	35
Feldspars	2	6	2	3
Anatase	2	n/a	3	n/a
Anhydrite	2	1	1	1
Bassanite	1	1	3	0
Dolomite	1	1	0	1
Siderite	n/a	1	n/a	1
Magnetite-Maghemite	3	2	3	2

A.3. Sedigraph grain size analysis

Grain size distribution data are summarized in Table A.2 and Figure A.1.

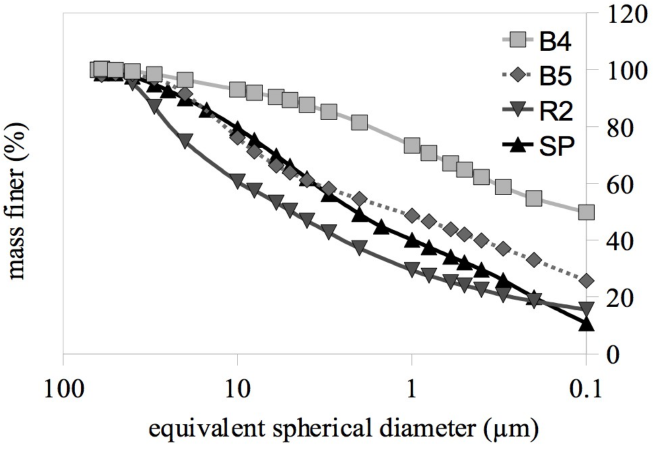

Figure A.1. Cumulative mass percent finer grain size distribution for each sample.

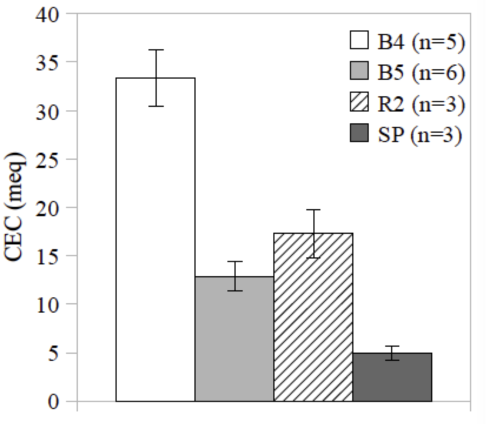

Figure A.2. Average CECs found for the four samples (meq per 100g dry sample). Part of data are results of other students in the group in order to determine errors. Error bars represent standard errors and n-values are indicated.

Table A.2. Grain size distribution for each of the samples, including median and modal grain diameters, and the relative amount of fraction <2 µm. Phyllosilicate semi-quantification from XRD results are included for comparison purposes only.

	B4	**B5**	**R2**	**SP**
Median diameter (µm)	0.10	1.19	4.89	2.10
Modal diameter (µm)	0.77	11.57	28.35	4.27
< 2 µm (%)	81.4	54.5	37.1	49.2
Phyllosilicates (%)	67	69	35	48

A.4. Cation-exchange capacity

Cation-exchange capacities of the <63-µm fractions are summarized in Figure A.2 (above). CEC of the <2-µm fraction of SP was also assessed, with a mean value of 6.47 meq/100g dry sample (SE=0.22; n=3). This is within the range expected for kaolinite clays, which is reported to be somewhere between 1 and 20 meq/100g, depending on the reference consulted (5-20 meq/100g according to Baron *et al*., 1971; 3-15 meg/100g according to Grim, 1968 cited in Bergaya *et al*., 2006; and 1-10 meq/100g according to Drever 1982 cited in Eslinger and Pevear, 1988), and not surprisingly it is higher than the mean CEC found or the <63-µm fraction that contains a lower concentration of phyllosilicates.

A.5. Chemical analyses by XRF

Chemical analysis by XRF as % oxide content is summarized in Table A.3.

Table A.3. Chemical analysis by XRF (% oxide content)

	B4	**B5**	**R2**	**SP**
SiO_2	54.906	62.033	64.284	55.848
Al_2O_3	21.363	20.147	18.605	29.636
Fe_2O_3	7.572	4.046	5.020	1.965
MnO	0.028	0.017	0.036	0.011
MgO	3.135	2.069	2.897	0.410
CaO	0.849	0.481	0.822	0.052
K_2O	3.430	3.712	2.162	1.802
TiO_2	0.812	0.786	1.070	0.605
P_2O_5	0.062	0.053	0.061	0.062
Na_2O	0.259	0.227	0.183	0.134
SO_3	0.010	0.015	0.013	0.022
Ba	0.024	0.028	0.019	0.018
Cr	0.012	0.007	0.008	0.007
Rb	0.021	0.025	0.010	0.009
Zr	0.020	0.025	0.086	0.020
L.O.I.	7.350	6.130	4.660	9.330

Appendix B – Selected characterisation results of KGa-1b extracted from the Baseline Studies (The Clay Minerals Society, 2003-2015)

Results shown here are taken from articles published as part of the Baseline Studies for reference purposes only. All analyses in the Baseline Studies were performed using the <2-µm fraction obtained by centrifugation (Costanzo, 2001).

B.1. Elemental composition

Chemical analysis of KGa-1 fine fraction was performed by Mermut and Cano (2001) by (primarily) atomic absorption spectrometry (Table B.1), and X-ray fluoresence of KGa-1b was reported by Pruett and Web (1993) for the <44 µm fraction (Table B.2). N.B. The latter is not part of the Baseline Studies.

Table B.1. Elemental composition (as % oxide content) of KGa-1 (N.B. this is not exactly the same location in the deposit as KGa-1b) fine fraction, as analysed by flame emission spectrometry for Na and K, and atomic absorption spectrometry for all other elements. The standard error (SE) of the averaged replicate results obtained by 4 different analysts are included (from Mermut and Cano, 2001).

	SiO_2	Al_2O_3	Fe_2O_3	TiO_2	MgO	CaO	Na_2O	K_2O	P_2O_5	LOI 110-550ºC	L.O.I. 550-1000ºC	TOTAL
% Oxide	43.36	38.58	0.35	1.67	0.04	0.04	0.05	0.00	0.37	13.60	1.45	99.51
SE	0.39	0.24	0.02	0.01	0.01	0.01	0.01	0.00	0.03			

Table B.2. Elemental composition (as % oxide content) of the <44-µm fraction of KGa-1b, as analysed by X-ray fluorescence. (from Pruett and Webb, 1993).

	SiO_2	Al_2O_3	Fe_2O_3	TiO_2	MgO	CaO	Na_2O	K_2O	P_2O_5	LOI 1025ºC	TOTAL
% Oxide	45.1	39.2	0.21	1.66	0.06	0.03	0.03	0.02	-	13.8	86.31

B.2. Trace-element chemistry

Trace element chemistry was analysed by Kogel and Lewis (2001) by ICP-MS of clay sample microwave digested in 250 µL HF, 2 mL HCl, 2 mL HNO_3 and 2 mL H_2O (Table B.3.)

Table B.3. Concentrations (ppm) of trace elements (analyte, isotope) of KGa-1b. Mean and standard deviation from 3 replicate experiments (taken from Kogel and Lewis, 2001)

	Co 59	Ni 60	Cu 63	Rb 85	Sr 88	Y 89	Mo 95	Sn 118	Sb 121	La 139	Ce 140	Pr 141	Nd 146
Mean	3.27	**17.87**	**25.24**	1.32	41.69	6.95	2.02	5.74	0.3	33.73	77.12	9.28	40.07
SD	0.14	0.96	1.44	0.29	3.19	0.74	0.31	0.73	0.09	2.7	5.73	0.68	3.79
	Sm 147	Eu 151	Gd 157	Tb 159	Dy 162	Ho 165	Er 166	Tm 169	Yb 174	Lu 175	Pb 208	Th 232	U 238
Mean	9.91	2.51	10.43	1.15	3.74	0.369	0.717	0.048	0.462	0.071	**32.5**	37.15	1.96
SD	1.97	0.34	1.31	0.19	0.36	0.073	0.078	0.024	0.003	0.024	3.99	5.54	0.4

B.3. Cation-exchange capacity

Borden and Giese (2001) report a CEC value of 3.0 meq/100g (SD=0.1, n=6) for KGa-1b, measured by the ammonia-electrode method.

B.4. Thermal analysis

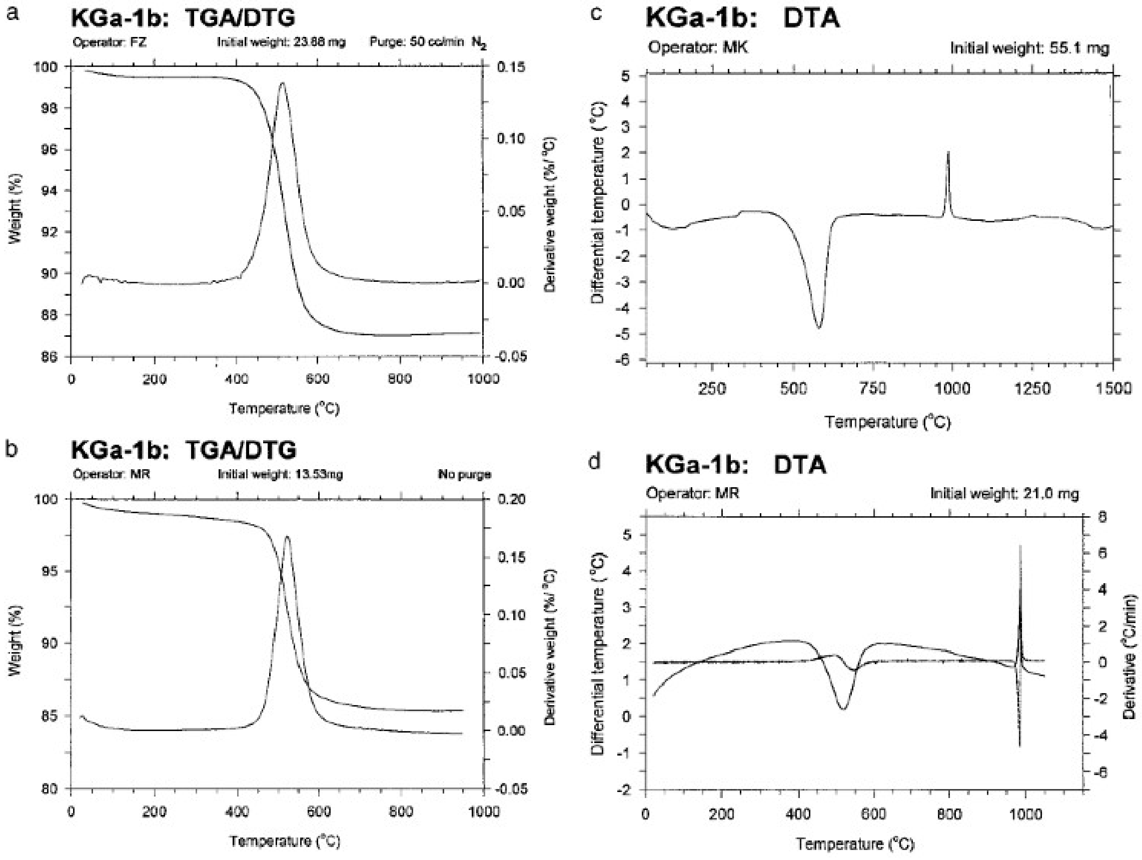

Figure B.1. Thermal analysis of KGa-1b by (a) TGA/DTG under nitrogen (platinum sample pan); (b) TGA/DTG without nitrogen (platinum sample pan); and DTA analysis under nitrogen performed at two different universities with different instrument shown in (c) (alumina sample pan) and (d) (platinum sample pan) (taken from Guggenheim and van Groos, 2001).

Appendix C – Subsidiary results to chapter 3

C.1. FT-IR spectrum of SP-DMSO

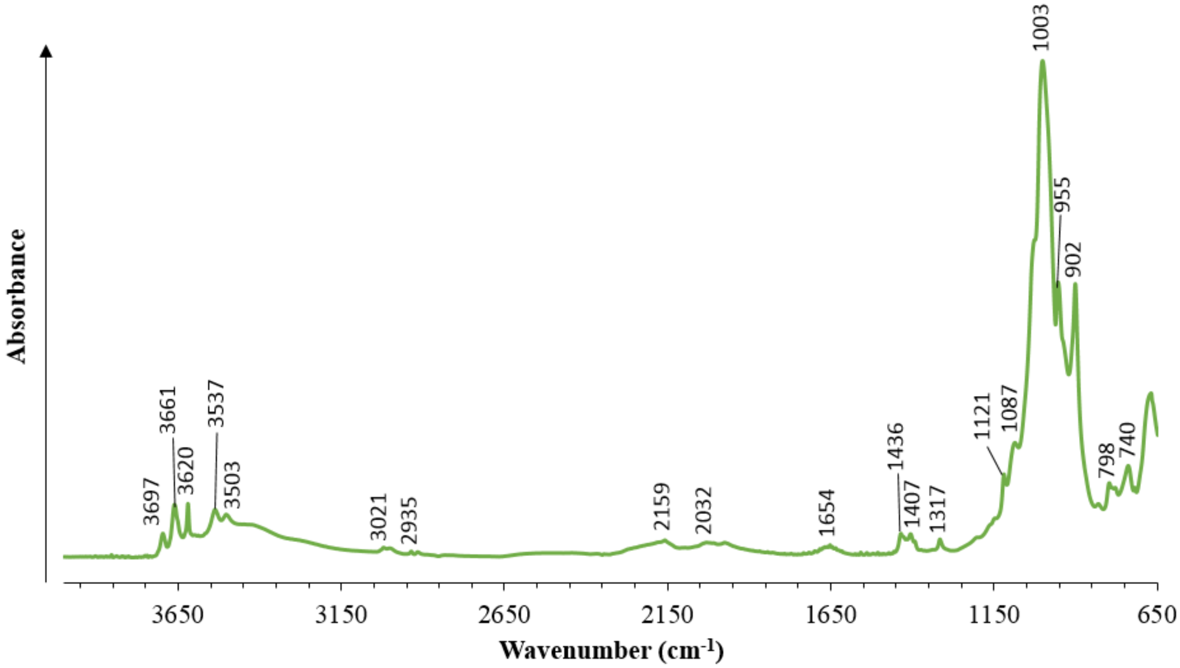

Figure C.1. FT-IR spectrum of SP-DMSO

The FT-IR spectrum of SP-DMSO (Fig. C.1) shows considerably more organic matter associated with the sample (bands between the OH stretching and Si-O regions) of the spectrum than the DMSO precursor of KGa-1b (Fig. 3.4.9). The peaks in the OH-stretching and Si-O regions are more or less identical, indicated the same interaction between DMSO and the interlayer surfaces. Peaks appearing along the central region between 3000 and 1700 cm^{-1} may also be related to interactions between DMSO and the accessory minerals in SP.

C.2. Images of the clay samples

The images below are a selection of sample photographs to illustrate their colours and textures. Figures C.8 and C.14 have been included to demonstrate the sensitivity of the melt-intercalation grafting process and the difficulty of obtaining the same product each time. The sample of K-urea-DTOD shown in figure C.8 is very coarsely crumbled but cannot be ground finer. The sample of SP-urea-DTOD shown in figure C.14 had a very different colour, as if it were burnt.

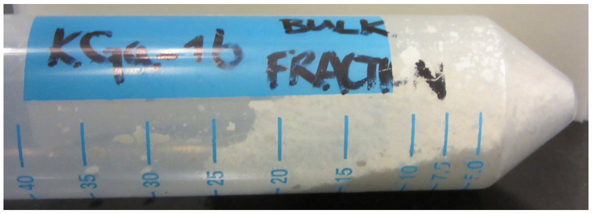

Figure C.2. Photograph of K-bulk

Figure C.3. Photograph of K-fine

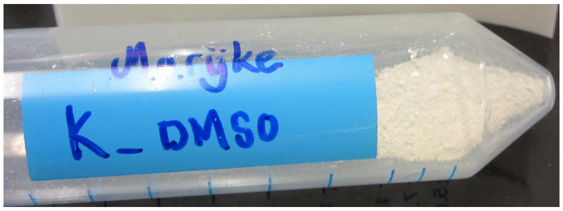

Figure C.4. Photograph of K-DMSO

Figure C.5. Photograph of K-urea

Figure C.6. Photograph of K-DMSO-DTOD

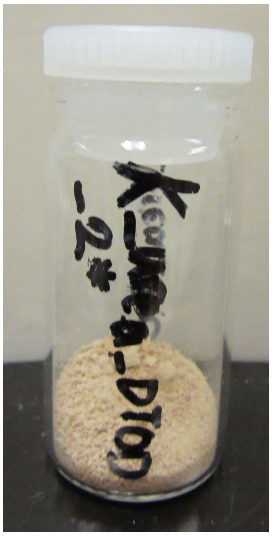

Figure C.7. Photograph of K-urea-DTOD

Figure C.8. Photograph of another K-urea-DTOD assay for comparison purposes

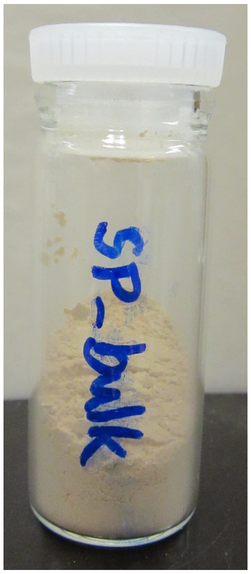

Figure C.9. Photograph of SP-bulk

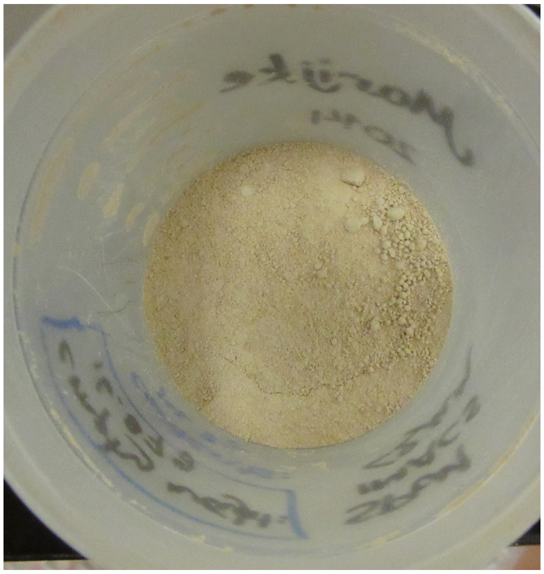

Figure C.10. Photograph of SP-fine

Figure C.11. Photograph of SP-urea

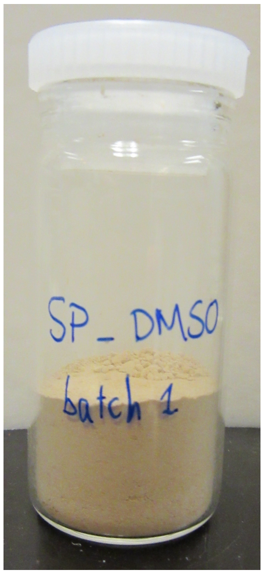

Figure C.12. Photograph of SP-DMSO

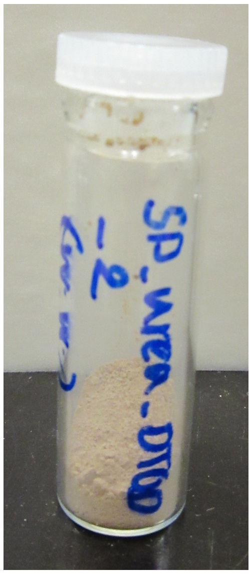

Figure C.13. Photograph of SP-urea-DTOD

Figure C.14. Photograph of another SP-urea-DTOD assay for comparison purposes

Appendix D – Example calculations for data processing of ICP-MS-measured sorption results

The example of Zn analysis of replicate number 3 of the K-fine treatment in sample set 3 will be used to demonstrate how data processing was performed. The calculations will be presented in seven steps: (1) determination of the dilution factor and the clay concentration; (2) correction of raw data for dilution; (3) calculation of the initial concentration; (4) normalisation to exact solution and clay weights in the vial; (5) calculation of the sorbed zinc-to-clay ratio; (6) calculation of the % sorption; and (7) calculation of the adjusted final zinc concentration.

(1) The preparation of each vial involved the recording of the weight of the appropriate amount of clay sample and the weight of solution (spiked DI- or waste-water), as well as the weight of the sample extracted for dilution in a new vial and the total weight of the diluted sample. The latter were converted into a dilution factor. If a sample was not diluted the dilution factor was 1. The former – the solution and clay weights – were converted into a clay concentration in ppm (mg clay per kg solution).

For the example sample 4.9786 g of wastewater with 0.0498 g clay was weighed, equalling a clay concentration of:

0.0498g clay(1000mg/g)/0.0050 kg wastewater = **10003 ppm** clay.

The supernatant was diluted 10 times as: 1.0638 g supernatant in 10.6446 g diluted solution with 1% nitric acid, giving a dilution factor of:

10.6446g/1.0638g = **10.0062**.

(2) The raw measurement given by the ICP-MS instrument was a Zn concentration of 97 ppb. This final Zn concentration was corrected by the dilution factor and converted to ppm:

97 ppb x 10.0062 = 968.2658 ppb = **0.9683 ppm**

(3) The data on the initial Zn concentration vials was also corrected for dilution in the same way. The average of the 5 initial-concentration replicates was then assumed for all treatments. In set 3 this was 5905.82 ppb (SD=169.5; SE=75.81) = **5.9058 ppm**.

(4) Normalisation of the initial and final concentration was done by multiplication with the clay concentration (see step 1) to obtain initial and final zinc-to-clay ratios.

Initial zinc-to-clay ratio: (1000mg/g)(5.9058 mg/kg)/(10003 mg/kg) = **0.5904 mg Zn/g clay**

Final zinc-to-clay ratio: (1000mg/g)(0.9683 mg/kg)/(10003 mg/kg) = **0.0968 mg Zn/g clay**

(5) Determination of the sorbed zinc-to-clay ratio is simply the initial ratio minus the final ratio:

0.5904 mg/g – 0.0968 mg/g = **0.4936 mg Zn sorbed/g clay**

This is the value that is given in parentheses above the %-sorption figures presented for some of the analytes in chapter 4.

(6) The % sorption was calculated as:

sorbed ratio/initial ratio*100% = 0.4936/0.5904*100% = **83.60%**

This is the value that was used in the % sorption charts presented in chapter 4.

(7) Finally, to obtain a Zn concentration that would have been determined directly by the ICP-MS (after correction for any dilution) if a perfect amount of clay and Zn-spiked solution had been prepared in the vial, the ideal final concentration was determined. If exactly 0.0050 kg wastewater would have been used with exactly 50 mg clay, the clay concentration would have been exactly **10000 ppm**. Therefore the final corrected concentration from step 2 was multiplied with the quotient of the ideal clay concentration and the actual clay concentration (step 1):

<u>Ideal/adjusted final Zn concentration</u>: 968.2658 ppb (10000ppm/10003ppm) = **967.99 ppb**

These adjusted yet idealised values were used in the bar charts that display final metal concentrations in ppb or, in some cases ppm.

Appendix E – Subsidiary results to chapter 4

E.1. Wastewater parameters

Table E.1. General raw sewage and final effluent parameters kindly provided by Tim Lewis at the Robert O. Pickard Environmental Centre, showing values for 20 March and 10 July with the monthly mean (SE). Key of codes included below the table.

	Raw sewage				Final effluent			
	20 March	Mean (SE)	10 July	Mean (SE)	20 March	Mean (SE)	10 July	Mean (SE)
cBOD (mg/L)	239	208 (10)	215	197 (11)	10	12 (1)	5	5 (0.4)
COD (mg/L)	585	608 (20)	585	593 (35)	81	84 (4)	37	48 (4)
TSS (mg/L)	346	311 (16)	312	361 (17)	9	10 (1)	5	7 (1)
VSS (% TSS)	83	83 (1)	84	78 (2)	-	-	-	-
TP (mg/L)	6.71	6.14 (0.18)	5.47	5.67 (0.1)	0.74	0.68 (0.04)	0.64	0.59 (0.04)
RP (mg/L)	2.74	1.86 (0.10)	1.41	1.38 (0.08)	0.31	0.25 (0.03)	0.46	0.37 (0.03)
PT RP (mg/L)	-	-	-	-	0.32	0.21 (0.03)	0.46	0.34 (0.04)
TKN-N (mg/L)	51.7	45.0 (1.0)	42.7	43.1 (1.4)	35.3	34.9 (0.7)	28.5	27.7 (0.7)
dNH_3 (mgN/L)	35.1	31.9 (0.8)	28.2	26.7 (0.6)	33	32.1 (0.8)	26.5	25.1 (0.6)
NO_x (mgN/L)	-	0.16 (0.01)	-	0.20 (0.00)	0.38	0.47 (0.03)	2.69	2.43 (0.56)
Alk (mg/L)	232	221 (2)	225	225 (3)	214	208 (2)	202	201 (5)
Un-ionized NH_3 (mgN/L)	-	-	-	-	0.08	0.06 (0.01)	0.11	0.11 (0.00)

cBOD – Carbonaceous biological oxygen demand (measure of biodegradable compounds)
COD – chemical oxygen demand (measure of biodegradable and non-biodegradable compounds)
TSS – total suspended solids (non-filtrable residue)
VSS – volatile suspended solids
TP – total phosphorus
RP – reactive phosphorus
PT RP – reactive phosphorus test performed by process technicians
TKN-N – total Kjeldahl nitrogen (NH_3+NH_4^+)
NH_3-N – nitrogen in the form of ammonia, though mostly dissolved in ionized form
No_x-N – nitrogen in the form of NO_x
Alk – alkalinity as $CaCO_3$
Un-ionized NH_3-N – ammonia only

Table E.2. Metal concentrations measured in raw sewage and final effluent. Data kindly provided by Tim Lewisat the Robert O. Pickard Environmental Centre. Showing the average metal concentrations (ppb) for the year 2012 (most recent data available) with the standard error of the mean (SE).

	Raw sewage		Effluent	
Element	Average (ppb)	SE	Average	SE
Al	2607	398	50	9
As	23	6	14	5
B	124	6	122	6
Ba	55	5	20	1
Be	70	28	65	26
Bi	13	1	13	1
Ca	54258	3283	48320	2546
Cd	5	0	5	0
Co	5	0	5	0
Cr	6	0	5	0
Cu	43	5	8	1
Fe	1195	226	195	24
Hg	88	24	50	0
K	13157	563	11364	328
Mg	13792	815	12238	647
Mn	56	4	52	3
Mo	5	0	5	0
Na	24115	12627	43428	13663
Ni	5	0	5	0
P	4526	342	394	34
Pb	11	2	10	2
Sb	12	2	12	3
Se	15	6	10	5
Si	0	0	-	-
Sn	8	1	7	1
Sr	883	46	804	37
Ti	26	7	5	0
Tl	21	6	20	6
V	5	0	5	0
Zn	79	9	22	5

E.2. Sorbed ratios

The sorption efficiency of the analytes onto each clay sample expressed in mg per g of clay is summarized in Table E.3.

Table E.3. Average sorbed ratio in mg/g clay of each analyte in sorption sets 2 and 3. Negative values represent release.

Set 2 – Simple system experiment													
	Zn	Ni	Cu	As	Cd	Pb	Cr	Mn	Fe	Na	Mg	Ca	
K-fine	38.23	-0.01	0.00	0.00	0.00	0.00	0.00	0.00	0.00	0.00	-0.03	-0.04	
K-DMSO-DTOD	26.18	0.00	0.00	0.00	0.00	0.00	0.00	0.00	0.00	-0.05	0.00	-0.01	
K-urea-DTOD	0.53	0.00	0.00	0.00	0.00	0.00	0.00	0.00	0.00	-0.29	-0.01	-0.03	
SP-fine	0.51	0.00	0.00	0.00	0.00	0.00	0.00	0.01	-0.62	-0.16	-0.09	-0.07	
SP-urea-DTOD	0.75	0.00	0.00	0.00	0.00	0.00	0.00	0.01	-0.01	-0.10	-0.07	-0.14	
Set 3 – Wastewater system experiment													
	Zn	Ni	Cu	As	Cd	Pb	Cr	Mn	Fe	Na	Mg	Ca	S
K-fine	0.486	0.00	0.00	0.00	0.00	0.00	0.00	0.00	0.00	0.38	0.050	0.196	0.13
K-DMSO-DTOD	0.466	0.00	0.00	0.00	0.00	0.00	0.00	0.00	0.00	0.19	0.056	0.165	-4.96
K-urea-DTOD	0.544	0.0	0.00	0.00	0.00	0.00	0.00	0.00	0.00	-0.24	0.042	0.192	-10.0
SP-fine	0.550	0.00	0.00	0.00	0.00	0.00	0.00	0.00	0.00	-0.04	0.075	0.550	0.05
SP-urea-DTOD	0.570	0.00	0.00	0.00	0.00	0.00	0.00	0.00	0.00	0.04	0.052	0.305	-2.40